Defining Fractionation in LA-ICP-MS Analysis of Volcanic Glass Shards and its Application to the Correlation of Tephra Deposits from Ulleungdo, Korea

Catherine Martin-Jones

Thesis submitted in fulfilment of the requirements for the degree of Master of Philosophy at Aberystwyth University

November 2012

Abstract

This study attempts to define element fractionation when analysing tephra glass shards using laser ablation inductively coupled plasma-mass spectrometry (LA-ICP-MS). Sixteen MPI-DING and USGS reference materials and natural tephra samples have been repeatedly analysed using a 193 nm Excimer laser coupled to a magnetic sector ICP-MS. ^{29}Si is a suitable internal standard for the analysis of rhyolitic glass shards using <10 µm crater diameters, whilst ^{43}Ca and ^{44}Ca are only suitable internal standards for the analysis of basaltic glass using >10 µm crater diameters.

Element fractionation becomes significant at <20 µm crater diameters and generally increases with decreasing crater diameter. Relative to certified concentrations; Zr is typically underrepresented by ~10% at 10 µm crater diameters, ~20% at 6 µm crater diameters and ~25% using 4 µm crater diameters. Elements fractionate differently; yet there is no correlation between fractionation and ionic radius, field strength, condensation temperature, electronegativity or ionization energy. Higher excitation voltages increase the fractionation of 20 µm and 10 µm crater diameters, possibly associated with a concomitant increase in laser pulse length. However, excitation voltage does not influence the fractionation of <10 µm crater diameters. Polymerisation, viscosity, liquidus temperature and iron concentration do not exert a systematic control on element fractionation.

The systematic influence of crater diameter on fractionation allows for its correction. Fractionation factors have been calculated from the repeated analysis of 16 samples and have been applied to Minoan (rhyolite) and UT2252 (basalt) glass shard analyses. Application of these fractionation factors brings concentrations measured from 6 µm crater diameters to within ±10% of concentrations from 20 µm crater diameters. Precisions from 20 µm and 10 µm crater diameters are good, at ±10-20%, whilst analyses performed at < 10 µm crater diameters are subject to ±20-50% errors.

Fractionation factors calculated here are also applied to the 10 µm and 6 µm crater diameter trace element analyses of Ulleungdo (Korea) proximal pyroclastic Units 2, 3 and 4. Ulleungdo units share similar trace element chemistry, thus further glass and mineral analyses are required in order to correlate further with the Suigetsu SGO6 (Japan) core.

Acknowledgements

I would like to thank the IGES department, Aberystwyth, for making this research possible.

Importantly, I would like to thank my supervisors Prof. Nick Pearce and Dr. Bill Perkins for their guidance, support and encouragement over the past year. I also thank to my external supervisor, Dr. Victoria Smith (RLAHA), for providing samples, facilitating my use of the EPMA at RLAHA and accommodating me in Oxford.

I acknowledge the invaluable LA-ICP-MS training provided by Prof. John Westgate and access to samples and major element data. I thank Dr. Charlie Bendall for his help whilst calculating sample polymerisation. Additionally, I would like to thank Andy Brown for his help in the laboratory, particularly with the density separation of my samples.

I particularly thank my office mates, Keith, Ian, Janet and Jo, with whom I shared many hilarious moments and cups of tea. A special thanks to Huw for his patience and constant support. I thank Kayleigh for her loyal friendship and always making me laugh. Most importantly I thank my family; particularly my Mum for encouraging my interest in geology from a young age and without her support this work would not have been possible.

Declaration

This work has not previously been accepted in substance for any degree and is not being concurrently submitted in candidature for any degree.

Signed …….. (candidate)

Date ……..

Statement 1

This thesis is the result of my own investigations, except where otherwise stated. Where correction services have been used, the extent and nature of the correction is clearly marked in a footnote(s).

Other sources are acknowledged by footnotes giving explicit references. A bibliography is appended.

Signed …….. (candidate)

Date ……..

Statement 2

I hereby give consent for my thesis, if accepted, to be available for photocopying and for inter-library loan, and for the title and summary to be made available to outside organisations.

Signed …….. (candidate)

Date ……..

Table of Contents

Page

Abstract……*i*
Acknowledgements……*ii*
Declaration……*iii*
Table of Contents……*iv*
List of Figures……*vi*
List of Tables……*xi*

Chapter 1 Tephrochronology and its Application

1.1 Introduction……1
1.2 Major Element Analysis……2
1.3 Trace Element Analysis and the Development of LA-ICP-MS……3
1.4 Element Fractionation……7
1.5 The Application of LA-ICP-MS to Tephrochronology……15
1.6 Correlation of the Suigetsu Lacustrine Archive to Ulleungdo, Korea……16
1.6.1 Lake Suigetsu……16
1.6.2 The SG06 Archive……17
1.6.3 Ulleungdo Tephra……18

Chapter 2 Aims and Methodology
2.1 Aims……20
2.2 Methodology……21
2.2.1 Ulleungdo Sample Preparation……21
2.2.2 Geochemical Analysis……25
2.2.3 Calculation of Compositional Parameters……29

Chapter 3 LA-ICP-MS Analytical Considerations
3.1 Lower Limits of Quantification……34
3.2 Assessment of Existing Fractionation Correction……42
3.3 The Response of Natural Glass Compositions and Reference Materials to Element Fractionation……44

Chapter 4 Element Fractionation
4.1 The Impact of Crater Diameter on Fractionation ……47
4.1.1 Discussion of Fractionation Associated with Crater Diameter……52

4.2 The Response of Trace Elements to Fractionation……53
4.2.1 Discussion of Fractionation Associated with Element Properties……55

4.3 The Impact of Excitation Voltage on Element Fractionation……57
4.3.1 Discusssion of Element Fractionation and Excitation Voltage……60

4.4 Element Fractionation and ……61
4.4.1 Element Concentration and Fractionation……....61
4.4.2 The Control of Sample Matrix on Element Fractionation……...64
4.4.3 Discussion of Fractionation Associated with Composition…….72

Chapter 5 Calculation of New Fractionation Factors
5.1 Calculation of Fractionation Factors……..73
5.2 Testing New Fractionation Factors…….73

Chapter 6 Characterisation of Ulleungdo Tephra
6.1 Major Element Glass Chemistry and Comparison with other Studies…….83
6.2 Trace Element Glass Chemistry and Comparison with other Studies……..88
6.3 Statistical Distance Tests and Possible Correlations……95

Chapter 7 Conclusions……..98

Reference List ……104

Appendices …….....108

Appendix 1 MPI-DING and USGS reference materials with no F.F……...111
Appendix 2 The Pearce *et al.* (2011) 20 μm crater diameter F.F…….117
Appendix 3 Trace element analyses of 16 samples corrected only using the Pearce *et al.* (2011) F.F……..118
Appendix 4 Calculation of LLD and LLQ……...136
Appendix 5 Calculation of sample polymerisation (NBO/T)……..156
Appendix 6 Fractionation and element properties……...158
Appendix 7 Excitation voltage and fractionation……159
Appendix 8 Calculation of new fractionation factors……..160
Appendix 9 Application of new F.F.s to trace element analyses UT2252 and Minoan glass shards……162
Appendix 10 Major element compositions of Ulleungdo proximal units……...170
Appendix 11 Trace element compositions of Ulleungdo proximal units, with only the Pearce *et al.* (2011) F.F. applied……..172
Appendix 12 Trace element compositions of Ulleungdo proximal units with new F.F……175
Appendix 13 Statistical distance tests……178

List of Figures ***Page***

Chapter 1 Tephrochronology and its Application
1.30……4
Absorption of UV, visible and near-infrared wavelengths for biotite, pyroxene, hornblende and microcline.
1.31……5
Optical path of GeoLas ArF Excimer laser (Compex 110 Lambda Physik) used in this study (from Heinrich *et al.,* 2003).
1.32……5
Expansion of NIR-ns-LA generated aerosols over time using (a) He as a carrier gas and (b) Ar as a carrier gas (from Pisonero and Gunther, 2008).
1.33 ……6
Schematic illustrating the diversion of Ar around some of the sample chamber (from Pearce et al., 2011), this configuration is used in this study.
1.40 ……7
Possible causes and locations of fractionation in LA-ICP-MS (from Sylvester, 2008).
1.41 ……8
Minoan glass (Santorini) analyses
1.42……9
SEM images of the development of melt films lining craters ablated into NIST 612 using an ArF Excimer laser (from Eggins *et al.,* 1998)
1.43……....10
SEM images of surface condensate formation within 4µm and 6µm craters in Minoan glass, Santorini.
1.44……13
Increasing transparency with decreasing Fe concentration of NIST SRM reference glasses (from Gaboardi and Humayan, 2009).
1.45 ……...13
Measured concentrations divided by reported concentrations and plotted against element behaviour for: NIST 612 and NIST 614.
1.46 ……...14
Fractionation index of Ba, Zr, Ce, Rb, Sr plotted against polymerisation (NBO/T) (Mysen, 1983) for a range of silicate glass compositions.
1.60 …….....16
Location of Lake Suigetsu, Japan, and Ulleungdo, South Korea (from Smith *et al.,* 2011a)
1.61 ……17
SG06 core lamination, event and tephra stratigraphy.
1.62 ……18
Distribution of Late Pleistocene major tephra marker layers of Japan and neighbouring areas (from Machida *et al.,* 1984)

Chapter 2 Aims and Methodology
2.20…….....22
Location of sample collection sites on Ulleungdo, Korea, adapted from Smith *et al.* (2011).
2.21 ……..23
Sample sieving procedure
2.23……...24
Density separation procedure
2.24……...30
Relationship between SiO_2 wt% with NBO/T, viscosity, liquidus temperature and iron concentration.

Chapter 3 LA-ICP-MS Analytical Considerations
3.10……...35
Counts per second obtained from one day of analysis
3.11……...36
Change in LLD for the rhyolitic reference glass material, ATHO-G, using crater diameters of 20 µm, 10 µm, 6 µm and 4 µm. Note vertical log scales
3.20……...42
Average deviations from GeoReM concentrations.
3. 21…….....43
Average measured divided by accepted concentrations for basic glasses (BCR-2G, BHVO-2G), intermediate glass (T1-G) and acidic glass (ATHO-G), from Pearce *et al.* (2011).
3.30……...45
Increase in RSD% (standard deviation/average) with decreasing crater diameter, for samples of natural composition and reference materials.
3.31……...46
F.I. (conc. at *x* µm crater diameter / conc. at 20 µm crater diameter) plotted against SiO_2 wt% of 15 samples analyses using a range of crater diameters.

Chapter 4 Element Fractionation
4.10……...48
Average of determined/accepted concentrations using A) 20 µm crater diameters and B) 10 µm crater diameter, for basic compositions (BCR-2G, BHVO-2G and KL2-G), intermediate compositions (StHs/680-G and T1-G) and acidic compositions (ATHO-G).
4.11……...49
Average of determined/accepted concentrations using A) 6 µm crater diameters and B) 4 µm crater diameter, for basic compositions (BCR-2G, BHVO-2G and KL2-G), intermediate compositions (StHs/680-G and T1-G) and acidic compositions (ATHO-G).
4.12……...50
Average concentrations of Zr, Pr and Rb in ATHO-G obtained over six sessions of five repeat analyses at 20 µm, 10 µm, 6 µm and 4 µm crater diameters.

4.13……...51
Fractionation index (F.I.) for Zr, Sr, Rb, Ba, Th and Ce in basic, intermediate and acidic reference materials and samples of natural composition plotted against crater diameter
4.20……...54
Fractionation index for 26 trace elements in MPI-DING reference materials against selected element properties.
4.21……...56
A) Fractionation for the REE calculated as (REE/^{29}Si $_{(\text{last run})}$)/ REE/^{29}Si $_{(\text{first run})}$) in NIST 610 versus ionic radius (from Jeffries *et al.*, 1997), B) F.I. for the REE in MPI-DING reference materials analysed in this study against ionic radius.
4.22……...56
Fractionation index against elements ordered by Lodders (2003)
4.30……...58
Average measured concentrations/ accepted concentrations for ATHO-G, with analyses conducted at excitation voltages of 24.2 kV and 28 kV and 20 µm and 10 µm crater diameters.
4.31……...59
Average measured concentrations/ accepted concentrations for ATHO-G, with analyses conducted at excitation voltages of 24.2 kV and 28 kV 6 µm and 4 µm crater diameters.
4.32……...60
Schematic of ablation using A) a femtosecond laser and B) using a nanosecond laser (from Ferrnandez *et al.*, 2007).
4.40……...62
Concentrations of A) Y, B) Zr, C) Th, D) Ba, E) Ce, F) Rb in 15 reference materials and tephra samples vs. the respective 10 µm, 6 µm, 4 µm crater diameter fractionation indices (F.I.).
4.41……...63
Signal intensity ratio of Zr and Y counts per second (cps) versus Si cps plotted against the respective Zr and Y fractionation indices
4.42……...65
F.I for Zr and Y measured from 10 µm (A and B), 6 µm (C and D) and 4 µm crater diameters in 15 samples and NIST 612 (*) against calculated NBO/T.
4.43……...66
F.I for Ce and Th measured from 10 µm (A and B), 6 µm (C and D) and 4 µm crater diameters in 15 samples against calculated NBO/T.
4.44……...67
F.I. for Ba and Rb measured from 10 µm (A and B), 6 µm (C and D) and 4 µm crater diameters in 15 samples against calculated NBO/T.
4.45……...69
F.I. for Zr and Rb measured from 10 µm (A and B), 6 µm (C and D) and 4 µm crater diameters in 15 samples against calculated Bottinga-Weill Viscosity (Pa s).
4.46……...70
F.I. for Zr and Rb measured from 10 µm (A and B), 6 µm (C and D) and 4 µm crater diameters in 15 samples against calculated liquidus temperature (^{o}C)

4.47……...71
F.I. for Zr and Rb measured from 10 µm (A and B), 6 µm (C and D) and 4 µm crater diameters in 15 samples against calculated FeOwt%.

Chapter 5 Calculation of New Fractionation Factors

5.10……...73
Fractionation index for trace elements in basic, intermediate, and acidic samples and at 10 µm, 6 µm and 4 µm crater diameters corrected using F.F.s from this study.
5.11……...77
Zr and Y concentrations in Minoan glass shard analyses from at 20 µm, 10 µm, 6 µm and 4 µm crater diameters, with a series of F.F.s applied.
5.12……...78
Rb and La concentrations in Minoan glass shard analyses at 20 µm, 10 µm, 6 µm and 4 µm crater diameters, with a series of F.F.s applied.
5.13……...79
Zr and Y concentrations in glass shards from UT2552 (~45wt % SiO_2) from Pearce *et al.* (2011) at 20 µm, 10 µm, 6 µm and 4 µm crater diameters with a series of F.F.s applied.
5.14……...80
La and Rb concentrations in glass shards from UT2552 (~45wt % SiO_2) from Pearce *et al.* (2011) at 20 µm, 10 µm, 6 µm and 4 µm crater diameters, with a series of F.F.s applied.

Chapter 6 Characterisation of Ulleungdo Tephra
6.10……...81
A) SG06-1288 tephra in the Suigetsu core, B) and C) U4 outcropping on Ulleungdo, Korea (from Smith *et al.*, 2011a).
6.11……...82
Simplified stratigraphic columns showing pyroclastic units at sites K1 and K7 on Ulleungdo.
6.12……...84
TAS plot of Ulleungdo proximal units with comparison of glass shard analyses from SG06 core, Japan (Smith *et al.* submitted).
6.13……...85
Harker diagrams for Ulleungdo proximal units
6.14……...87
Harker diagrams comparing Ulleungdo proximal units with AT tephra proximal glass compositions from (Smith *et al.*, submitted).
6.20……..90
Selected trace element variation plots for Ulleungdo units and compared with glass compositions from (Park *et al.,* 2007 and Smith *et al.,* submitted).
6.21……...92
Trace element ratios for Ulleungdo proximal glass compared with AT, U-Oki and U-Ym glass compositions from Park *et al.* (2007)
6.22……...93
Pearce tectono-magmatic plots and chondrite normalised spider diagrams for Ulleungdo proximal units.

6.23……...94
Mineral vector diagrams indicating the impact of possible crystallising phenocryst phases on the Ulleungdo magma composition.
6.30……...……96
Histograms for selected trace elements in the Ulleungdo pyroclastic units.

List of Tables ***Page***

Chapter 2 Aims and Methodology
2.20 ……20
Details of Ulleungdo proximal deposits
2.21 ……26
Average major element analyses of MPI-DING reference materials analysed as secondary standards over a three day period
2.22……27
Typical operating conditions of the Thermo Element 2 ICP-MS coupled to a GeoLas 193 nm laser.
2.23…….....31
Major element composition of reference materials analysed in this study.
2.24…….....32
Major element composition of tephra samples analysed in this study

Chapter 3 LA-ICP-MS Analytical Considerations
3.10…….....38
Trace elements detectable and quantifiable in basic, intermediate and acidic glass compositions at 20 µm and 10 µm crater diameters.
3.11……39
Trace elements detectable and quantifiable in basic, intermediate and acidic glass compositions at 6 µm and 4 µm crater diameters
3.12……..40
Trace element concentrations (ppm) and SiO_2wt% and CaOwt% in MPI-DING and USGS reference materials
3.13……..41
Trace element concentrations (ppm) and SiO_2wt% and CaOwt% in a compositional suite of tephra samples.

Chapter 5 Calculation of New Fractionation Factors
5.10……76
New fractionation factors
Chapter 6 Characterisation of Ulleungdo Tephra
6.10……83
Major element (wt%) glass compositions for Ulleungdo units.
6.20……88
Trace element composition of Ulleungdo proximal units
6.30……97
Statistical distance test results for Ulleungdo proximal units.

Chapter 1 Tephrochronology and its Application

1.1 Introduction

Tephra is the collective term for pyroclastic materials that fall to the ground from volcanic eruption clouds (Francis and Oppenheimer, 2004). Large explosive eruptions are capable of dispersing and depositing volcanic ash over thousands of kilometres within a geologically 'instantaneous' time frame (Lowe, 2011). Therefore, tephra deposits from an eruption have the same age wherever they occur, forming isochronous markers which may be used to date and link geological, palaeoclimatic and archaeological sequences.

Tephrochronology is a geochronological technique involving the identification, correlation and dating of tephra (Thorarinsson, 1944). The method relies upon the accurate characterisation of tephra isochrons to establish a unique 'fingerprint', which may be used to compare and discriminate between tephra deposits (Lowe, 2011). This 'fingerprint' is ascertained through observation of the physical properties of both tephra deposits and glass shards and through undertaking geochemical analyses (Lowe, 2011), with the latter being the focus of this study. Individual glass shards are commonly analysed in order to obtain a geochemical fingerprint for correlation (Pearce *et al.,* 2004). Bulk tephra samples may contain reworked material and contaminant phenocrysts, xenocrysts, lithic clasts and detrital material, varying in quantity with distance from the volcanic vent (Lowe, 2011). Therefore, bulk samples may not reflect the actual eruption composition, causing difficulties when correlating tephra deposits (Pearce *et al.,* 2004).

Tephrochronology has been exploited by Quaternary researchers in order to provide chronology for high resolution palaeoclimate records, with global projects such as INTIMATE (Integration of ice core, marine, and terrestrial records: refining the record of the last glacial-interglacial transition), RESET (Response of humans to abrupt environmental transitions) and SUPRAnet (Studying uncertainty in palaeoenvironmental reconstruction - a net) all utilising tephrochronology extensively (Lowe, 2011). Improved methods of detection and bulk density separation have facilitated the recognition of cryptotephra (<125 μm) shards which are otherwise invisible to the naked eye, allowing distal tephra layers to be traced over greater distances (Blockley *et al.,* 2005; Lowe, 2011). However, distal shards are fine grained and often vesicular, limiting the area suitable for analysis to typically <10 μm (Hayward, 2011). At this resolution, analytical issues such as chemical modification may be encountered, reducing the confidence with which robust

correlations may be established. The focus of this study will be on the <10 µm crater diameter trace element characterisation of individual tephra glass shards.

1.2 Major Element Analysis

The appearance of the electron probe micro analyser (EPMA) in the 1960s allowed the analysis of individual tephra glass shards (Pearce *et al.,* 2004). Smith and Westgate (1969) were the first to undertake major element analysis of tephra glass shards using EPMA, a technique which is now well established. Tephra shards are mounted in resin and a focussed beam of electrons is directed at the chosen tephra shard, resulting in the emission of X-rays with particular wavelengths corresponding to elements and the wavelength intensity relating to elemental abundance (Coulter *et al.,* 2010; Lowe, 2011).

High precision EPMA analyses are required in order to define subtle compositional variations of tephra deposits. It is critical that appropriate beam conditions are used as alkali elements can migrate and affect the analysis (Humphreys *et al.,* 2006; Kuehn *et al.,* 2011). This migration from the upper 0.5- >1 µm of the sample occurs due to charging and heating (Hayward 2011). The process is characterised by an irreversible decline in Na and K counts, coupled with anomalously high Si and Al counts (Hayward, 2011). In order to overcome this chemical modification, abundant elements (e.g. Na) are counted first using a defocussed beam diameter of 5 – 20 µm and a <6 nA beam current, however, this hinders the use of narrow beams for the analysis of distal and vesicular tephra glass shards (Kuehn *et al.,* 2011). Hayward (2011) recently described the wavelength dispersive (WDS) analysis of tephra glass shards using a focussed beam of 3 µm diameter and a low beam current of (0.1 nA/ μm^2) with no observed alkali element migration, allowing cryptotephra deposits to be analysed with increased precision.

Currently, cryptotephra analysis is commonly undertaken using EPMA (Pearce *et al.,* 2011). However, rhyolitic and dacitic melts are often of a cotectic/eutectic minimum composition and may therefore be of a similar major element chemistry. If tephra deposits are of a similar major element composition, they may be distinguished by trace element analysis (Pearce *et al.,* 2011). Recent instrumental advances now allow trace element analysis of finer tephra glass shards with increased confidence.

1.3 Trace Element Analysis and the Development of LA-ICP-MS

Laser ablation inductively coupled plasma mass spectrometry (LA-ICP-MS) is a high-resolution method of geochemically characterising trace elements in tephra glass shards. More than 20-30 elements, including the rare earth elements (REE), can be determined in a ~20 s acquisition. Analyses at crater diameters of 20 µm and 10 µm are now routinely practised, with precisions of normally ±15-30% at 1 ppm and ±2-3% at 500 ppm for 10 µm craters (Pearce *et al.,* 2011). Lower limits of detection (LLD) are <1 ppm for most elements analysed using 10 µm crater diameters. Using a 193 nm Excimer laser, 4 µm crater diameters are feasible, allowing the analysis of minute quantities of tephra glass shards (Pearce *et al.,* 2011).

The ICP-MS was first developed as a commercial analytical instrument in the 1980s (Pearce *et al.,* 2007). Samples are introduced to the inductively coupled Ar plasma as an aerosol. Inside the plasma, the sample is exposed to atmospheric pressures and temperatures of 6000^{o}C where it is ionised to form positively charged ions (Pearce *et al.,* 2007). This ionised sample is 'pulled' through the aperture of the interface cone and the beam of ions is focused by ion lenses before it passes into the high vacuum mass spectrometer (Pearce *et al.,* 2007). Samples may be introduced as a solution (direct injection nebulisation) or vaporised from a solid using electro thermal vaporisation (ETV) or laser ablation (LA) (Pearce *et al.,* 2007). The introduction of solid samples to the plasma has various advantages; it achieves higher spatial resolutions and avoids complex sample preparation procedures associated with contamination and sample loss (Gray, 1985; Arrowsmith, 1987; Hirata *et al.,* 1997; Hergenroder, 2006).

LA-ICP-MS is a readily available trace element technique which is particularly suited to tephrochronology. LA-ICP-MS analysis has only achieved spatial resolutions comparable with EPMA in the last 10-15 years and recent analytical developments have been driven by the ambition to analyse increasingly distal tephra shards (Pearce *et al.,* 2011). Gray (1985) was the first to analyse solid geological materials using a JK type 694 nm wavelength ruby laser coupled to an ICP-MS. Arrowsmith (1987) later used a 1064 nm (infra-red) Nd:YAG laser coupled to an ICP-MS, with a longer duty cycle which produced a more consistent signal (Perkins *et al.,* 1997). Westgate *et al.* (1994) conducted the first analysis of ~80 µg of material from ~10-20 tephra glass shards bonded together with cyano-acrylate glue using a 1064 nm laser coupled to an ICP-MS.

Although Westgate *et al.* (1994) demonstrated the utility of the technique, the 1064 nm wavelength produced large crater diameters of ~150 µm and coupled poorly to the sample, due to poor absorption of the 1064 nm wavelength (Jackson *et al.*, 1992). Absorption relates to composition and crystallographic orientation of the sample - material containing transition metals with d orbital valence electrons (e.g. Fe) will absorb the 1064 nm radiation more readily (see Fig. 1.30) (Perkins *et al.*, 1997). When glass shards of a low absorption are analysed using a 1064 nm laser wavelength, much of the radiation passes through the grain and is instead absorbed by the epoxy resin. This results in the production of large volumes of vapour and the collapse of the shard – a process known as catastrophic ablation (Perkins *et al.*, 1997).

Jackson *et al.* (1992) and Perkins *et al.* (1997) reported improved absorption and decrease in catastrophic ablation at shorter UV wavelengths. Thus, IR laser systems were gradually replaced by UV wavelengths. In the mid '90s Nd: YAG 1064 nm laser wavelengths were quadrupled to 266 nm (UV) wavelengths (see Pearce *et al.*, 1999) and in the late '90s frequency quintupled 213 nm (UV) laser wavelengths were achieved (see Jeffries *et al.*, 1996), allowing the efficient ablation and analysis of smaller sample quantities. In the early 2000s ArF_2 Excimer lasers (excited state dimer lasers), operating at 193 nm (deep UV), became available. Excimer lasers couple more efficiently to the sample and reduce peripheral damage to the glass shard (Pearce *et al.*, 2011). The more efficient ablation also produces an improved aerosol, which is less susceptible to element fractionation (the non-stoichiometric removal of material from the sample) (Gunther and Hattendorf, 2005; Pearce *et al.*, 2011). Excimer lasers (see Fig. 1.31) also offer increased sensitivity and lower limits of detection (LLD).

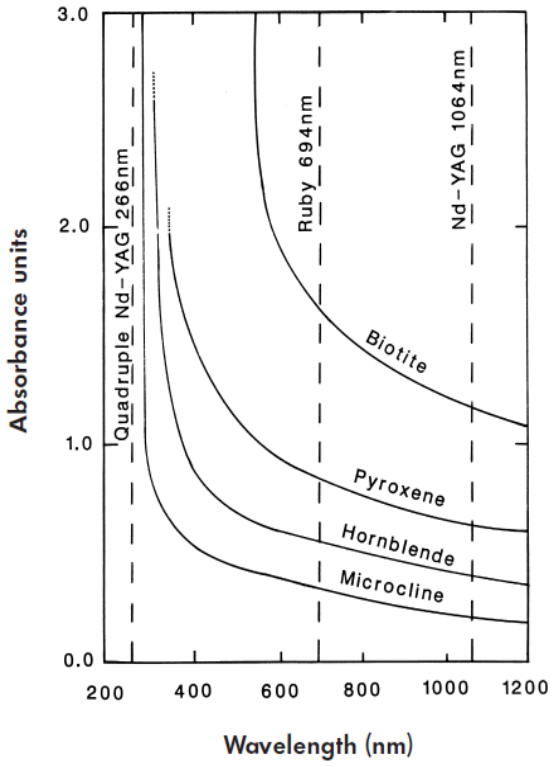

Fig.1.30 Absorption of UV, visible and near-infrared wavelengths for biotite, pyroxene, hornblende and microcline. As seen, better absorption is achieved at higher frequency wavelengths (from Perkins et al., 1997).

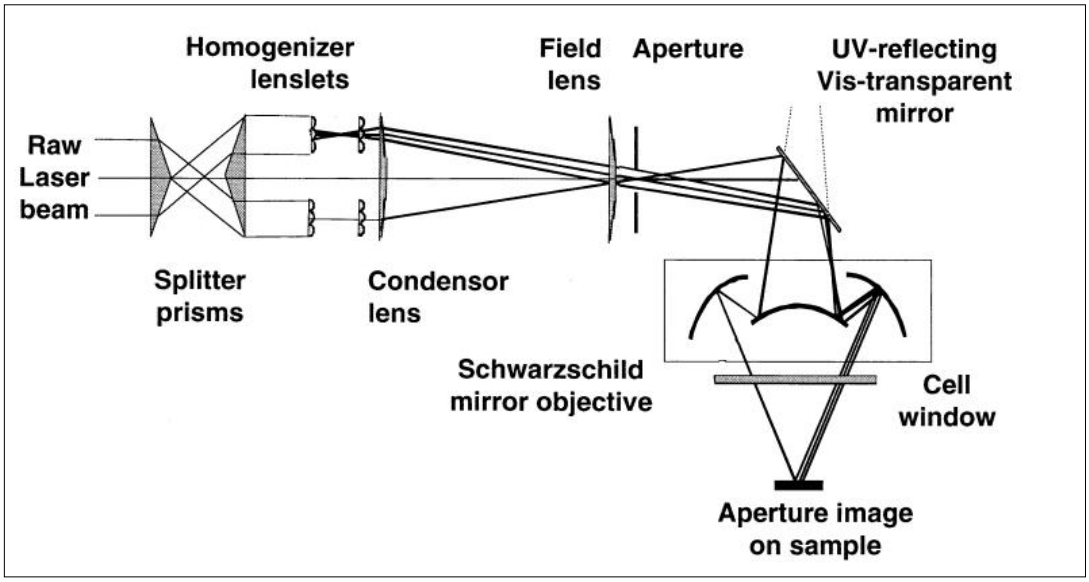

Fig. 1.31 Optical path of GeoLas ArF Excimer laser (Compex 110 Lambda Physik) used in this study (from Heinrich *et al.,* 2003). The rectangular raw beam (10 x 25 mm) is divided into two parallel beams by prisms, these pass through 2 sets of 18 x 18 lenslets followed by a condenser lens, concentraring the beam into a homogeneous area of ~ 3 x 3 mm. An aperture (used to change the crater diameter at the sample surface) then blocks out some of the laser which is then demagnified by a 25 x mirror objective onto the sample (Heinrich *et al.,* 2003).

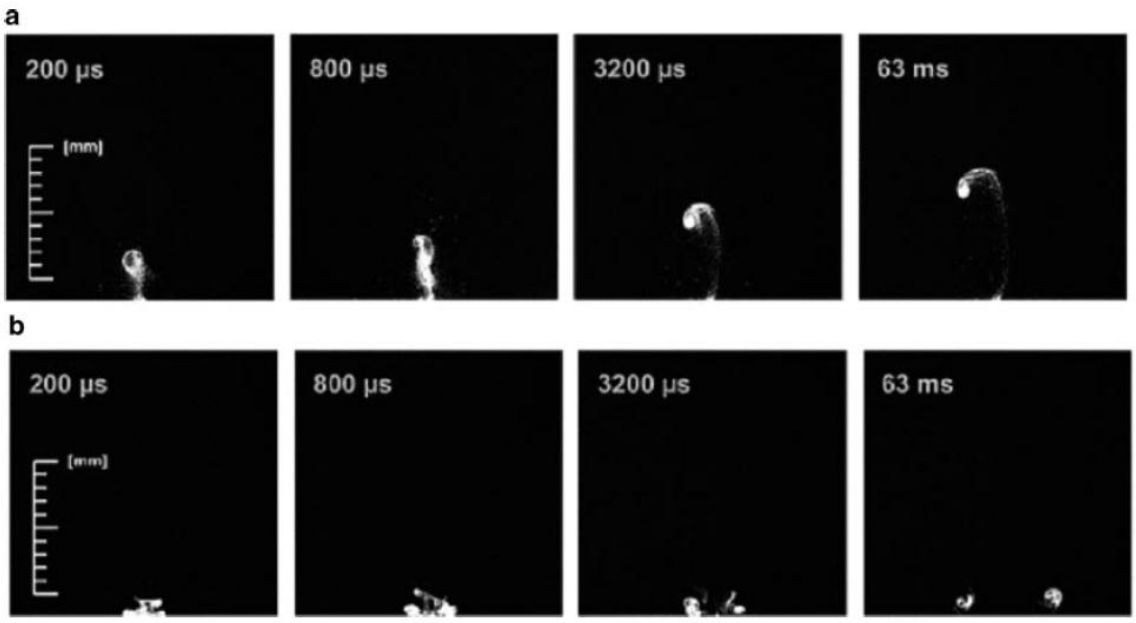

Fig.1.32. Expansion of NIR-ns-LA generated aerosols over time using (a) He as a carrier gas and (b) Ar as a carrier gas (from Pisonero and Gunther, 2008)

Pearce *et al.* (2011) illustrated instrumental developments in the Laboratories at Aberystwyth. Whilst using a 266 nm laser system coupled to either a PQII+/S-option quadrupole based ICP-MS (1996) or a VG PQII+STE (2004) the LLD is 0.1 ppm at 30-50 µm crater diameters. Using a 193 nm laser system coupled to a PQII+STE ICP-MS (2007) the LLD for many elements is 0.1 ppm at 10 µm crater diameters.

LA-ICP-MS sensitivity is improved further through using helium as a carrier gas. Helium has a lower density and volume than the commonly used Ar carrier gas (Eggins *et al.*, 1998). Pisonero and Gunther (2008) demonstrated that the two gases show different dispersal patterns (seen in Fig. 1.32), with He transporting small particles more effectively. Pearce *et al.* (2004) reported a 2-3 fold increase in sensitivity when He was used as a carrier gas instead of Ar. However, the study also revealed an increase in the ^{29}Si blank associated with the use of He, worsening the signal/background ratio, particularly when analysing rhyolites. To increase sensitivity where Ar is used as a carrier gas, Pearce *et al.* (2011) modified the configuration of gas flows so that 35% of the Ar gas flow is diverted away from the sample and recombined downstream in a tangential mixer (Fig. 1.33). For the majority of elements, this modification resulted in a 30% sensitivity increase compared with analyses where 100% Ar was allowed to pass over the sample.

With increased ablation efficiency and improvements in sensitivity, minute quantities of distal tephra glass shards may be analysed successfully, with analyses at 20 µm and 10 µm crater diameters now routinely achieved (Pearce *et al.*, 2011). However, analyses of micro-shards (<32 µm diameter) using <10µm diameter craters are subject to the effects of elemental fractionation.

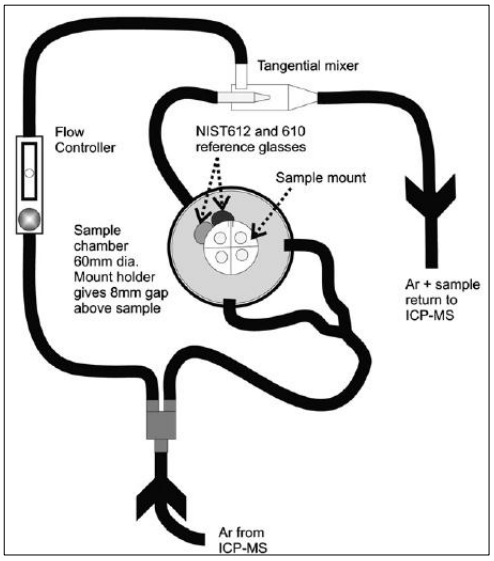

Fig. 1.33 Schematic illustrating the diversion of Ar around some of the sample chamber (from Pearce et al., 2011), this configuration is used in this study.

1.4 Element Fractionation

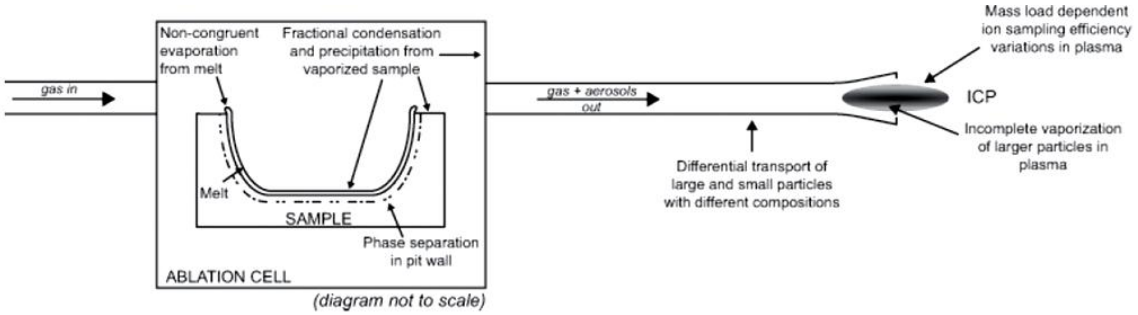

Fig. 1.40 Possible causes and locations of fractionation in LA-ICP-MS (from Sylvester, 2008).

Variations in the elemental abundance of a sample during LA-ICP-MS analysis relative to its reported composition are the result of element fractionation (Pearce *et al.,* 2007; Sylvester, 2008). Several processes operating within the ICP-MS may contribute to element fractionation such as, ablation, aerosol transport and vaporization, atomization and ionization within the ICP (see Fig. 1.40) (Gunther and Kroslakova, 2006; Sylvester, 2008; Tomlinson *et al.,* 2010). However, the ablation process is primarily responsible for aerosol production and is widely reputed to be a significant cause of elemental fractionation (Gunther and Kroslakova, 2006). Therefore fractionation associated with ablation will be the focus of this study.

Fractionation becomes an issue where analyses are calibrated against reference materials of a different matrix, which do not respond to fractionation in the same manner as the sample (Pearce *et al.,* 2011; Sylvester, 2008). Most geoanalysts calibrate using NIST (National Institute of Standards and Technology) 610 and NIST 612, these partially certified reference materials are spiked with high concentrations of all trace elements (~450 ppm and ~50 ppm, respectively), and are thus ideal for instrument calibration (Pearce *et al.,* 1997; Jochum, *et al.,* 2005). The NIST reference materials are, however, constituted of synthetic soda-lime silicate with a very different matrix to that of any geological sample. This causes analytical biases as a result of differential fractionation of the sample and the reference material (Jochum *et al.,* 2005; Pearce *et al.,* 2011). Due to this, a suite of USGS and MPI-DING (Max-Planck Institute) reference materials of natural composition have been manufactured; however, these are commonly used as secondary standards due to their low trace element abundance (Jochum *et al.,* 2005).

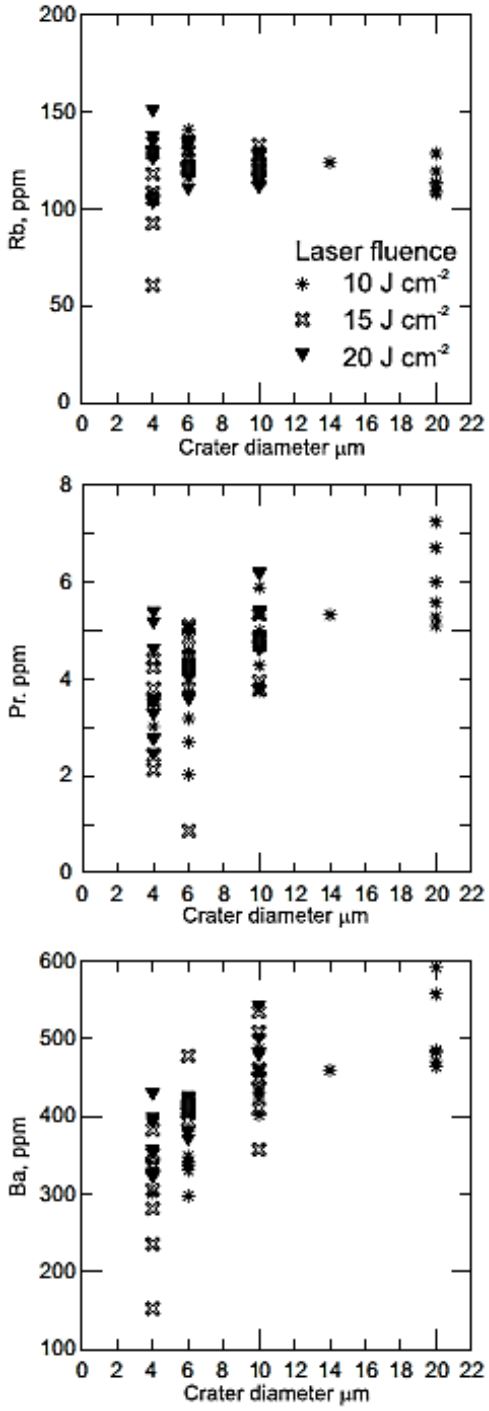

Fig. 1.41 Minoan glass (Santorini) analyses. Graphs show Ba, Pr and Rb concentrations (ppm) against crater size (20 µm, 10 µm, 6 µm, 4 µm). Analyses were conducted using a 193 nm laser operating at 5 Hz, <20 µm craters were performed at 10, 15 and 20 Jcm^{-2}, 4 µm craters were conducted exclusively at 10 Jcm^{-2}. Calibration was against 20 µm NIST 612 analyses at 5 Hz and 10 Jcm^{-2} (from Pearce et al., 2011).

Pearce *et al.* (2011) investigated element fractionation and its possible causes. A series of analyses on the MPI-DING reference glasses; BHVO-2G, BCR-2G (basic), T1-G (intermediate) and ATHO-G (acidic) were conducted at 20 µm crater diameters, using a 193 nm laser operating at 10 Jcm^{-2} coupled to a Thermo Element 2 ICP-MS at Aberystwyth. Analyses were calibrated against 20 µm NIST 612 spectra with ^{29}Si as the internal standard. Measured concentrations generally compared well with certified concentrations from GeoReM reference material database (see Jochum *et al.*, 2005).

However, some measured concentrations were systematically offset from the reported concentrations. The rare earth elements (REE) and high field strength elements (HFSE) (e.g. Zr, Nb, Ta) were typically underestimated, with REE measured at 80-90% of their certified concentrations. The study found all compositions were similarly affected by element fractionation. However, Pb concentrations were underrepresented in acidic reference glasses and overrepresented in basic reference materials, with Cs showing the opposite behaviour to that of Pb.

This analytical offset is the result of element fractionation (Perkins *et al.*, 1997; Gunther and Hattendorf, 2005; Sylvester, 2008; Pearce

et al., 2011).

Pearce *et al.* (2011) calculated an 'overall fractionation factor' to compensate for element fractionation, this may be applied to glass shard analyses of any composition using 20 µm and 10 µm crater diameters and where ^{29}Si is the internal standard. Application of these fractionation factors to 20 µm and 10 µm crater diameter analyses of proximal tephra from the Minoan eruption, Santorini, improved analytical accuracy.

In addition, Pearce *et al.* (2011) found concentrations became increasingly offset with decreasing crater diameter. Figure 1.41 shows Minoan glass shard concentrations measured using crater diameters of 20 µm, 10 µm, 6 µm and 4 µm and laser fluences of 10 Jcm^{-2}, 15 Jcm^{-2} and 10 Jcm^{-2}. Barium and Pr concentrations are increasingly underrepresented and Rb concentrations are increasingly overrepresented with decreasing crater diameter. It is not possible to correct for these offsets at 6 µm and 4 µm by calibration against NIST 612 spectra of the same crater diameter. This is due to low counts and large errors at <10 µm crater diameters, giving unknown analyses with low analytical precisions (Pearce *et al.*, 2011).

Pearce *et al.* (2011) described a link between element fractionation and laser fluence. This is seen in Fig. 1.41, where analyses conducted on Minoan glass shards appear less fractionated at a laser fluence of 20 Jcm^{-2} than at 10 Jcm^{-2}. Pearce *et al.* (2011) ablated craters of 40 µm, 20 µm, 10 µm, 6 µm and 4 µm diameters into obsidian from Chabbi, Ethiopia, using a 193 nm GeoLas laser with a 10 Jcm^{-2} laser fluence and a 0.5 mm thick mask.

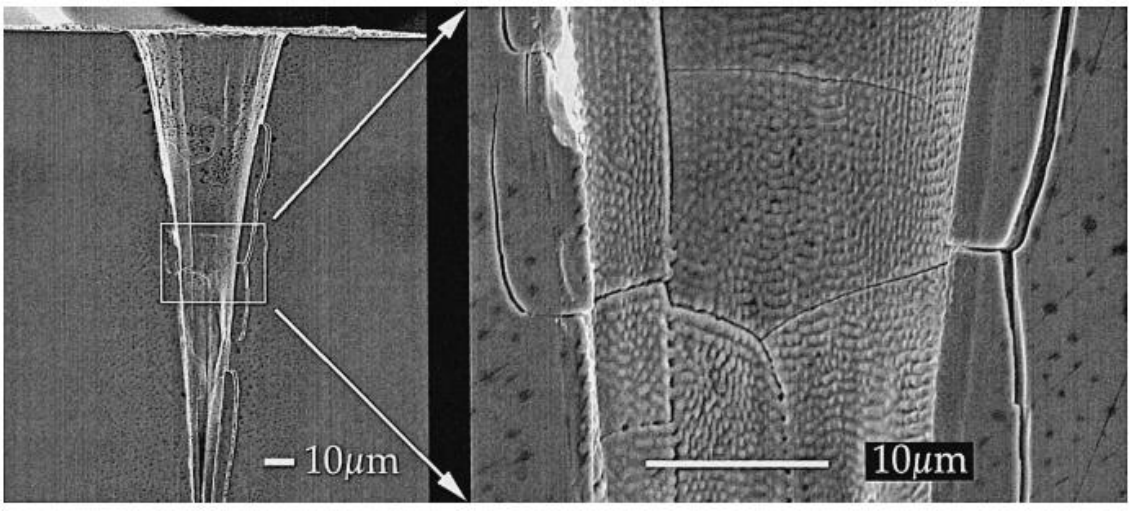

Fig. 1.42 SEM images of the development of melt films lining craters ablated into NIST 612 using an ArF Excimer laser at a constant fluence of 13 Jcm^{-2} coupled to a quadrupole ICP-MS (from Eggins *et al.*, 1998).

The aspect ratio of the craters varies as a function of their crater diameter (Pearce *et al.* 2011). The 20 µm to 40 µm crater diameter ablation pits are near cylindrical and 20 µm deep. The 10 µm diameter craters are flat bottomed and 15 µm deep. Craters of 4 µm diameter resemble inverted cones with depths of 2 µm (see Fig. 1.43).

Pearce *et al.* (2011) suggested the changing aspect ratio of ablation pits with diameter is associated with attenuation of the laser beam as it passes through one of a series of preformed holes in the 0.5 mm mask used to alter the crater diameter at the sample surface (see Fig.1.31). When analysing at crater diameters of >20 µm, the preformed holes in the 0.5 mm thick mask have a greater diameter than the mask thickness. However, the mask thickness (500 µm) is greater than the aperture in the mask used to create <10 µm crater diameters. Therefore laser energy is attenuated and scattered as it passes through the mask, causing changes in the beam profile and subsequent changes in crater shape at the sample surface. This attenuation is reduced at a higher laser fluence of 20 Jcm^{-2} as evidenced by the decrease in element fractionation of the Minoan glass shard analyses at 20 Jcm^{-2}.

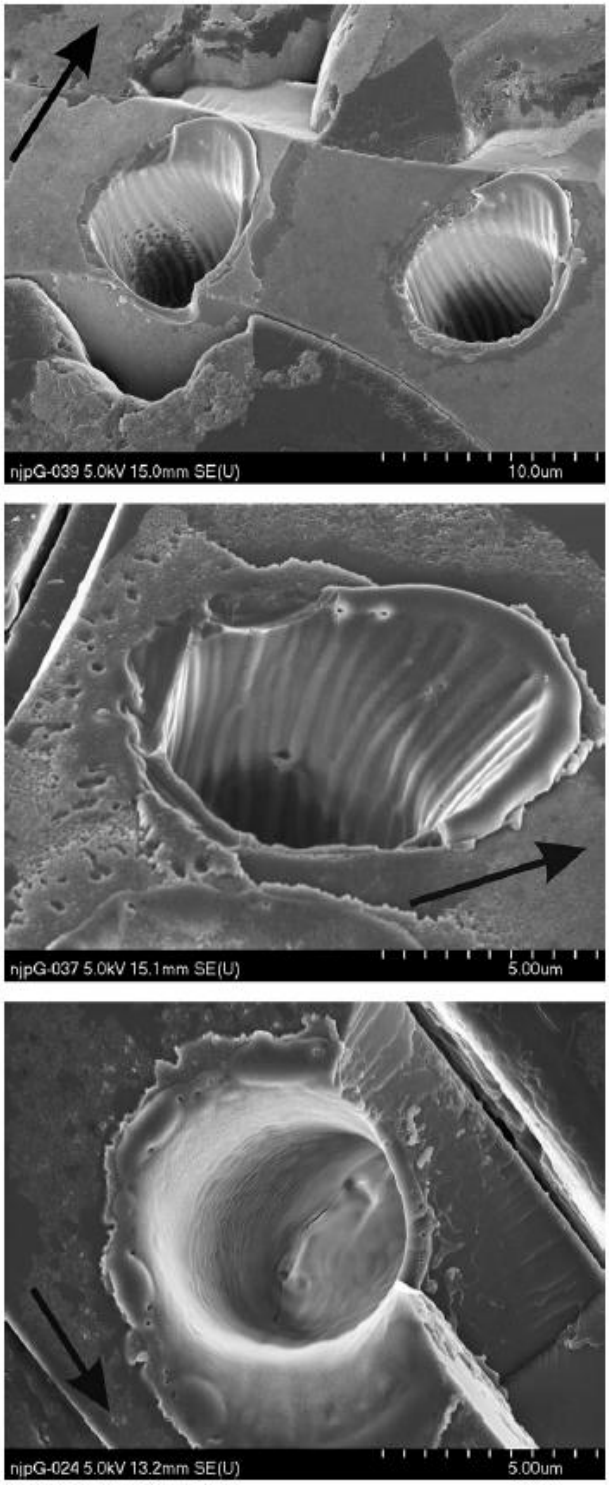

Fig. 1.43 SEM images of surface condensate formation within 4µm and 6µm craters in Minoan glass, Santorini. A 10 Jcm^{-2} and 5 Hz 193 nm laser and the thinned 0.1 mm mask were used. Arrows denote direction of gas flow (Pearce *et al.*, 2011).

A 0.3 mm thick mask was obtained and the area around the apertures was thinned so that none of the preformed holes had narrower diameters than the thickness of the mask. This modification generated shallow, conical 6 µm and 4 µm craters.

The change in aspect ratio as a function of crater diameter, described by Pearce *et al.* (2011), was also noted by Eggins *et al.* (1998) and Mank and Mason (1999). Mank and Mason (1999) described an increase in element fractionation with increasing crater depth, stating that when the depth/crater diameter ratio exceeded 6 there was a 50% reduction in signal. Eggins *et al.* (1998) also described the formation of increasingly convoluted ablation pits with increasing crater depth, associated with signal decay caused by a reduction in ablated mass. In addition, Eggins *et al.* (1998) described the development of a surface condensate lining the walls of the ablation pits, exhibiting sequential cooling of the refractory followed by volatile phases over time (see Fig. 1.42). This surface condensate has been widely cited as a source of element fractionation (Eggins *et al.,* 1998; Hergenröder, 2006; Sylvester, 2008; Pearce *et al.,* 2011). Pearce *et al.* (2011) described the presence of a similar 0.3-0.5 µm melt film lining the interior of 20 µm, 10 µm, 6 µm and 4 µm diameter craters ablated into Minoan glass shards. Pearce *et al.* (2011) suggested elements are selectively removed or retained within this melt film. Alkali elements (e.g. Rb) are volatilised from the melt and HFSE (e.g. Zr) are retained within the melt film, causing measured concentrations to be overrepresented and underestimated, respectively. The response of elements to fractionation has been widely studied. Elements of a small ionic radius and high condensation temperature are generally strongly bound within the silicate matrix and thus less efficiently ablated (Jeffries *et al.,* 1997; Gaboardi and Humayan, 2009). Pearce *et al.* (2011) associated the increase in fractionation with decreasing crater diameter to the subsequent variation in the melt film volume relative to the volume of material ablated.

Pearce *et al.* (2011) found sample composition influenced the extent of element fractionation. Matrix controls have been widely cited as a key influence on element fractionation (Gunther and Hattendorf, 2005; Sylvester, 2008; Pearce *et al.,* 2011; Czas *et al.,* 2012). Some studies indicate a simple link between sample Fe and SiO_2 concentrations and element fractionation (Gaboardi and Humayan, 2009; Czas *et al.,* 2012). These factors also determine the efficiency of laser energy absorbance; transparent samples contain higher SiO_2 and FeO concentrations and couple less efficiently to the laser. This produces

larger particles which are volatilised less effectively in the ICP-MS (Horn and Gunther, 2002; Sylvester, 2008).

Gaboardi and Humayan (2009) analysed a series of NIST partially certified reference materials with varying Fe concentrations at a laser wavelength of 213 nm (see Fig. 1.44). NIST 614 (19 ppm Fe) was found to show more fractionation than NIST 612 (51 ppm Fe), suggesting more transparent samples with lower Fe concentrations couple poorly to the 213 nm wavelength laser. The inefficient ablation of transparent samples may release particles of >125 nm diameter which vaporize incompletely and fractionate more dramatically (see Fig. 1.45). Czas *et al.* (2012) compared the element fractionation of the reference materials NIST 616, 614, 612 and 610, BAM S005A & B and GSD-1G and GSE-1G. Using a 193 nm laser coupled to a Thermo Element 2 ICP-MS, Czas *et al.* (2012) found no evidence for element fractionation associated with varying FeO concentrations. Czas *et al.* (2012) stated this may be due to better coupling of the 193 nm laser to the sample. However, Czas *et al.* (2012) used large (> 75 µm) crater diameters, less effected by element fractionation (Pearce *et al.*, 2011), and calibrated against samples of the same matrix. Furthermore, NIST reference glasses are spiked with high concentrations of ~60 elements which collectively denote the darker colour of this reference glass. This may suggest the link between element fractionation and parameters such as FeOwt% and colour are not as clear as suggested (Pearce *et al.*, 2011).

Pearce *et al.* (2011) stated that element fractionation may instead be associated with silicate melt structure (polymerisation). Polymerisation gives an indication of melt structure through relating the number of non-bridging oxygens (NBO) to the number of tetrahedrally organised oxygens (T) in a silicate melt (Mysen, 1983). Pearce *et al.* (2011) calculated the polymerisation of four calc-alkaline samples using the NBO/T calculation as established by Mysen (1983). A linear relationship between fractionation and polymerisation exists, with the HFSE most fractionated in polymerised samples (higher SiO_2) analysed using the smallest crater diameters (Fig. 1.46).

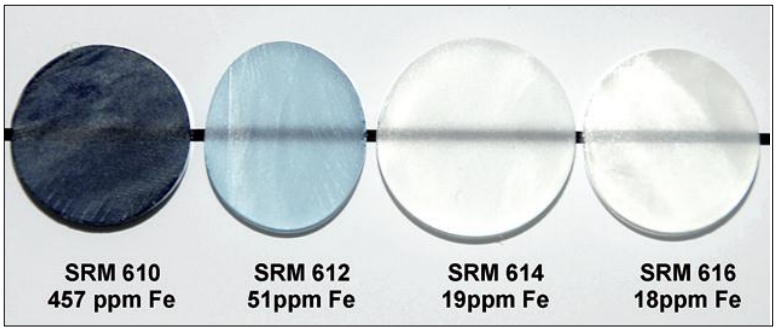

Fig.1.44 Increasing transparency with decreasing Fe concentration of NIST SRM reference glasses (from Gaboardi and Humayan, 2009)

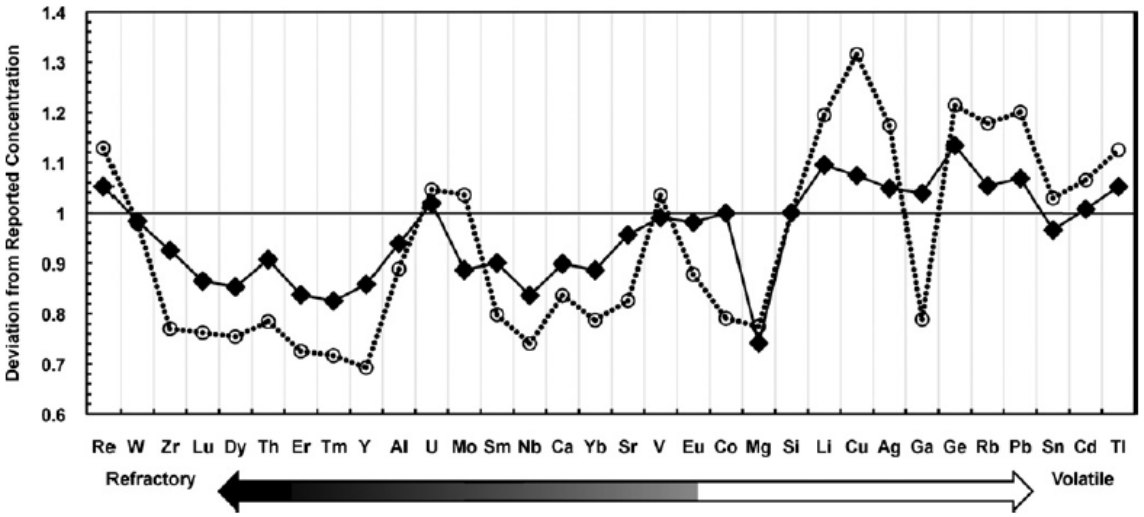

Fig.1.45 Measured concentrations divided by reported concentrations and plotted against element behaviour for: NIST 612 (solid lines, ~51 ppm Fe) and NIST 614 (~19 ppm Fe). Analyses calibrated against NIST 610 (~457 ppm Fe). The NIST 614, with lower Fe concentrations, appears more fractionated (from Gaboardi and Humayan, 2009).

Pearce *et al.* (2011) related this increase in fractionation with increasing polymerisation to changes in trace element coordination with variations in sample composition. Numerous studies have cited the influence of melt composition on trace element behaviour (Ponader and Brown, 1989; Prowatke and Klemme, 2005; 2006). Prowatke and Klemme (2005) demonstrated that partition coefficients (*D*, a measure of elements preference for the melt phase) for REE and Th, Nb and Ta vary significantly with melt composition. This can be explained by changing coordination and regularity of REE polyhedra within silicate melts, coincident with compositional variation (Prowatke and Klemme, 2005).

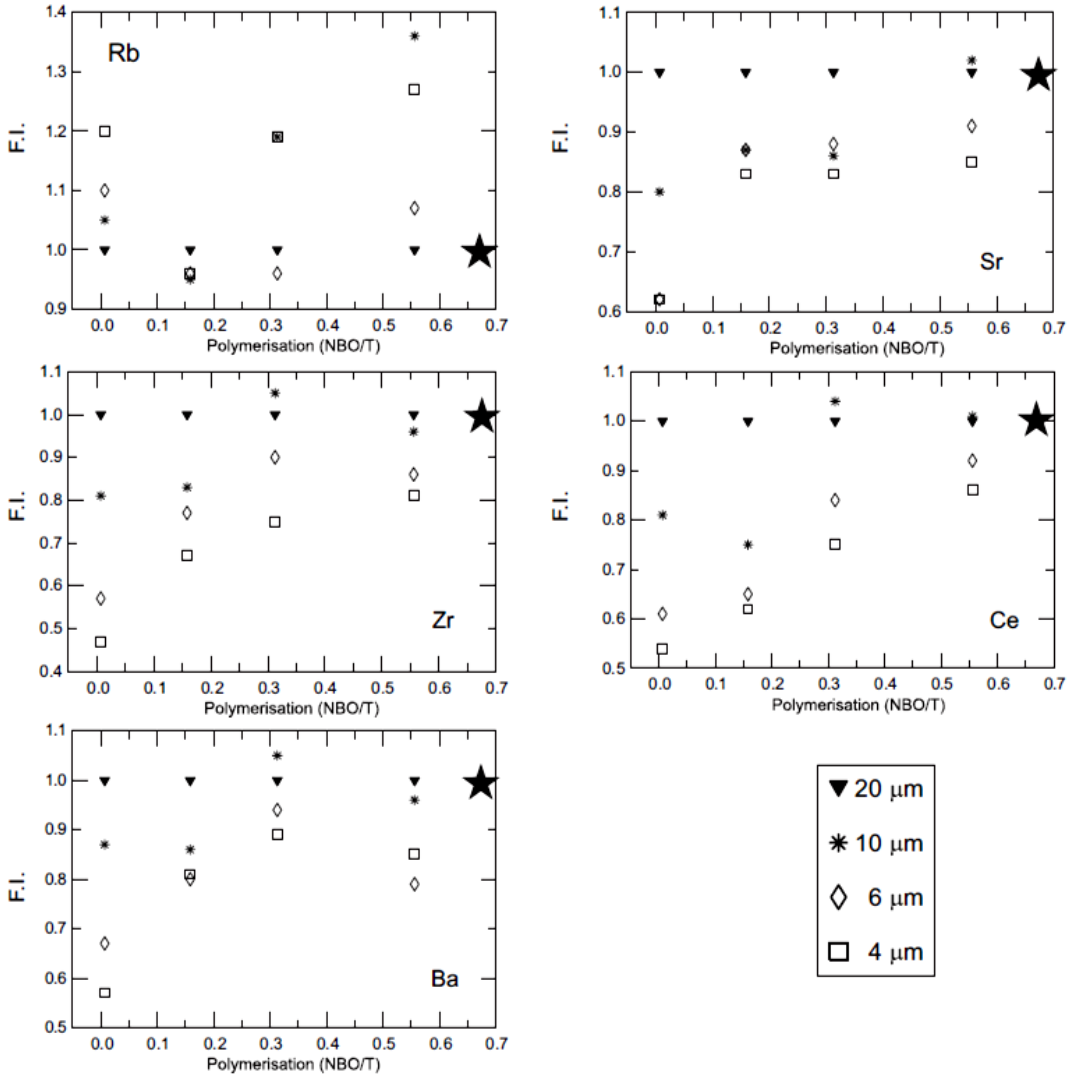

Fig.1.46 Fractionation index (concentration at *x* µm/ concentration at 20 µm) of Ba, Zr, Ce, Rb, Sr plotted against polymerisation (NBO/T) (Mysen, 1983) for a range of silicate glass compositions (Santorini, UT2015, UT1412 and UT2252 and NIST 612) using a 193 nm laser operating at 5 Hz, analyses at 6 µm and 4 µm were obtained using the thinned mask (0.3 mm) (from Pearce *et al.*, 2011). Analyses demonstrate increased fractionation at smaller crater sizes and with increasing polymerisation (lower NBO/T).

Coordination relates to the number of molecular/ionic groups (ligands) bound to a central ion, whilst the coordination number relates to the number of ligand donor atoms bonding with the central ion (Clugston and Flemming, 2000). Ponader and Brown (1989) observed a six-fold coordination of Gd in melts with NBO/T= 0, a six to eight-fold coordination of Gd in melts with NBO/T=0.29 and an eight fold coordination of Gd in melts with NBO/T=0.67.

Therefore, melt composition changes may alter the preference of trace elements for the melt film forming along the crater walls during ablation and alter how strongly elements are bonded within the sample matrix. This may explain why Pearce *et al.* (2011) observed variations in trace element fractionation in differently polymerised samples. However, Prowatke and Klemme (2005) noted that partition coefficients for monovalent and divalent cations and Zr and Hf do not vary significantly with melt composition, contrasting with the variable fractionation of Zr with composition noted by Pearce *et al.* (2011).

In summary, Pearce *et al.* (2011) demonstrated the control of crater diameter, laser operating conditions and sample composition on element fractionation. Pearce *et al.* (2011) corrected for element fractionation of 20 µm and 10 µm crater diameters and cited the need for further research to compensate for compositionally related fractionation at <10 µm crater diameters. This study will further investigate the findings of Pearce *et al.* (2011).

1.5 The Application of LA-ICP-MS to Tephrochronology

The application of LA-ICP-MS to tephrochronology is reviewed extensively by Pearce *et al.* (2004; 2007), Tomlinson *et al.* (2010) and Lowe (2011).

The development of LA-ICP-MS has revolutionised tephrochronology (Bryant *et al.*,1999; Lowe, 2011). Westgate *et al.* (1994) were the first to use LA-ICP-MS to characterise a bulk tephra sample. An IR laser was used to ablate ~80 µg of material from 10-20 tephra shards mounted in cyano-acrylate glue (Pearce *et al.*, 2007; 2011). Analyses were calibrated using Ce as an internal standard, requiring the use of another trace element analytical technique. Pearce *et al.* (1996) offered a solution, demonstrating the effective use of a minor isotope of a major element (Si, Ca or Fe), all frequently measured using EPMA, as an internal standard. Analyses were first undertaken on individual glass shards during the late 1990s using 40-100 µm crater diameters (Bryant *et al.*, 1999; Pearce *et al.*, 2011). Trace element analysis has since been utilised in numerous studies, notably the correlation of distal tephra from Golhisar Gölu, Turkey, to the Minoan eruption, Santorini (Eastwood *et al.*, 1998; 1999, Pearce *et al.*, 2002) and to correlate tephra from the Auckland region of New Zealand to the Waiuku tephra (Pearce *et al.*, 2007). The identification of microtephra deposits, containing glass shards of <32 µm, has significantly widened the distance over which tephra deposits can be correlated (Pollard *et al.*, 2006). The ambition to analyse distal tephra has also pushed forward LA-ICP-MS analytical improvements (Pearce *et al.*, 2007; 2011).

In the following section a specific instance where tephrochronology has been exploited to correlate and date an important palaeoclimatic archive is explored in detail.

1.6 Correlation of the Suigetsu Lacustrine Archive with Ulleungdo, Korea

1.6.1 Lake Suigetsu

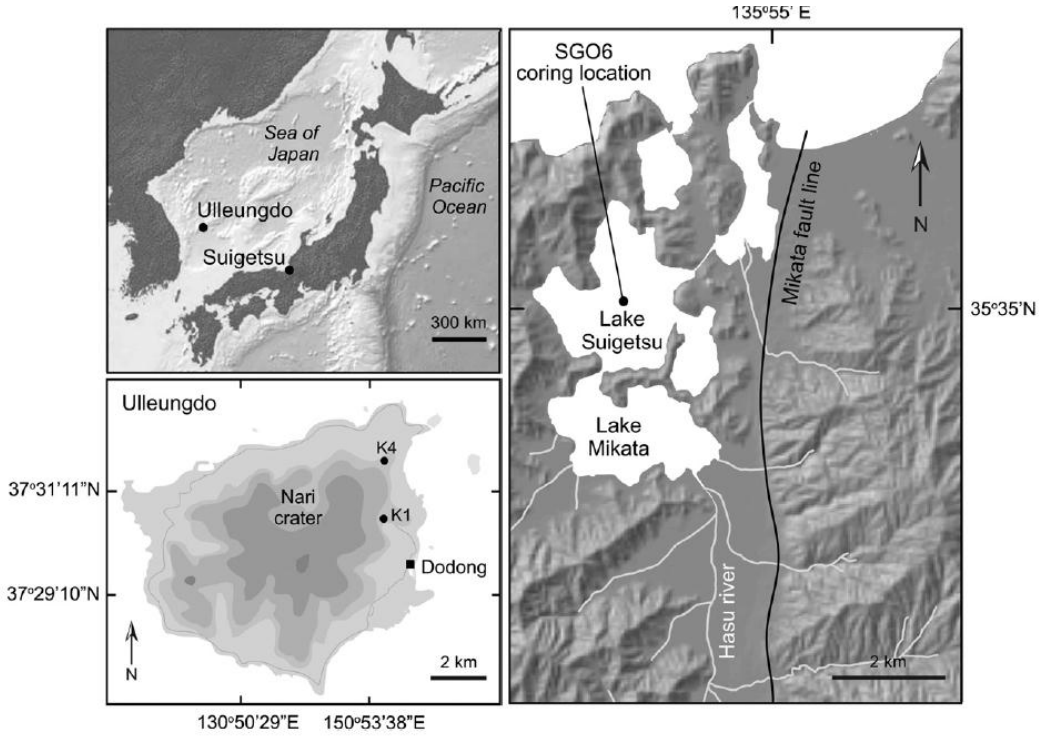

Fig.1.60 Location of Lake Suigetsu, Japan, and Ulleungdo, South Korea (from Smith *et al.,* 2011a)

For several decades, Lake Suigetsu, Honshu Island, Japan, (35°35'N, 135°53'E) has been regarded as a valuable palaeoenvironmental archive (Fig. 1.60). Lake Suigetsu is a tectonic lake situated on Honshu Island, Japan, lying close to the Sea of Japan (Nakagawa *et al.,* 2011). The lake has an area of 4.3 km^2 and reaches depths of 34 m (Nakagawa *et al.,* 2011). Lake Suigetsu is sheltered, receives little inflow of water, is subject to strong seasonal variations and has been surrounded by vegetation since the Last Glacial Maximum (Nakagawa *et al.,* 2011). These factors have ensured that the lake sediment has not been disturbed, thus annual layers (varves) can be seen through large portions of the record, providing an ideal palaeoclimate archive (Nakagawa *et al.,* 2011). Lake Suigetsu is a crucial mid-latitude archive, providing information on how the Asian climate relates to that recorded at the poles (Smith *et al.,* 2011a)

1.6.2 The SG06 Archive

In 2006, the SG06 sediment core was extracted from Lake Suigetsu as part of the 'Suigetsu Varves 2006' project, providing one of the most well constrained mid-latitude palaeoclimatic archives (Smith *et al.,* 2011a). The SG06 core measures 73 m (150 kyrs of continuous sedimentation) and is annually varved between ~10 and 65 kyrs (see Fig. 1.61). The core contains numerous plant macrofossils which have been used to construct a purely terrestrial radiocarbon calibration, thereby avoiding uncertainties associated with marine records (Bronk Ramsey *et al.,* 2012).

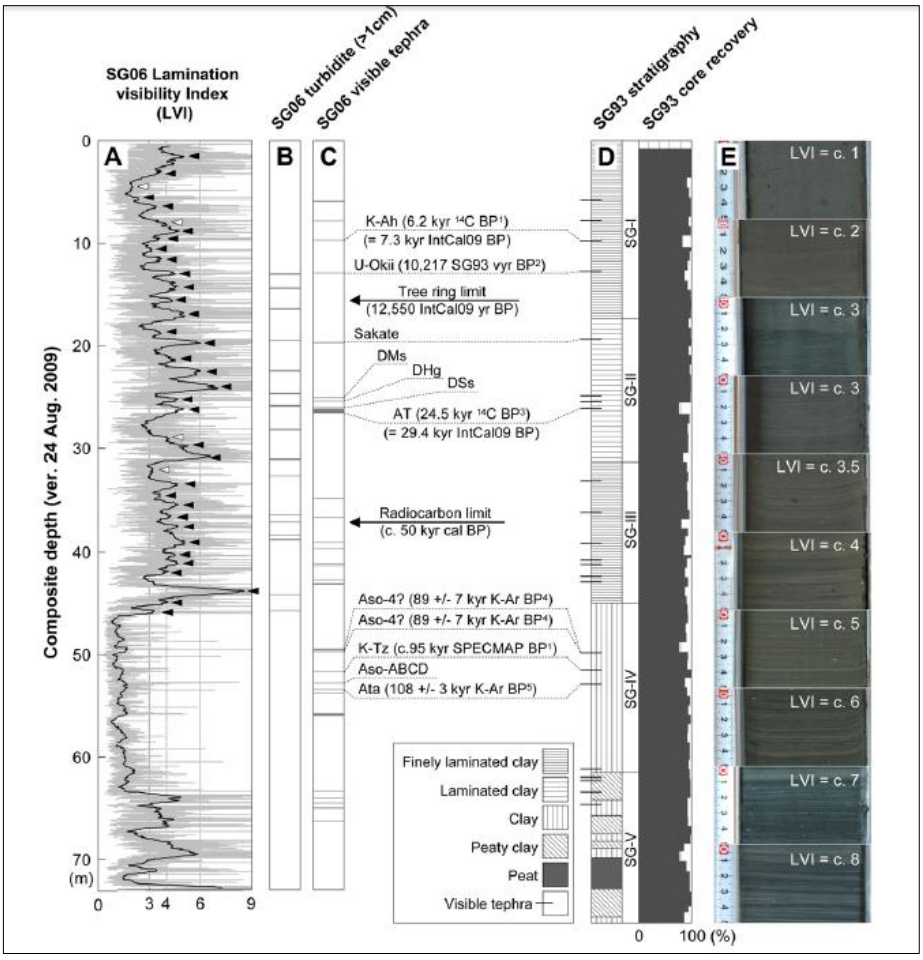

Fig. 1.61 SG06 core lamination, event and tephra stratigraphy. A) Lamination visibility index (LVI) raw data (grey curve) and 50cm moving average (black line), B) turbidite layer distribution, C) tephra distribution, D) core stratigraphy, E) appearance of fresh core (from Smith *et al.,* 2011a).

The archive contains ~30 tephra layers, many derived from the Japanese volcanic arc (Fig. 1.61 C) (Nagakawa *et al.,* 2011; Smith *et al.,* 2011a; Smith *et al.,* submitted). A tephra found at 1286.1-1288.0 cm composite depth has previously been defined as the Ulleungdo-

Oki (U-Oki) Korean tephra using its physical characteristics and stratigraphic position (Takemura, 1994; Smith *et al.,* 2011a). The presence of this tephra within the lower portion of the tree ring-derived IntCal09 radiocarbon calibration curve has enabled the calculation of a terrestrial radiocarbon age for the 1288 tephra through wiggle-matching radiocarbon measurements of macrofossils either side to the calibration model (Smith *et al.,* 2011a; Staff *et al.,* 2011). Using this method, the 1288 tephra was found to have a modelled age of 10.202-10.231 cal. ka BP (68.2% probability) (Smith *et al.,* 2011a; Staff *et al.,* 2011).

In order to independently verify this age and constrain the floating varve chronology to an absolute age, Smith *et al.* (2011a) correlated the 1288 tephra to Ulleungdo proximal deposits, more suitable for $^{40}Ar/^{39}Ar$ dating.

1.6.3 Ulleungdo Tephra

The U-Oki tephra (10.7 cal ka BP) forms a significant Holocene marker across the southern Sea of Japan, central Honshu and the north-western Pacific. The U-Oki tephra is uniquely alkaline (6.1-7.2wt% K_2O, 5.8-7.7wt% Na_2O) compared with the calc-alkaline nature of many Japanese tephra layers within SG06 (Smith *et al.,* 2011a). The distribution of the U-Oki tephra across the Sea of Japan (see Fig. 1.62) suggests it originates from Ulleungdo, Korea (also known as Ullreung or Ulleung) (Smith *et al.,* 2011a).

Ulleungdo is located within the Japanese back-arc basin, 110 km from the Korean peninsula, with its 120 km^2 area representing the top of a dormant stratovolcano (Kim *et al.,* 2008; Smith *et al.,* 2011a). Lying at the centre of the island is the Nari caldera – measuring 2 km in diameter (Kim *et al.,* 2008). Machida *et al.* (1984) defined seven pyroclastic units on Ulleungdo, younging from U7 to U1, comprised of ash and pumice emplaced as falls and/or by pyroclastic flows. Ulleungdo volcanic deposits range in composition from basalts (1.37-0.7 Ma), through to trachytes (0.73-0.24 Ma), and finally to trachyandesites (<6.3 kyrs) (Kim *et al.,* 2008; Smith *et al.,* 2011a; submitted).

Okuno *et al.* (2010) correlated the U-Oki tephra to the thickest Ulleungdo pyroclastic unit, U4, based on radiocarbon measurements beneath U4 (13.8-14.0 cal. kyrs BP; 2σ) and above (8.2-9.0 cal kyrs BP; 2σ). Smith *et al.* (2011a) found the SG06-1288 tephra to have an identical major element chemistry to that of U4 of Ulleungdo. Proximal tephra from U4 contains large sanidine crystals suitable for $^{40}Ar/^{39}Ar$ dating, yielding an age of 10,000 ± 300 cal yrs BP and independently verifying the SG06 core ^{14}C chronology (Smith *et al.,* 2011a; Staff *et al.,* 2011). Preliminary work by Dr Victoria Smith (RLAHA, Oxford) suggests that pyroclastic Ulleungdo units share a similar major element chemistry and are

highly pumiceous. Trace element data using small crater diameters is therefore critical in order to accurately characterise and establish robust correlations between the Ulleungdo proximal units and the SG06 archive. This will allow further $^{40}Ar/^{39}Ar$ dating of the Ulleungdo units, which may be applied to the SG06 age model (Smith, *pers. comm*.)

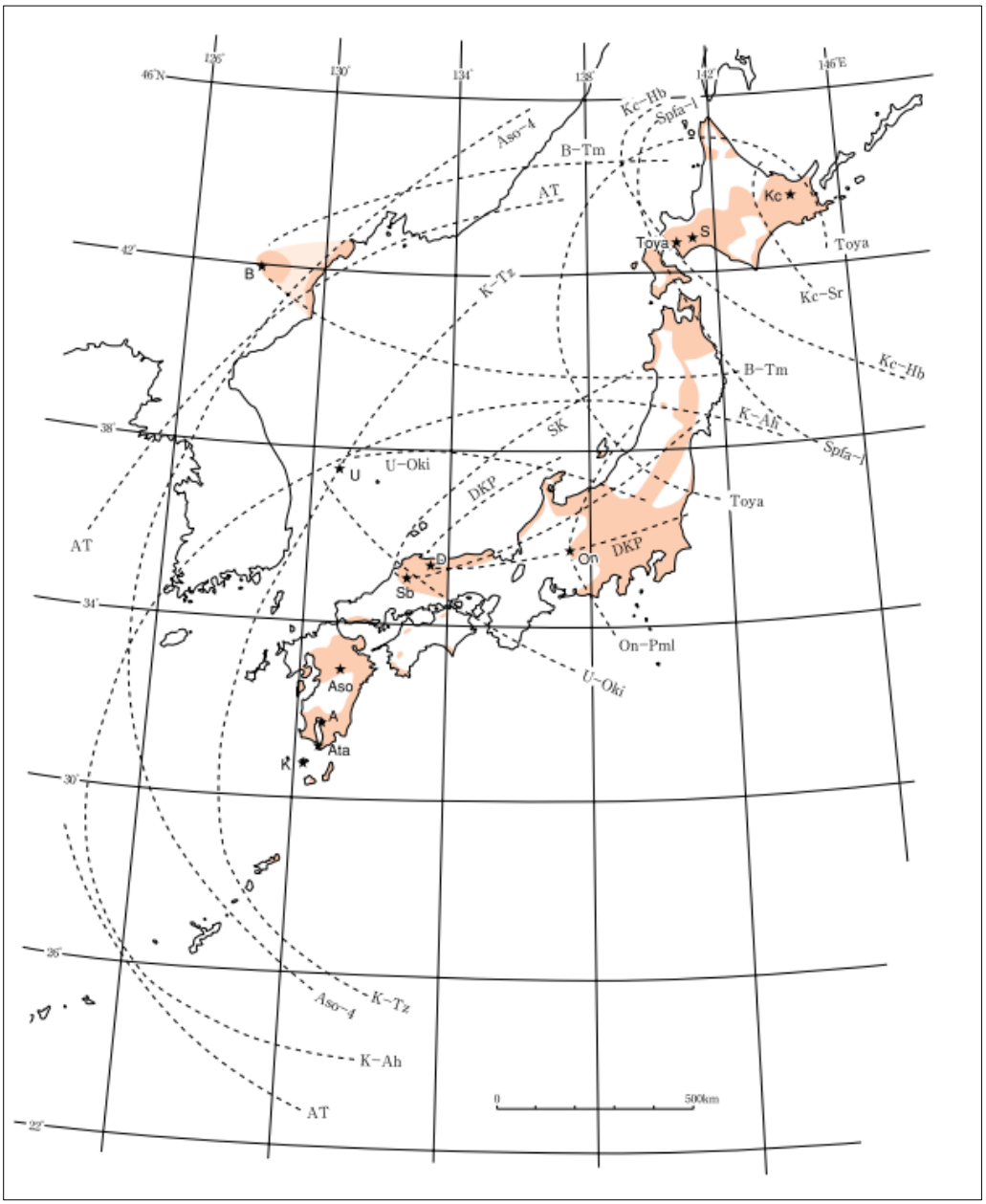

Fig.1.62 Distribution of Late Pleistocene major tephra marker layers of Japan and neighbouring areas (from Machida *et al.*, 1984). See Smith *et al.* (submitted) for more details.

Chapter 2 Aims and Methodology

2.1 Aims

The previous chapter has highlighted the issues affecting LA-ICP-MS analysis of tephra shards. These problems need to be investigated and overcome to allow for increased accuracy when correlating cryptotephra deposits.
In order to achieve this, the following research objectives are addressed:

i) To further test the hypothesis that element fractionation can be closely related to variations in crater size, element properties, glass composition, and laser excitation voltage.
ii) To compensate for any fractionation effects observed.
iii) To test fractionation factors by applying them to the trace element analyses of tephra from Ulleungdo, Korea, in order to assess whether proximal units can be distinguished.

A suite of tephra samples and MPI-DING and USGS reference glasses (Jochum *et al.*, 2005) of varying composition was analysed using a 193 nm GeoLas ArF Excimer laser coupled to a Thermo Element 2 magnetic sector ICP-MS at Aberystwyth University.

Element fractionation was tested through analysing samples at 20 µm, 10 µm, 6 µm and 4 µm crater diameters and laser fluences of 24.2 kV and 28 kV. Analyses were repeated over a series of days in order to assess variations in day to day instrument operating conditions. Graphical and statistical methods were used to assess the extent and nature of element fractionation, and fractionation factors were calculated to correct analyses for fractionation.

Fractionation factors were then applied to LA-ICP-MS analyses of a series of proximal Ulleungdo volcanic units. The trace element chemistry of a number of different Ulleungdo proximal units were compared in order to ascertain whether further correlations could be made with the SG06 core.

2.2 Methodology

2.2.1 Ulleungdo Sample Preparation

Proximal Ulleungdo samples were supplied by Dr Victoria Smith. The samples were collected from two sites (K1 and K7) on Ulleungdo, Korea (see Fig. 2.20). Details of the Ulleungdo samples and field correlations to geological units made by Dr Victoria Smith are seen in Table 2.20.

Samples were sieved in order to obtain size fractions of 90- 125 µm and 125- 250 µm. Glass shards were then retrieved from each size fraction of each sample using the density separation method established by Blockley *et al.* (2005). Procedures for sieving and density separation are given in Figs. 2.21 and 2.22.

The dried 250-125 µm light fraction of a <2.5 g/ml of each sample was then mounted in epoxy resin stubs containing 7 predrilled holes. Firstly, the resin stubs were affixed to a glass slide using silica gel. Each sample was then placed into separate holes in the resin stub using a pipette, the pipette was changed between each sample to avoid cross contamination. The location of the samples in each mount was recorded.

An epoxy resin was made up using Specifix® 40 and hardener to a mass ratio of 2.5 to 1. The resin was stirred for ~2 minutes and placed in an ultrasonic bath until all the gas bubbles had been removed. This mixture was then dropped onto the samples within the predrilled mount and stirred in order to remove any further bubbles. The glass slide and mount were then carefully placed in an oven at 60^{o}C for approximately 4 hours and left to cool overnight.

The mount was then removed from the glass slide using a razor blade. In order to achieve a flat surface and remove silica gel, each mount was ground by hand on 300 grade paper in a figure of eight motion for ~2 minutes. This was followed by grinding on 600 grade and then 1250 grade paper for up to 5 minutes, respectively. The mounts were checked under the microscope for scratches and then placed in an ultrasonic bath for ~2 minutes. They were then polished using a polishing machine, using 3 µm grade pads for 30 minutes and then using 1 µm grade pads for 5 minutes.

To aid locating the samples during subsequent trace element analysis, the sample mounts were etched with a razor blade and the x and y coordinates of three points on the mount were recorded. Resin mounts were then carbon coated, forming a conducting surface for analysis by electron microprobe.

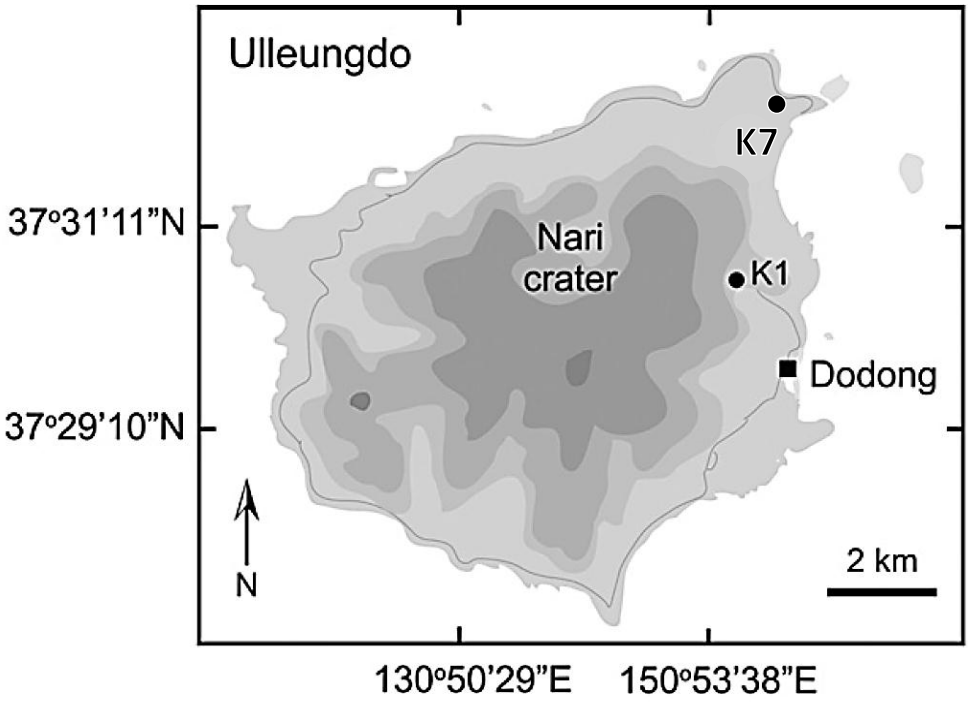

Fig. 2.20 Location of sample collection sites on Ulleungdo, Korea, from Smith *et al.* (2011).

Site	Sample	Unit	Description
K1	a1	U4	Pumice
	b1	U3?	Ignimbrite
	c1	U2?	Fall unit
K7	j1	U3	Ash & pumice unit
	f1	U5?	Pumice from basal PDC
	g1	U6?	Pumice
	i1	U7?	Pumice - weathered
	b2	?	Vitric ash

Table 2.20 Details of Ulleungdo proximal deposits with descriptions and field correlations to geological units (information provided by Dr Victoria Smith).

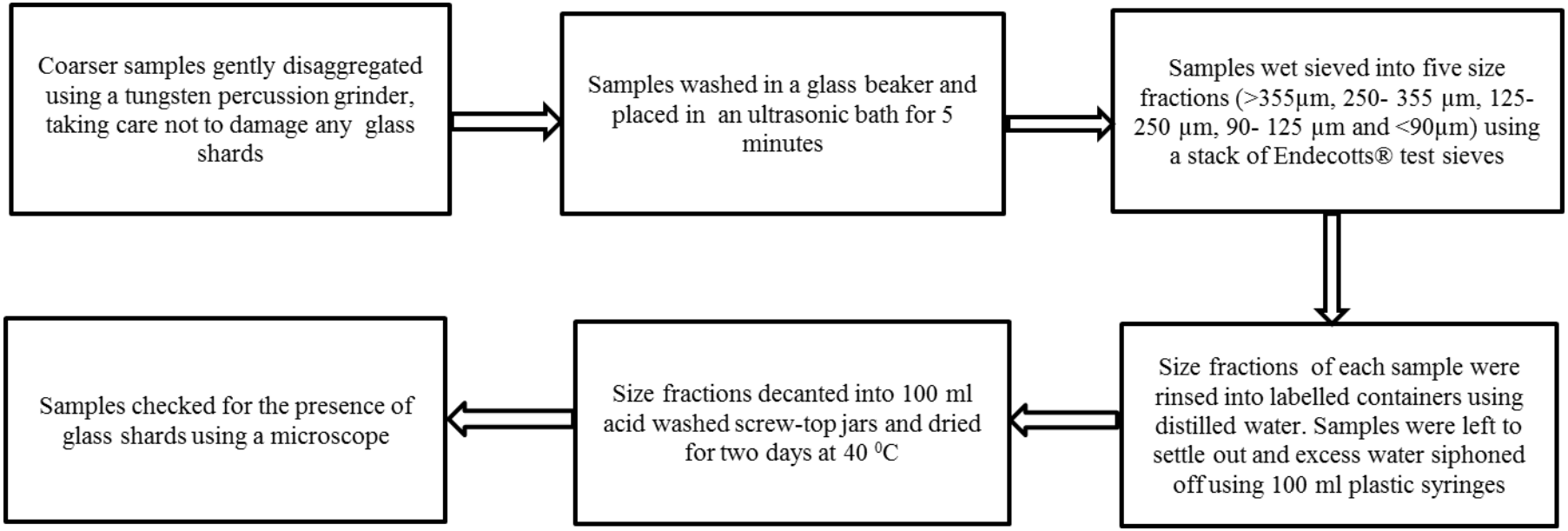

Fig. 2.21 Sample sieving procedure

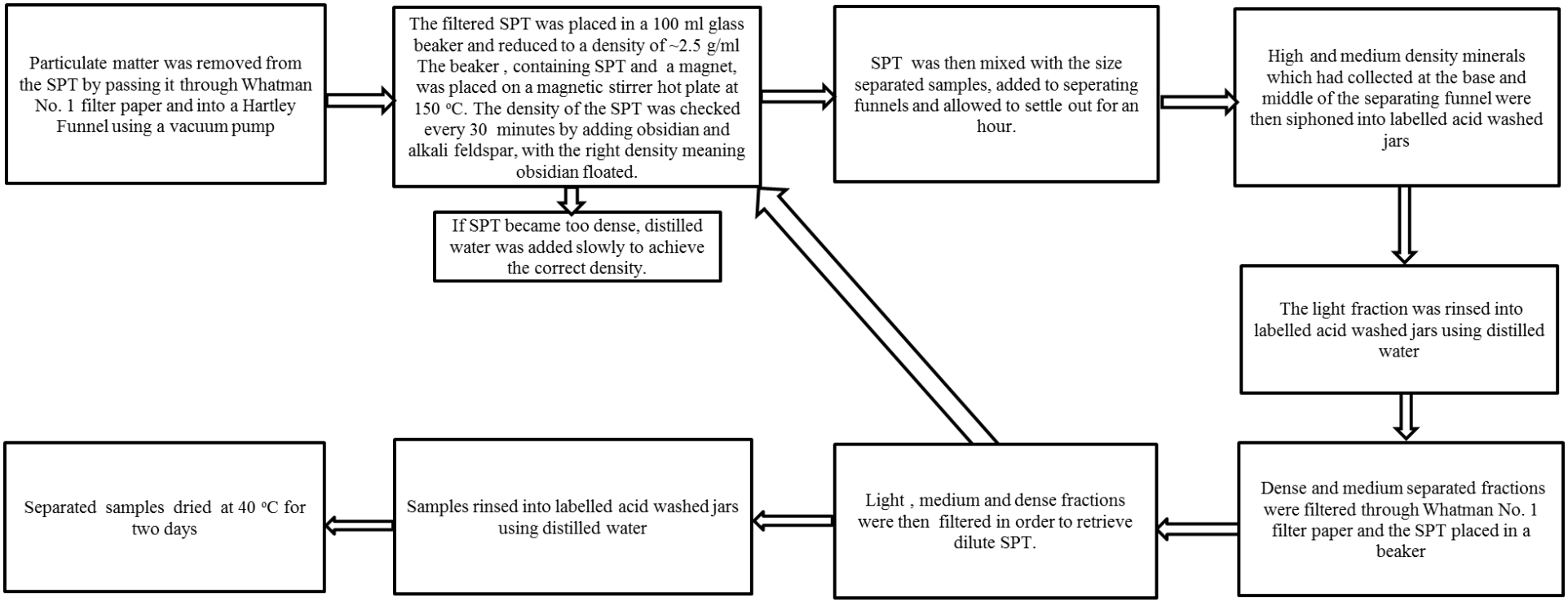

Fig. 2.22 Density separation procedure

2.2.2 Geochemical Analysis

EPMA Analysis

The tephra samples were then analysed for major elements using the Jeol 8600 electron microprobe, equipped with 4 wavelength dispersive spectrometers and 1 energy dispersive spectrometer, at RLAHA, Oxford. Typically 30 glass shards per sample were analysed using a 6 nA, 15 kV, 10 µm beam. When calibrating a 15 nA beam current was used and typical count times were 30 s on peak and 30 s on background (15 s either side), for each element. Low abundance elements were collected over a longer acquisition time; Cl and P were acquired over respectively a 50 and 60 s period. Na was only collected for the first 10 s (on peak) of analysis to reduce alkali element migration.

The analyses were calibrated against mineral standards and the calibration verified by MPI-DING reference glasses (Jochum *et al.,* 2005). Average secondary standards acquisitions for each day are given in Table 2.21. The secondary standards, ATHO-G, St-Hs6/80g and GOR 132G, were each analysed ten times during an analytical session. Typically, major element concentrations in secondary standards were measured to within 2 standard deviations from the reported concentration. Analytical errors for the EPMA results are typically ~<5% RSD for many elements, 0.4% for SiO_2 and ~0.6% for Al_2O_3. Higher RSD% for lighter elements was noted, e.g. ~30% for MnO, ~7% for TiO_2 and ~40% for P_2O_5. The majority of analytical totals were >95% and the glass shard analyses were normalised to 100% to compensate for secondary hydration of glasses and magmatic water content (Shane and Smith, 2000).

		SiO2	TiO2	Al2O3	FeO(t)	MnO	MgO	CaO	Na2O	K2O	P2O5	Cl
StHs6/80-G	**Preferred concs.**	**63.70**	**0.70**	**17.80**	**4.37**	**0.08**	**1.97**	**5.28**	**4.44**	**1.29**	**0.16**	**0.02**
Dacite	AVG	63.46	0.69	18.04	4.45	0.07	1.94	5.27	4.72	1.29	0.16	0.01
	AVG	63.42	0.73	17.90	4.35	0.06	1.98	5.35	4.73	1.31	0.16	0.01
	AVG	63.80	0.73	17.91	4.35	0.09	1.95	5.26	4.52	1.30	0.19	0.00
	SD	*0.18*	*0.02*	*0.10*	*0.05*	*0.01*	*0.02*	*0.04*	*0.14*	*0.01*	*0.01*	*0.01*
GOR132-G	**Preferred concs.**	**45.50**	**0.31**	**11.00**	**10.10**	**0.15**	**22.40**	**8.45**	**0.83**	**0.03**	**0.04**	**0.00**
Basalt	AVG	45.82	0.32	11.14	10.28	0.17	21.96	8.42	0.90	0.03	0.04	0.01
	AVG	45.75	0.30	11.07	10.24	0.14	22.21	8.49	0.79	0.03	0.04	0.00
	AVG	45.58	0.30	11.07	10.33	0.19	22.23	8.42	0.82	0.03	0.04	0.00
	SD	*0.15*	*0.01*	*0.06*	*0.10*	*0.02*	*0.18*	*0.03*	*0.05*	*0.00*	*0.00*	*0.00*
ATHO-G	**Preferred concs.**	**75.60**	**0.26**	**12.20**	**3.27**	**0.11**	**0.10**	**1.70**	**3.75**	**2.64**	**0.03**	**0.04**
Rhyolite	AVG	75.33	0.26	12.34	3.28	0.13	0.10	1.74	4.13	2.71	0.02	0.03
	AVG	75.47	0.25	12.38	3.31	0.10	0.09	1.70	4.11	2.74	0.03	0.04
	SD	*0.14*	*0.01*	*0.10*	*0.02*	*0.02*	*0.01*	*0.02*	*0.21*	*0.05*	*0.01*	*0.01*
Average RSD%		0.36	14.75	0.59	8.61	1.53	4.81	95.95	3.98	36.53	33.10	2.30

Table 2.21 Average analyses of MPI-DING reference materials analysed as secondary standards over a three day period, with reported concentrations (from Jochum *et al.,* 2005) for comparison. Values are in wt% with one standard deviation in italics.

LA-ICP-MS Analysis

Trace element analyses were undertaken using a Coherent GeoLas ArF 193 nm Excimer laser ablation system coupled to a Thermo Finnigan Element 2 magnetic sector ICP-MS at Aberystwyth University. Typical laser and ICP-MS operating conditions can be seen in Table 2.22.

LA-ICP-MS Instrumental Operating Conditions	
Thermo Element 2	
Cool gas	15.7 $Lmin^{-1}$
Auxiliary gas	1.05-1.20 $Lmin^{-1}$
Sample gas	~1.25 $Lmin^{-1}$
RF power	1050 W (morning) – 1150 W (afternoon) guard electrode off
U^{O+}/U^{+}, Th^{O+}/Th^{+}	Typically tuned to respectively <0.5% and <1%
Analytes	^{29}Si, ^{43}Ca, ^{44}Ca, ^{85}Rb, ^{88}Sr, ^{89}Y, ^{90}Zr, ^{93}Nb, ^{133}Cs, ^{137}Ba, ^{139}La, ^{140}Ce, ^{141}Pr, ^{143}Nd, ^{147}Sm, ^{151}Eu, 158Gd, ^{159}Tb, ^{163}Dy, ^{165}Ho, ^{166}Er, ^{169}Tm, ^{174}Yb, ^{175}Lu, ^{178}Hf, ^{181}Ta, ^{232}Th, ^{238}U
Runs/passes	1/10
Samples per peak	100
Mass window	5%
Segment duration	0.05 s
Acquisition time	20 s
GeoLas	
Excitation voltage	24.2 – 28 kV
Laser Fluence	10 Jcm^{-2}
Repetition rate	5 Hz
Pulse length	13-20 ns
Mask thickness	0.3 mm (>10 µm craters), 0.1 mm (6 µm and 4 µm craters)

Table 2.22 Typical operating condition of Thermo Element ICP-MS coupled to a GeoLas 193 nm laser

To investigate element fractionation, samples detailed in Tables 2.23 and 2.24 were each analysed five times at crater diameters of 20 µm, 10 µm 6 µm and 4 µm and excitation voltages of 24.2 kV and 28 kV. During a typical analytical run, a series of instrument blanks were acquired, followed by a series of calibration spectra (NIST 612) acquired using 20 µm and 10 µm crater diameters. Unknown sample spectra were then acquired, with intervening instrument blanks. Typically, three to four samples were analysed during each ~4 hr analytical run. At the end of each analytical run a series of instrument blanks were acquired, followed by ten calibration spectra obtained using 20 µm and 10 µm crater diameters. Through obtaining calibration spectra at the start and end of each analytical run instrumental drift can be accounted for (Pearce *et al.,* 2011). For all analyses ^{29}Si was used as an internal standard, using Si concentrations detailed in Tables 2.23 and 2.24.

Ulleungdo samples were then analysed by LA-ICP-MS. Relocation of glass shards analysed by EPMA was achieved by inputting the *x*-*y* coordinates of three reference points on each mount and those of the shard to be analysed into a coordinate transformation spread sheet (provided in the supplementary material from Kuehn and Froese, 2010). Each shard was analysed at 10 Jcm^{-2} and 5 Hz (at crater diameters of typically < 10 µm). Analyses were then calibrated against NIST 612 acquisitions at 20 µm crater diameters and shard specific ^{29}Si concentrations obtained by EPMA analysis were used as internal standards. During an analytical run, five analyses of a reference material at a crater diameter of 20 µm were acquired, allowing the precision of the instrument to be assessed.

Data in the form of counts per second (cps) were converted to concentration (ppm) using an Excel spreadsheet with in-built calculations prepared by Prof. N. Pearce. The spreadsheet first subtracts gas blank counts from sample counts. Gas blank subtracted analyte cps are then divided by the internal standard cps and multiplied by the internal standard concentration. Ratios are then drift corrected, the drift is calculated by dividing the average NIST 612 20 µm crater diameter acquisitions from the end of the analytical run by those acquired at the start. To calibrate, the drift corrected ratios are then divided by the calibration slope. Calibration slopes are calculated by averaging the 20 µm and 10 µm crater diameter NIST 612 acquisitions and dividing each slope by preferred NIST 612 concentrations.

Analyses acquired at all crater diameters were then fractionation corrected by dividing element concentrations by the 20 µm crater diameter fractionation factor calculated by Pearce *et al.* (2011).

Any analyses which originated from mineral contamination, rather than glass, were then removed; these are typically identified by high Zr and Hf concentrations (indicating zircons), high Ba and Sr concentrations (feldspars), low overall counts (quartz) and high Rb and Cs concentrations (micas) (Pearce, *pers. comm*.)

2.2.3 Calculation of Compositional Parameters

In order to investigate element fractionation, a compositional suite of MPI-DING (Jochum *et al.,* 2005) and USGS reference materials and tephra samples were analysed, details of these samples are seen in Tables 2.20 and 2.21.

The polymerisation, viscosity and liquidus temperature of each sample were calculated in order to assess the impact of sample composition on element fractionation. Viscosity and liquidus temperature of each sample were calculated by entering the major element composition of each sample into KWare® geological software (Wohletz, 1999).

The polymerisation of each sample was calculated after Mysen (1981). The number of non-bridging oxygens to tetrahedrally organised oxygens (NBO/T) may be used to quantify polymerisation, providing an indication of melt structure. An NBO/T = ~0 corresponds to a highly polymerised melt (e.g. rhyolite) and a value of ~1 corresponds to a highly depolymerised melt (e.g. basalt). In this study NBO/T is calculated using the method of Deubener *et al.* (2003), with Na, K, Ca and Mg assumed to be network modifers (NBO) and Si and Al assumed to be network formers (T). Anhydrous major element concentrations of Na_2O, K_2O, CaO, MgO, Al_2O_3 and SiO_2 in each sample (Table 2.23 and 2.24) were recalculated as cation molecular proportions and entered into equation (1) from Deubener *et al.* (2003).

$$NBO/T = (Na + K + 2Ca + 2Mg - Al) / (Si + Al) \quad \textbf{(1)}$$

The polymerisation, liquidus temperature and viscosity of all samples are presented in Tables 2.23 and 2.24. Polymerisation is negatively correlated with SiO_2 concentration in Fig. 2.23. This is due to the general increase in network formers and decrease in network modifiers with increasing SiO_2wt%. NIST 610 and 612 are depolymerised relative to their high (~70wt%) SiO_2 concentration, due to high concentrations of the network modifier,

Na_2O (~13wt%) and low concentrations of the network former, Al_2O_3 (~2wt%). Viscosity is closely related to polymerisation, with both parameters governed by melt composition. Network formers create strong cation-anion bonds, with their increasing abundance, melts become more ordered and viscous (Cas and Wright, 1987).

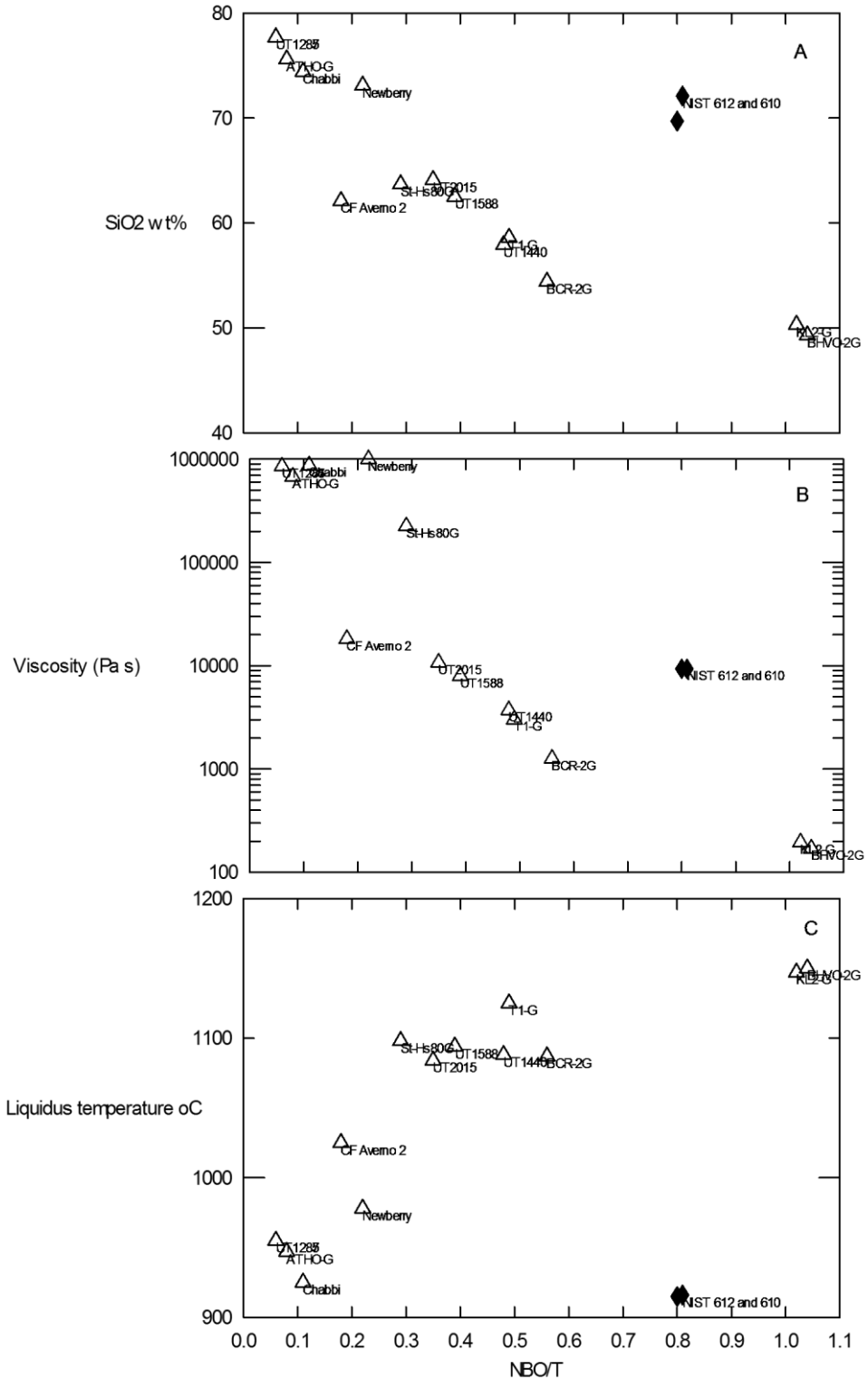

Fig. 2.23 A) SiO_2wt% of samples vs. NBO/T B) Bottinga-Weill viscosity (Pa s) vs. NBO/T C) Liquidus temperature (^oC) vs. NBO/T.

Sample	NBO/T	Viscosity Pa-s	Liquidus Temperature ^{o}C	SiO2	TiO2	Al2O3	FeO(t)	Na2O	MnO	MgO	CaO	K2O	P2O5
T1-G	0.49	2990	1125	**58.60**	**0.76**	**17.10**	**6.44**	**3.13**	**0.13**	**3.75**	**7.10**	**1.96**	**0.17**
Andesite				*0.40*	*0.02*	*0.20*	*0.06*	*0.09*	*0.01*	*0.04*	*0.09*	*0.04*	*0.03*
StHs6/80-G	0.29	222000	1098	**63.70**	**0.70**	**17.80**	**4.37**	**4.44**	**0.08**	**1.97**	**5.28**	**1.29**	**0.16**
Dacite				*0.50*	*0.02*	*0.20*	*0.07*	*0.14*	*0.00*	*0.04*	*0.09*	*0.02*	*0.02*
KL2-G	1.02	194	1147	**50.30**	**2.56**	**13.30**	**10.70**	**2.35**	**0.17**	**7.34**	**10.90**	**0.48**	**0.23**
Basalt				*0.30*	*0.09*	*0.20*	*0.10*	*0.08*	*0.01*	*0.09*	*0.20*	*0.01*	*0.03*
GOR132-G	1.51	141	1187	**45.50**	**0.31**	**11.00**	**10.10**	**0.83**	**0.15**	**22.40**	**8.45**	**0.03**	**0.04**
Basalt				*0.40*	*0.01*	*0.20*	*0.10*	*0.04*	*0.01*	*0.20*	*0.12*	*0.00*	*0.01*
ATHO-G	0.08	679000	947	**75.60**	**0.26**	**12.20**	**3.27**	**3.75**	**0.11**	**0.10**	**1.70**	**2.64**	**0.03**
Rhyolite				*0.70*	*0.02*	*0.20*	*0.10*	*0.31*	*0.01*	*0.01*	*0.03*	*0.09*	*0.00*
BCR-2G	0.56	1270	1087	**54.4**	**2.27**	**13.4**	**12.4**	**3.23**	**0.19**	**3.56**	**7.06**	**1.74**	**0.37**
Basalt				*54.4*	*0.04*	*0.4*	*0.3*	*0.07*	*0.01*	*0.09*	*0.11*	*0.04*	*0.01*
BHVO-2G	1.04	170	1150	**49.3**	**2.79**	**13.6**	**11.3**	**2.4**	**0.17**	**7.13**	**11.4**	**0.51**	**0.29**
Basalt				*0.1*	*0.02*	*0.1*	*0.1*	*0.1*	*0.03*	*0.02*	*0.1*	*0.02*	*0.02*
NIST 610	0.80	9340	983	**69.98**	**0.08**	**2.04**	**0.06**	**13.35**	**0.05**	**0.07**	**11.45**	**0.06**	**0.12**
Soda-lime silicate				*0.39*	*0.01*	*0.16*	*0.02*	*0.68*	*0.01*	*0.01*	*0.23*	*0.00*	*0.00*
NIST 612	0.81	9430	916	**71.90**	**0.01**	**2.11**	**0.02**	**13.98**	**0.01**	**0.00**	**11.93**	**0.01**	**0.01**
Soda-lime silicate				*0.96*	*0.00*	*0.16*	*0.00*	*0.56*	*0.00*	-	*0.22*	*0.00*	-

Table 2.23 Anhydrous major element chemistry of USGS and BCR-2G reference materials, preferred concentrations are from GeoReM, except for NIST 610 and NIST 612 where values are from Pearce *et al.* (1997). All values are in wt% with one standard deviation in italics. NBO/T was calculated after Mysen (1981) whilst viscosity and liquidus temperatures of samples were calculated by inputting major element concentrations in each sample into KWare® Geological Software (Wohletz, 1999).

Sample	NBO/T	Viscosity Pa-s	Liquidus Temperature °C	SiO_2	TiO_2	Al_2O_3	FeO(t)	MnO	MgO	CaO	Na_2O	K_2O	P_2O_5	Values from	Collected by
Chabbi Obsidian	0.11	862000	925	**74.32**	**0.28**	**9.48**	**2.91**	**0.22**	**0.17**	**0.23**	**5.46**	**4.39**		MacDonald and Gibson (1969)	Nick Pearce
Alkali Rhyolite				*0.32*	*0.03*	*0.10*	*0.16*	*0.01*	*0.03*	*0.04*	*0.13*	*0.07*			
Newberry Obsidian	0.22	998000	978	**73.07**	**0.21**	**14.44**	**1.65**	**0.06**	**0.20**	**1.00**	**4.77**	**4.04**	**0.07**	Higgins (1973)	Nick Pearce
Alkali Rhyolite				*0.46*	*0.02*	*0.12*	*0.08*	*0.03*	*0.03*	*0.24*	*0.48*	*0.10*	*0.05*		
UT1285/ UT 1287	0.06	848000	955	**77.68**	**0.11**	**12.38**			**0.07**	**0.77**	**3.72**	**3.84**		Pearce *et al.* (2007)	Nick Pearce
Rhyolite				*0.20*	*0.02*	*0.07*			*0.03*	*0.05*	*0.17*	*0.14*			
UT1440	0.48	3740	1088	**57.99**	**1.54**	**15.98**	**8.82**	**0.23**	**2.69**	**6.59**	**4.29**	**1.75**		John Westgate	John Westgate
Trachyandesite				*0.70*	*0.23*	*0.58*	*0.50*	*0.06*	*0.47*	*0.73*	*0.17*	*0.33*			
UT2015	0.35	10700	1084	**64.07**	**0.68**	**16.33**	**5.01**	**0.09**	**2.45**	**5.11**	**4.19**	**2.02**		John Westgate	John Westgate
Rhyodacite				*7.06*	*0.29*	*1.95*	*2.00*	*0.05*	*1.29*	*2.29*	*0.33*	*0.92*			
UT1588	0.39	8030	1094	**62.49**	**1.02**	**16.72**	**5.44**	**0.09**	**2.60**	**5.66**	**4.25**	**1.66**		John Westgate	John Westgate
Quartz latite				*4.86*	*0.30*	*1.14*	*1.45*	*0.04*	*0.83*	*1.49*	*0.21*	*0.47*			
CF86	0.18	18200	1025	**62.10**	**0.42**	**18.25**	**2.85**	**0.23**	**0.23**	**1.81**	**6.48**	**6.69**	**0.04**	This study	Victoria Smith
				0.39	*0.03*	*0.15*	*0.13*	*0.06*	*0.02*	*0.07*	*0.34*	*0.10*	*0.02*		

Table 2.24 Anhydrous major element chemistry of tephra samples taken from several studies. All values are in wt% with one standard deviation in italics. NBO/T was calculated after Mysen (1981) whilst viscosity and liquidus temperatures of samples were calculated by inputting major element concentrations in each sample into KWare® Geological software (Wohletz, 1999).

Liquidus temperature generally increases with increasing polymerisation. This may be explained by the Bowen's Reaction Series, where minerals containing higher SiO_2 are stable at lower temperatures and therefore melt at lower temperatures (Bowen, 1956). The low melting temperature of the depolymerised NIST reference materials may be associated with its high SiO_2 concentration.

Chapter 3 LA-ICP-MS Analytical Considerations

3.1 Lower Limits of Quantification

The impact of crater diameter, analysis time and sample composition on lower limits of detection (LLD) and lower limits of quantification (LLQ) is investigated in this chapter. The LLD may be defined as the concentration at which an element is detected above instrument background noise and is expressed in equation (2) (from Perkins and Pearce, 1995).

LLD (ppm) = 3 x standard deviation of gas blanks (cps) x (concentration (ppm) /avg. sample cps) **(2)**

The LLQ is the concentration at which a particular element may be quantified above the background noise; it may be calculated as 3.333 *x* LLD (Perkins and Pearce, 1995).

LLQ and LLD concentrations for all sample acquisitions using 20 µm and 10 µm crater diameters were calculated using NIST 612 spectra and intervening gas blanks. LLD and LLQ concentrations for each sample at 6 µm and 4 µm crater diameters were then calculated using the cps for the particular sample and crater diameter and the intervening gas blanks. Lower limits of detection for Rb, Y, U, Pr, Hf and Cs are plotted against crater diameter in Fig. 3.11.

Pearce *et al.* (2011) state that limits of detection are sensitive to instrumental variations associated with tuning and instrument blanks. During an analytical session, the blank at ^{29}Si decreases steadily, associated with the warm-up of the ICP-MS (Fig. 3.10 A). The blank at ^{29}Si varies by ~5% every 5-10 minutes; possibly associated with a pulsing of the vacuum system (Pearce *et al.,* 2011). Background counts for Sr, Rb, Cs and Ba increase over time, the 'sticky' nature of the alkali elements causing them to adhere to glassware and interface cones within the ICP-MS (Fig. 3.10 B) (Pearce *et al.,* 2011; Jenner and O'Neill, 2012). Pearce *et al.* (2011) state that as part of instrument maintenance, interface cones may be cleaned in order to reduce gas blanks, however, the removal of the oxide film from the cones may cause the instrument to drift for several days.

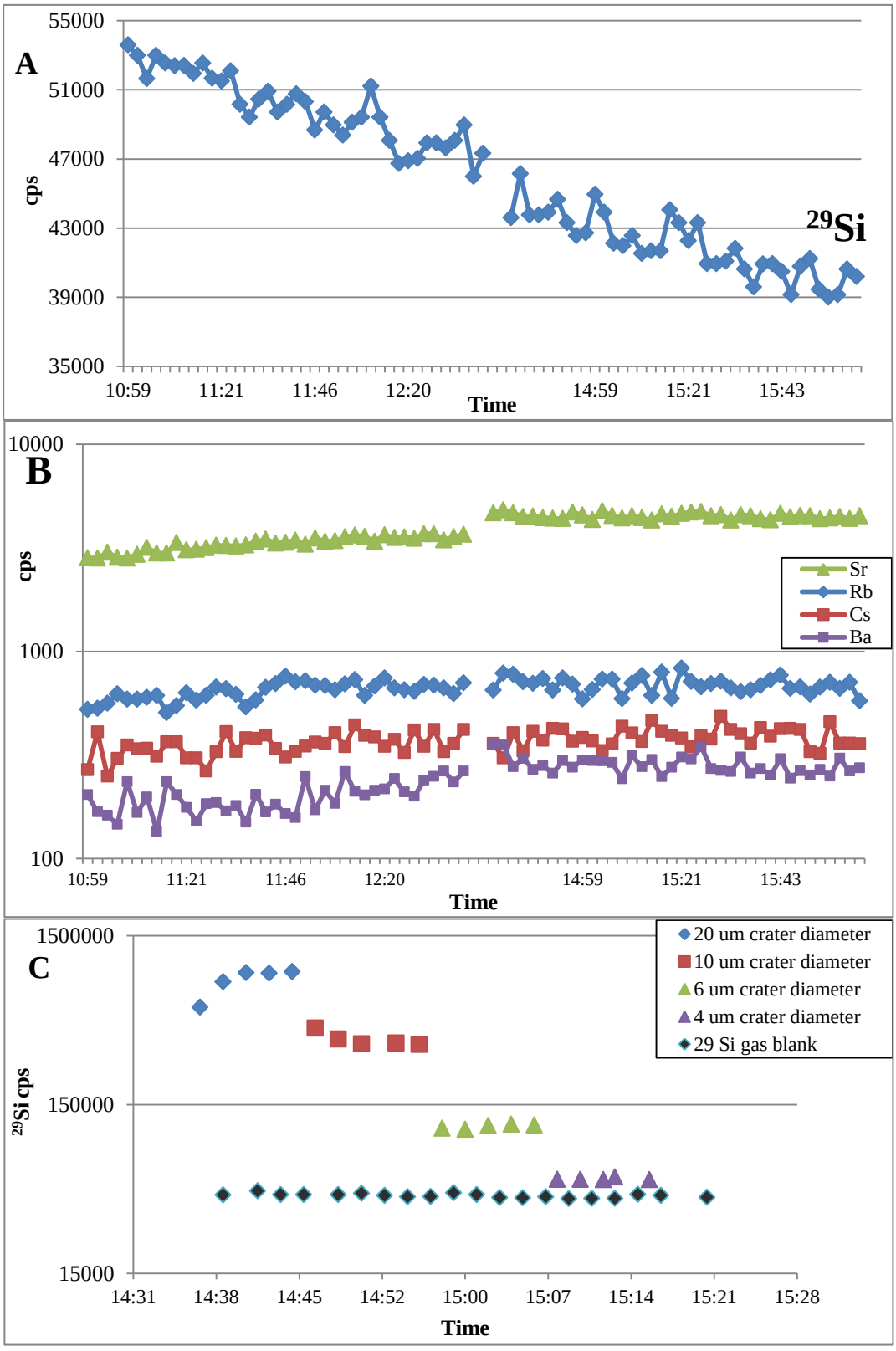

Fig. 3.10 Counts per second obtained from one day of analysis, A) instrumental blanks at mass 29 over a 5 hour acquisition period, with a break in the middle B) blanks for Sr, Rb, Cs and Ba over the same time period as A, C) ATHO-G cps acquired over a 30 minute period using a range of crater diameters with instrument blanks for ^{29}Si plotted alongside. Analyses were undertaken using only Ar as a carrier gas, with the excitation voltage at 24.2 kV, a repetition rate of 5 Hz and a laser fluence of 10 Jcm^{-2}. Note vertical log scales for B and C.

Figure 3.10 C shows a series of analyses of the rhyolitic reference material ATHO-G over 30 minutes using 20 µm, 10 µm, 6 µm and 4 µm crater diameters and plotted alongside intervening gas blank cps. With decreasing crater diameter the ^{29}Si signal to background ratio decreases; the ratio is ~20 when a 20 µm crater diameter is used, ~10 using a 10 µm crater diameter, ~3 using a 6 µm crater diameter and ~>1 using a 4 µm crater diameter. This relates to an increase in Rb, Y, Pr and Hf LLD concentrations with decreasing crater diameter (Fig. 3.11). At all crater diameters, LLD for U are low and Rb and Cs LLD are high, associated with low blanks for U and high blanks for Rb and Cs. Trace elements above LLD and/or LLQ concentrations in a variety of compositions and crater diameters are reported in Tables 3.10 and 3.11, trace element concentrations in each sample are given in Table 3.12.

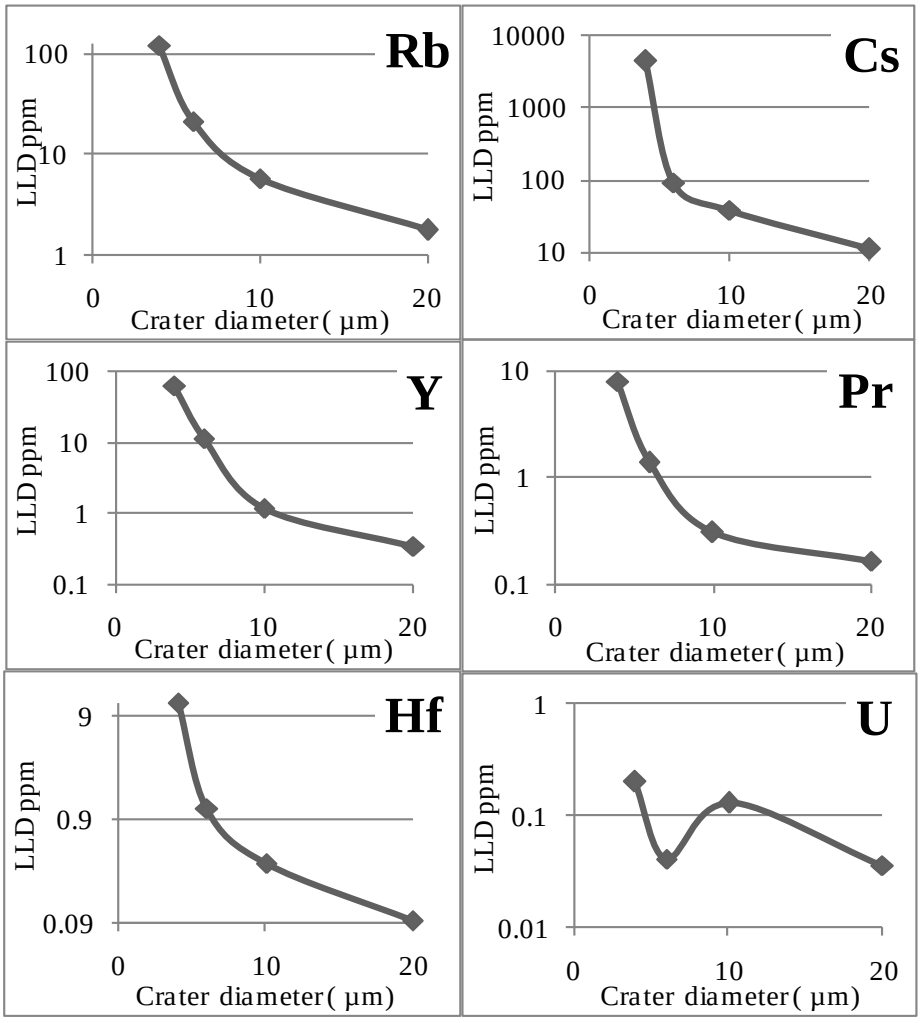

Fig. 3.11 Graphs show change in LLD for the rhyolitic reference glass material, ATHO-G, using crater diameters of 20 µm, 10 µm, 6 µm and 4 µm. Note vertical log scales.

An increasing number of trace elements fall below the LLD and LLQ with decreasing crater diameter. At 20 µm and 10 µm crater diameters, the majority of trace elements are present above the LLQ. However, Cs and occasionally Sr concentrations fall below the LLQ and LLD due to high gas blanks for these elements. Using 6 µm crater diameters, many MREE and HREE concentrations drop below the LLD and/or LLQ and using 4 µm crater diameters fewer M-HREE are detectable. However, at <10 µm crater diameters Rb, Y, Zr, Nb, Ba, La, Pr, Ce, Th and U remain above the LLD and/or LLQ. At all crater diameters, the light rare earth elements (LREE) and Rb, Sr, Zr, Nb, Cs and Ba concentrations all fall below LLD and LLQ in GOR 132G, a result of their low abundance (nominal <~2ppm) in this sample. Pearce *et al.* (2011) also noted Y, Zr, Ba, La, Ce, Th and Ce remained quantifiable and Rb, Sr, Nb, Pr and Nd remained detectable in Minoan glass shards using 4 µm crater diameters. Improving the signal for the petrogenically significant HFSE and LREE at 6 µm and 4 µm crater diameters may be achieved by counting only for these detectable elements, thereby increasing counting times on each element peak.

Tables 3.10 and 3.11 demonstrate the control of composition on detection and quantification limits. The calculated LLD and LLQ concentrations presented here indicate that neither ^{43}Ca nor ^{44}Ca are quantifiable in acidic (rhyolitic) glasses when using <20 µm crater diameters. The LLQ for ^{43}Ca in ATHO-G (rhyolite containing ~1.7wt% CaO) increases from ~4wt% at 20 µm crater diameter to ~18wt% at 10 µm to ~71wt% at 6 µm and to ~1600wt% at 4 µm. Low concentrations (<~1wt%) of CaO in rhyolites, mean that ^{43}Ca and ^{44}Ca are only suitable internal standards for basic tephra glass shard analyses at >10 µm crater diameters. ^{29}Si is a more suitable internal standard for rhyolitic analyses at <10 µm diameters; the LLQ for ^{29}Si in ATHO-G is ~5wt% at a 20 µm crater diameter, ~ 18wt% at 10 µm, ~ 31wt% at 6 µm and 178wt% at 4 µm, with Si concentrations at 4 µm detectable. ^{29}Si remains quantifiable in all but two samples using 6 µm crater diameters and is detectable in 10 of the 15 samples using 4 µm crater diameters. This is the result of the lower signal/background ratio at mass 29 than for ^{43}Ca and ^{44}Ca. Pearce *et al.* (2011) also suggested that CaO may only be used as an internal standard for basaltic analyses at large crater diameters.

Therefore, this study will focus only on the fractionation of the petrogenically significant trace elements and ^{29}Si will be used as an internal standard. Due to the low trace element abundance in GOR 132G, the fractionation of this reference material will not be investigated.

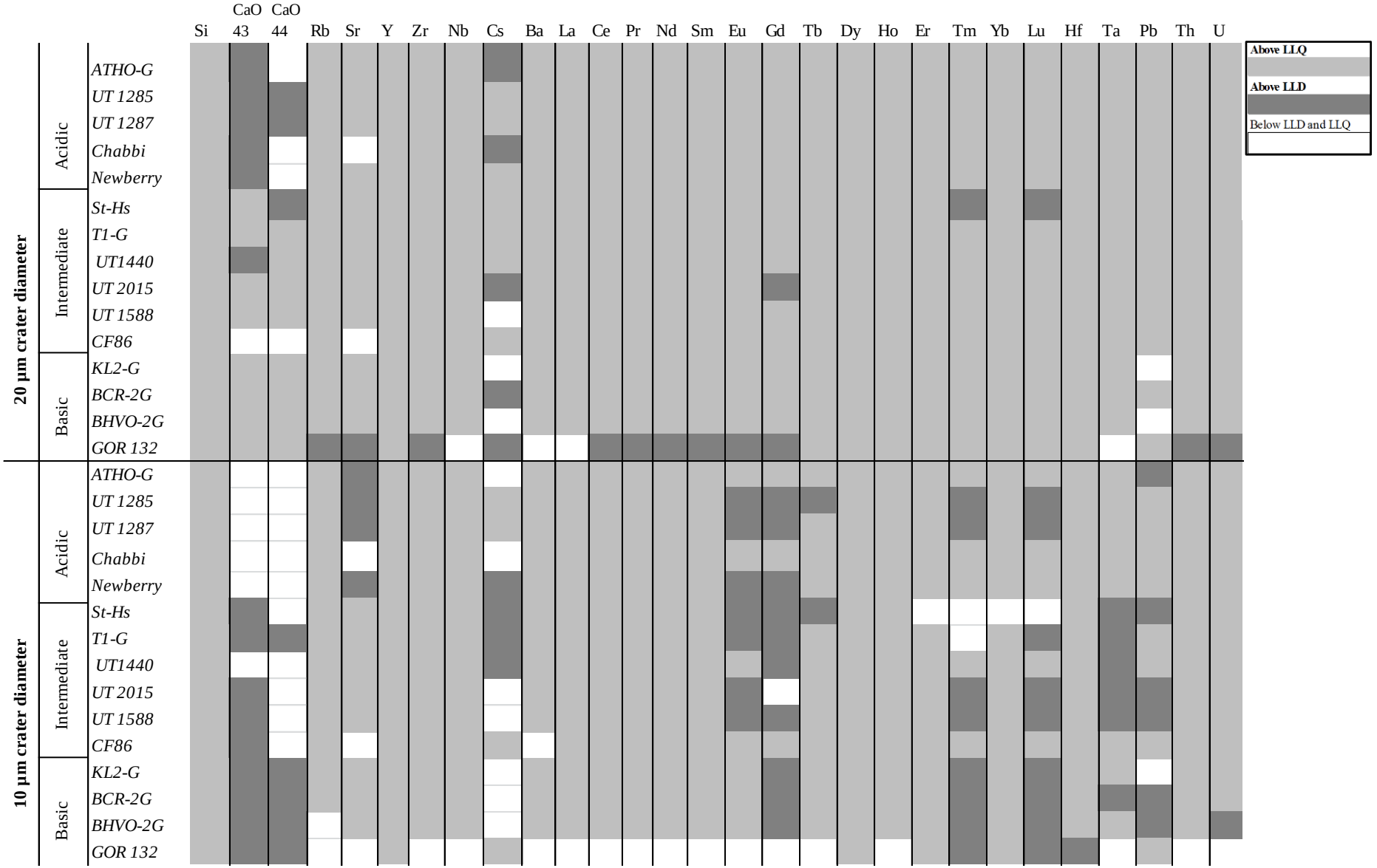

Table 3.10. Trace elements detectable and quantifiable in basic, intermediate and acidic glass compositions at 20 µm and 10 µm crater diameters. Elements with no shading are below the LLD, elements with dark grey and light grey shading are above LLD and LLQ, respectively.

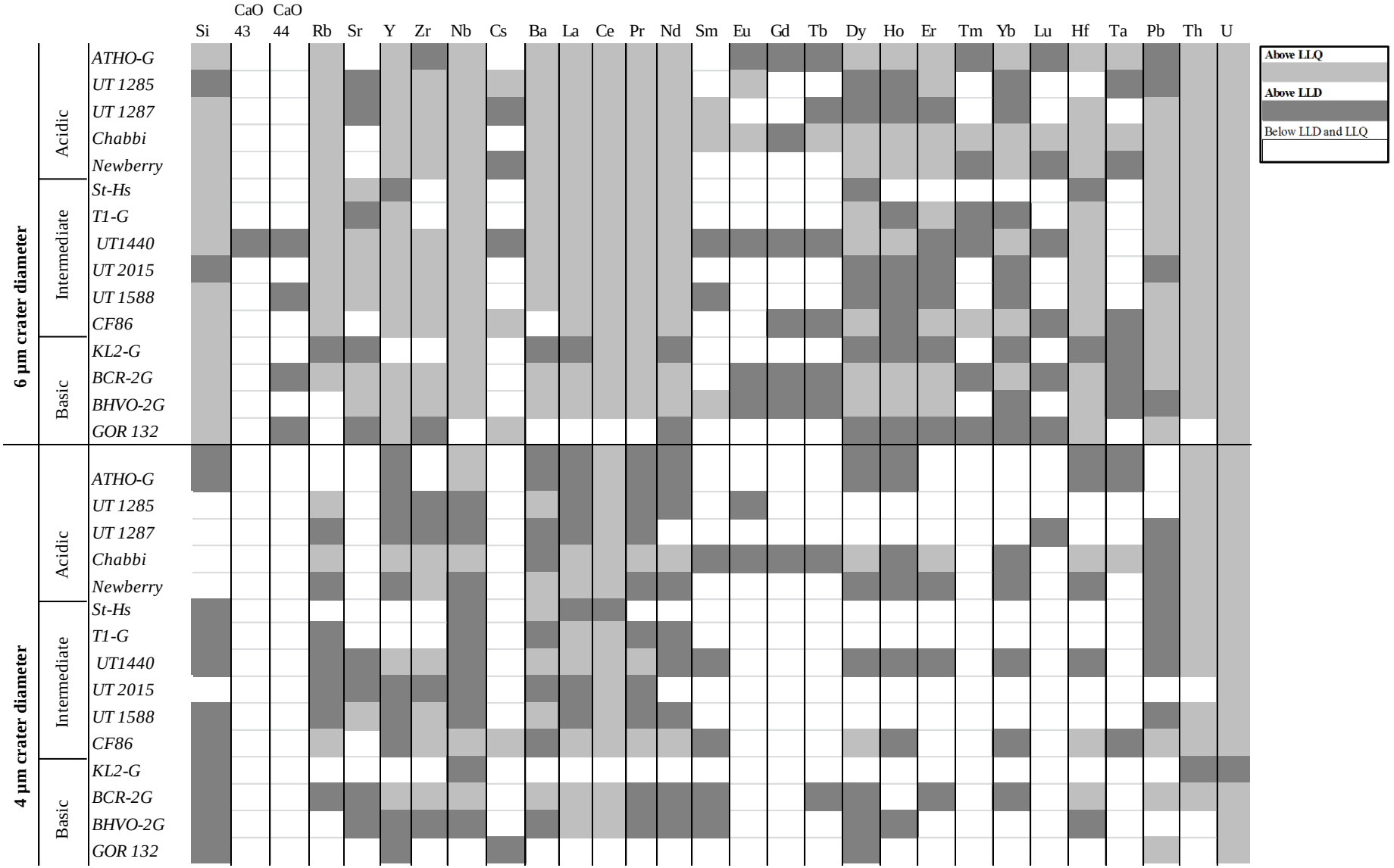

Table 3.11. Trace elements detectable and quantifiable in basic, intermediate and acidic glass compositions at 6 µm and 4 µm crater diameters. Elements with no shading are below the LLD, elements with dark grey and light grey shading are above LLD and LLQ, respectively.

Sample	*ATHO-G*	*SD*	*St-Hs680G*	*SD*	*T1-G*	*SD*	*KL2-G*	*SD*	*BCR-2G*	*SD*	*BHVO-2G*	*SD*	*GOR 132G*	*SD*
SiO_2	**75.6**	*0.70*	**63.7**	*0.50*	**58.6**	*0.40*	**50.3**	*0.40*	**54.4**	*0.40*	**49.3**	*0.40*	**45.5**	*0.40*
CaO	**1.70**	*0.03*	**5.28**	*0.09*	**7.10**	*0.09*	**10.9**	*0.20*	**7.06**	*0.11*	**11.4**	*0.11*	**8.45**	*0.12*
Rb	**65.3**	*3.00*	**30.7**	*1.70*	**79.7**	*3.50*	**8.70**	*0.40*	**47.0**	*0.50*	**9.20**	*0.50*	**2.10**	*0.10*
Sr	**94.1**	*2.70*	**482**	*8.00*	**284**	*6.00*	**356**	*8.00*	**342**	*4.00*	**396**	*4.00*	**15.3**	*0.60*
Y	**94.5**	*3.50*	**11.4**	*0.40*	**23.9**	*0.80*	**25.4**	*1.10*	**35.0**	*3.00*	**26.0**	*3.00*	**12.9**	*0.50*
Zr	**512**	*20.00*	**118**	*3.00*	**144**	*4.00*	**152**	*5.00*	**184**	*15.00*	**170**	*15.00*	**9.90**	*0.30*
Nb	**62.4**	*2.60*	**6.94**	*0.25*	**8.87**	*0.43*	**15.0**	*0.50*	**12.5**	*1.00*	**18.3**	*1.00*	**0.073**	*0.01*
Cs	**1.08**	*0.11*	**1.75**	*0.11*	**2.69**	*0.19*	**0.115**	*0.01*	**1.16**	*0.07*	**0.100**	*0.07*	**7.45**	*0.63*
Ba	**547**	*16.00*	**298**	*9.00*	**388**	*12.00*	**123**	*5.00*	**683**	*7.00*	**131**	*7.00*	**0.815**	*0.06*
La	**55.6**	*1.50*	**12.0**	*0.30*	**70.4**	*2.40*	**13.1**	*0.20*	**24.7**	*0.30*	**15.2**	*0.30*	**0.0842**	*0.00*
Ce	**121**	*4.00*	**26.1**	*0.70*	**127**	*4.00*	**32.4**	*0.70*	**53.3**	*0.50*	**37.6**	*0.50*	**0.393**	*0.02*
Pr	**14.6**	*0.40*	**3.20**	*0.06*	**12.4**	*0.40*	**430**	*0.10*	**6.70**	*0.40*	**5.35**	*0.40*	**0.0890**	*0.00*
Nd	**60.9**	*2.00*	**13.0**	*0.30*	**41.4**	*1.20*	**21.6**	*0.40*	**28.9**	*0.30*	**24.5**	*0.30*	**0.689**	*0.02*
Sm	**14.2**	*0.40*	**2.78**	*0.05*	**6.57**	*0.14*	**5.54**	*0.09*	**6.59**	*0.07*	**6.10**	*0.07*	**0.508**	*0.02*
Eu	**2.76**	*0.10*	**0.953**	*0.02*	**1.21**	*0.04*	**1.92**	*0.04*	**1.97**	*0.02*	**2.07**	*0.02*	**0.255**	*0.01*
Gd	**15.3**	*0.70*	**2.59**	*0.09*	**5.31**	*0.29*	**5.92**	*0.20*	**6.71**	*0.07*	**6.16**	*0.07*	**1.19**	*0.04*
Tb	**2.51**	*0.08*	**0.371**	*0.01*	**0.773**	*0.03*	**0.89**	*0.03*	**1.02**	*0.08*	**0.920**	*0.08*	**0.269**	*0.01*
Dy	**16.2**	*0.70*	**2.22**	*0.06*	**4.50**	*0.12*	**5.22**	*0.12*	**6.44**	*0.06*	**5.28**	*0.06*	**2.15**	*0.06*
Ho	**3.43**	*0.11*	**0.420**	*0.01*	**0.86**	*0.03*	**0.961**	*0.02*	**1.27**	*0.08*	**0.980**	*0.08*	**0.507**	*0.02*
Er	**10.3**	*0.50*	**1.18**	*0.04*	**2.49**	*0.08*	**2.54**	*0.07*	**3.70**	*0.04*	**2.56**	*0.04*	**1.56**	*0.05*
Tm	**1.52**	*0.07*	**0.172**	*0.01*	**0.354**	*0.02*	**0.331**	*0.01*	**0.51**	*0.04*	**0.340**	*0.04*	**0.234**	*0.01*
Yb	**10.5**	*0.40*	**1.13**	*0.03*	**2.38**	*0.08*	**2.10**	*0.05*	**3.39**	*0.03*	**2.01**	*0.03*	**1.61**	*0.04*
Lu	**1.54**	*0.05*	**0.168**	*0.01*	**0.354**	*0.01*	**0.285**	*0.01*	**0.503**	*0.01*	**0.279**	*0.01*	**0.237**	*0.01*
Hf	**13.7**	*0.50*	**3.07**	*0.09*	**3.88**	*0.15*	**3.93**	*0.14*	**4.84**	*0.28*	**4.32**	*0.28*	**0.357**	*0.02*
Ta	**3.90**	*0.20*	**0.420**	*0.02*	**0.464**	*0.02*	**0.961**	*0.02*	**0.78**	*0.06*	**1.15**	*0.06*	**0.031**	*0.00*
Pb	**5.67**	*0.62*	**10.3**	*0.90*	**11.6**	*1.50*	**2.07**	*0.10*	**11.0**	*1.00*	**1.70**	*1.00*	**19.5**	*1.70*
Th	**7.40**	*0.27*	**2.28**	*0.07*	**31.3**	*1.00*	**1.02**	*0.03*	**5.90**	*0.30*	**1.22**	*0.30*	**0.00900**	*0.00*
U	**2.37**	*0.12*	**1.01**	*0.04*	**1.71**	*0.10*	**0.548**	*0.02*	**1.69**	*0.12*	**0.403**	*0.12*	**0.0480**	*0.01*

Table 3.12 Trace element concentrations in MPI-DING and USGS reference materials (ppm) and SiO_2wt% and CaOwt% to 3 sig. figs. Element concentrations are from GeoReM; standard deviations are given to 2 decimal places and illustrated in italics.

	UT1285 *n=20*	*SD*	*UT1287* *n=20*	*SD*	*Chabbi Obsidian* *n=10*	*SD*	*Newberry Obsidian* *n=18*	*SD*	*UT1440* *n=10*	*SD*	*UT2015* *n=18*	*SD*	*UT1588* *n=18*	*SD*	*Campi Flegrei* *n=5*	*SD*
SiO_2	**77.7**	*0.19*	**77.7**	*0.19*	**74.4**	*0.32*	**73.1**	*0.46*	**57.9**	*0.70*	**64.1**	*7.07*	**62.5**	*4.86*	**62.1**	*0.39*
CaO	**0.880**	*0.05*	**0.880**	*0.05*	**0.230**	*0.04*	**0.840**	*0.20*	**6.59**	*0.73*	**5.11**	*2.29*	**5.66**	*1.49*	**1.81**	*0.07*
Rb	**143**	*7.89*	**130**	*11.22*	**127**	*7.02*	**113**	*5.67*	**37.5**	*9.12*	**35.4**	*10.04*	**23.5**	*2.41*	**526**	*19.27*
Sr	**58.2**	*2.98*	**77.1**	*8.47*	**2.08**	*0.65*	**44.7**	*3.21*	**388**	*126.07*	**518**	*44.30*	**588**	*52.42*	**8.37**	*1.48*
Y	**28.0**	*2.48*	**33.6**	*3.57*	**145**	*11.33*	**44.3**	*1.97*	**49.3**	*13.10*	**24.8**	*4.41*	**21.4**	*2.19*	**104**	*6.75*
Zr	**96.3**	*7.30*	**135**	*20.64*	**1110**	*95.67*	**356**	*12.40*	**243**	*62.28*	**155**	*15.87*	**169**	*14.85*	**1470**	*58.94*
Nb	**9.30**	*0.47*	**9.96**	*0.55*	**213**	*13.02*	**24.9**	*1.03*	**8.55**	*2.05*	**7.41**	*3.72*	**6.35**	*0.67*	**199**	*10.13*
Cs	**7.61**	*0.50*	**7.05**	*0.67*	**1.44**	*0.24*	**4.66**	*0.41*	**2.15**	*0.56*	**1.47**	*1.48*	**0.459**	*0.15*	**59.2**	*2.22*
Ba	**889**	*47.33*	**905**	*54.67*	**162**	*15.76*	**758**	*71.70*	**554**	*104.15*	**608**	*146.09*	**527**	*49.87*	**2.67**	*6.26*
La	**30.8**	*1.56*	**32.6**	*2.99*	**146**	*8.77*	**31.0**	*1.36*	**21.0**	*4.43*	**20.6**	*2.92*	**16.0**	*1.97*	**240**	*12.91*
Ce	**57.9**	*2.23*	**60.3**	*3.08*	**285**	*15.96*	**68.6**	*3.58*	**43.3**	*9.99*	**36.8**	*6.89*	**30.3**	*2.30*	**384**	*15.59*
Pr	**6.42**	*0.54*	**6.95**	*0.80*	**34.6**	*2.56*	**7.40**	*0.47*	**6.56**	*1.51*	**4.91**	*0.80*	**4.31**	*0.44*	**42.2**	*1.43*
Nd	**22.5**	*2.50*	**25.8**	*2.98*	**139**	*13.59*	**28.4**	*2.29*	**30.9**	*6.82*	**20.5**	*4.08*	**18.7**	*2.51*	**149**	*2.92*
Sm	**4.85**	*0.97*	**5.55**	*0.86*	**27.2**	*2.98*	**6.66**	*0.65*	**7.96**	*2.42*	**4.50**	*1.19*	**4.83**	*2.75*	**25.8**	*1.18*
Eu	**0.542**	*0.13*	**0.631**	*0.15*	**6.06**	*0.89*	**0.873**	*0.13*	**1.88**	*0.51*	**1.37**	*0.64*	**1.25**	*0.30*	**1.38**	*0.25*
Gd	**4.07**	*0.70*	**5.11**	*1.03*	**27.6**	*3.94*	**6.64**	*1.05*	**9.46**	*2.56*	**4.62**	*1.49*	**4.50**	*0.94*	**19.4**	*2.36*
Tb	**0.707**	*0.07*	**0.816**	*0.24*	**4.34**	*0.36*	**1.10**	*0.09*	**1.50**	*0.38*	**0.836**	*0.39*	**0.748**	*0.22*	**2.90**	*0.20*
Dy	**4.27**	*0.60*	**5.52**	*0.80*	**26.6**	*2.62*	**7.18**	*0.75*	**8.60**	*2.52*	**4.65**	*1.09*	**3.95**	*0.88*	**16.2**	*1.24*
Ho	**0.961**	*0.16*	**1.15**	*0.29*	**5.34**	*0.50*	**1.48**	*0.22*	**1.70**	*0.46*	**1.03**	*0.33*	**0.762**	*0.17*	**3.24**	*0.34*
Er	**2.87**	*0.47*	**3.50**	*0.79*	**14.6**	*0.84*	**4.50**	*0.30*	**5.47**	*1.48*	**2.31**	*0.39*	**2.14**	*0.57*	**9.16**	*0.68*
Tm	**0.466**	*0.07*	**0.520**	*0.17*	**2.19**	*0.22*	**0.724**	*0.11*	**0.760**	*0.23*	**0.355**	*0.11*	**0.354**	*0.10*	**1.49**	*0.12*
Yb	**3.46**	*0.42*	**3.96**	*0.78*	**16.3**	*2.39*	**5.43**	*0.51*	**5.41**	*1.34*	**3.00**	*0.77*	**2.34**	*0.55*	**10.4**	*1.28*
Lu	**0.549**	*0.12*	**0.634**	*0.10*	**2.31**	*0.23*	**0.812**	*0.11*	**0.809**	*0.22*	**0.351**	*0.10*	**0.342**	*0.09*	**1.66**	*0.17*
Hf	**3.64**	*0.41*	**5.05**	*0.90*	**27.6**	*2.84*	**9.63**	*0.82*	**6.97**	*1.83*	**4.22**	*0.69*	**4.75**	*0.90*	**31.0**	*1.13*
Ta	**0.940**	*0.16*	**1.07**	*0.21*	**13.6**	*0.72*	**1.85**	*0.17*	**0.709**	*0.20*	**0.589**	*0.25*	**0.55**	*0.12*	**10.3**	*0.97*
Pb	**20.4**	*1.13*	**21.1**	*2.15*	**22.1**	*2.09*	**18.5**	*4.02*	**12.0**	*2.73*	**9.24**	*4.46*	**7.28**	*1.53*	**98.8**	*11.85*
Th	**16.8**	*1.14*	**17.8**	*2.15*	**20.8**	*2.09*	**12.1**	*0.67*	**6.58**	*1.69*	**4.97**	*1.18*	**2.94**	*0.40*	**142**	*7.53*
U	**3.64**	*0.32*	**3.42**	*0.33*	**5.25**	*0.57*	**5.05**	*0.36*	**2.19**	*0.61*	**1.55**	*0.47*	**0.945**	*0.11*	**32.8**	*2.33*

Table 3.13 Trace element concentrations in a compositional suite of tephra samples (ppm) and SiO_2wt% and CaOwt% to 3 sig. figs. in samples of natural compositions. Element concentrations were obtained from the average of a series of analyses at 20 µm crater diameter. Standard deviation of averages to 2 decimal places given in italics.

3.2 Assessment of Existing Fractionation Correction

Pearce *et al.* (2011) calculated a fractionation factor to correct for element fractionation using 20 µm and 10 µm crater diameters. This fractionation factor is tested below in order to assess the need to further investigate element fractionation.

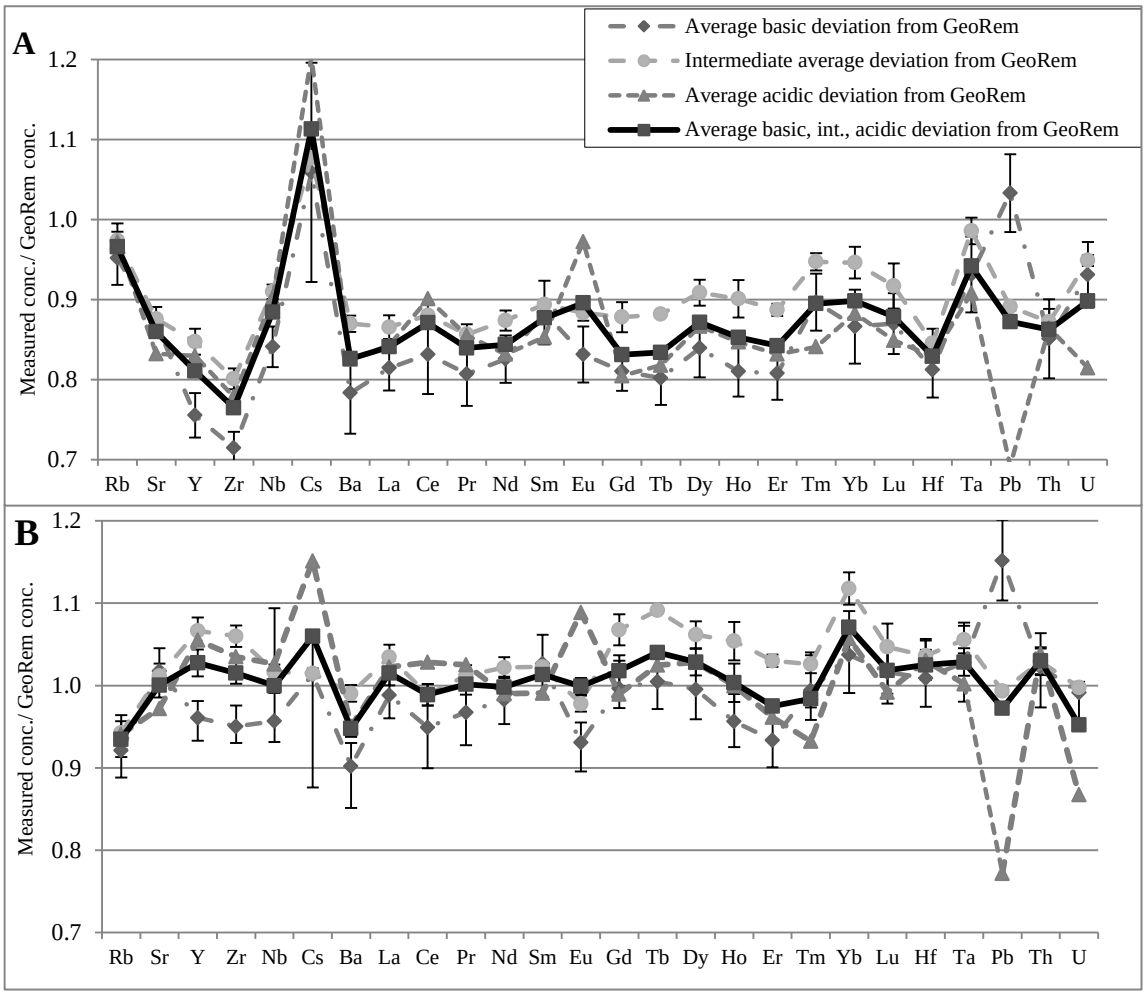

Fig. 3.20 Average deviations from GeoReM concentrations. Analyses were conducted at 20 µm crater diameters; A) shows analyses with no fractionation correction, B) shows analyses with the fractionation factor of Pearce *et al.* (2011) applied.

The results of a series of analyses conducted on basic reference materials (BCR-2G, BHVO-2G, KL2-G and GOR 132G), intermediate reference materials (StHs/680-G and T1-G) and an acidic reference material (ATHO-G) at a 20 µm crater diameter are presented in Fig 3.20 A and B. The accuracy of measured concentrations was monitored by dividing them by GeoReM certified concentrations (Table 3.12; Jochum *et al.*, 2006). Ratios from GeoReM for basic, intermediate and acidic compositions were averaged and an overall average deviation from GeoReM was calculated. A ratio of 1 indicates the measured

concentration is close to the certified concentration. Without fractionation correction (Fig. 3.20 A), element concentrations are typically measured at 85-90% of GeoReM concentrations. However, some elements are more dramatically offset; Zr is measured at on average ~75-80 % of certified concentrations. Measured concentrations are similarly offset in different compositions, although Pb and Cs biases are governed by composition. Caesium is generally overestimated, with biases more dramatic in acidic glasses compared with intermediate and basic glasses, deviating by +11%, +8% and +6% from certified concentrations, respectively. Lead shows the opposite behaviour, being underestimated by 31% in acidic glasses, underestimated by 11% in intermediate glasses and overestimated by 5% in basic glasses.

This bias from certified concentrations is caused by element fractionation. Pearce *et al.* (2011) analysed basic (BHVO-2G and BCR-2G), intermediate (T1-G) and acidic (ATHO-G) reference materials at 20 µm crater diameters using an identical laser set-up to this study (Fig. 3.21). Zirconium was represented at ~75% of reported concentrations and Rb was overrepresented by ~5% in all compositions, contrasting with the average ~5% underestimation of Rb in this study. Pearce *et al.* (2011) also highlighted the compositional control of Pb and Cs fractionation, yet found Cs to be more fractionated (+30%) in ATHO-G.

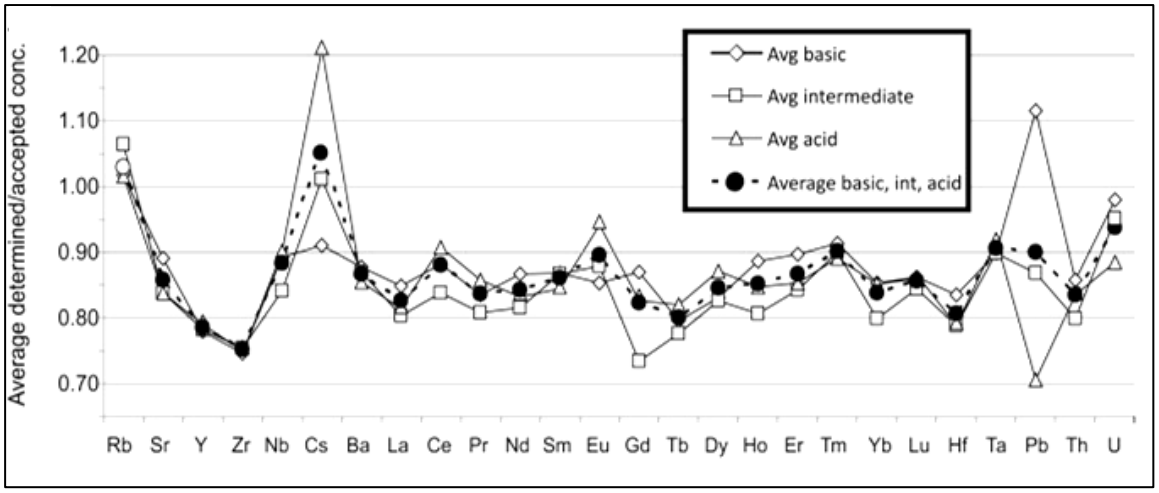

Fig. 3. 21 Average measured divided by accepted concentrations for basic glasses (BCR-2G, BHVO-2G), intermediate glass (T1-G) and acidic glass (ATHO-G), from Pearce *et al.* (2011).

The fractionation factor calculated by Pearce *et al.* (2011) for correcting the fractionation of measured concentrations from 20 µm and 10 µm crater diameters is applied to analyses of MPI-DING reference materials in Fig. 3.20 B. Measured concentrations of Cs, Zr, Pb and U, previously dramatically fractionated, are brought closer to the GeoReM concentrations by on average 5%. However, it is apparent that some elements remain offset from the certified concentrations in different compositions. For example, Cs remains overrepresented by 8% in acidic glasses, Nb remains underestimated by 18% in basic glasses, Pb remains underestimated by 23% in acidic samples and U is still underrepresented by 13% in acidic glasses. This illustrates the need to further investigate element fractionation.

3.3 The Response of Tephra Samples and Reference Materials to Fractionation

Pearce *et al.* (2011) studied fractionation associated with polymerisation using four calc-alkaline tephra samples. This study will investigate the fractionation of a wider range of natural glass compositions, including USGS and MPI-DING reference materials. The fractionation of reference materials and natural samples is compared here in order to assess whether they fractionate differently and should therefore be investigated separately.

The USGS reference materials, BHVO-2G and BCR-2G, were manufactured by melting powdered basalt at 1540^{o}C in a nitrogen atmosphere (Jochum *et al.*, 2005). The MPI-DING reference materials ATHO-G, T1-G, StHs/680-G, KL2-G and GOR 132G were made by fusing and stirring rock powders at 1400^{o}C-1600^{o}C for 1 hour and transferring the melts to another kiln to cool over a 12 hour period (Jochum *et al.*, 2005). The NIST 612 and NIST 610 USGS reference materials, commonly used as calibration standards, are synthetic soda lime glasses prepared by melting high purity sand, alumina, soda ash and calcium carbonate at ~1500^{o}C. Melts were then spiked with ~50 ppm (NIST 612) and 500 ppm (NIST 610) of trace elements (Pearce *et al.*, 1997; Kane, 1998). Kempenaers *et al.* (2003) cited the differential fractionation of the NIST reference materials associated with their synthetic matrix. Although the MPI-DING reference materials and BCR-2G and BHVO-2G have geological matrices, they have been artificially manufactured and may therefore respond to fractionation differently.

In Fig. 3.30, the average RSD% for repeat analyses on reference materials and tephra samples (of natural compositions) is plotted against analysis crater diameter (20 µm, 10 µm, 6 µm and 4 µm). Although scatter generally increases with decreasing crater diameter, samples of natural composition are more scattered than reference materials; this may be due to compositional heterogeneity within the sample glass or accidental ablation of microcrysts (Tomlinson *et al.*, 2010). The SiO_2wt% of each reference material and tephra samples is plotted against a fractionation index (F.I.) for Zr, Y and Rb in Fig. 3.31. The F.I. was calculated, after Pearce *et al.* (2011), by dividing average concentrations at a particular crater diameter by concentrations obtained at 20 µm crater diameters. The fractionation of reference materials and tephra samples is consistent. Therefore, in this study, the fractionation of reference materials and samples of natural composition will be investigated collectively.

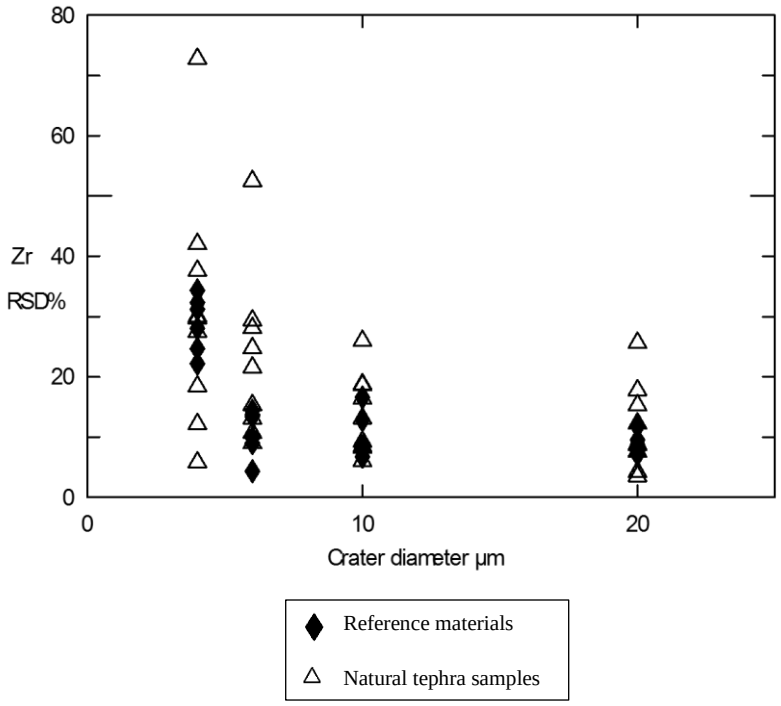

Fig. 3.30 Graph showing increase in RSD% (standard deviation/average) with decreasing crater diameter, for samples of natural composition and reference materials.

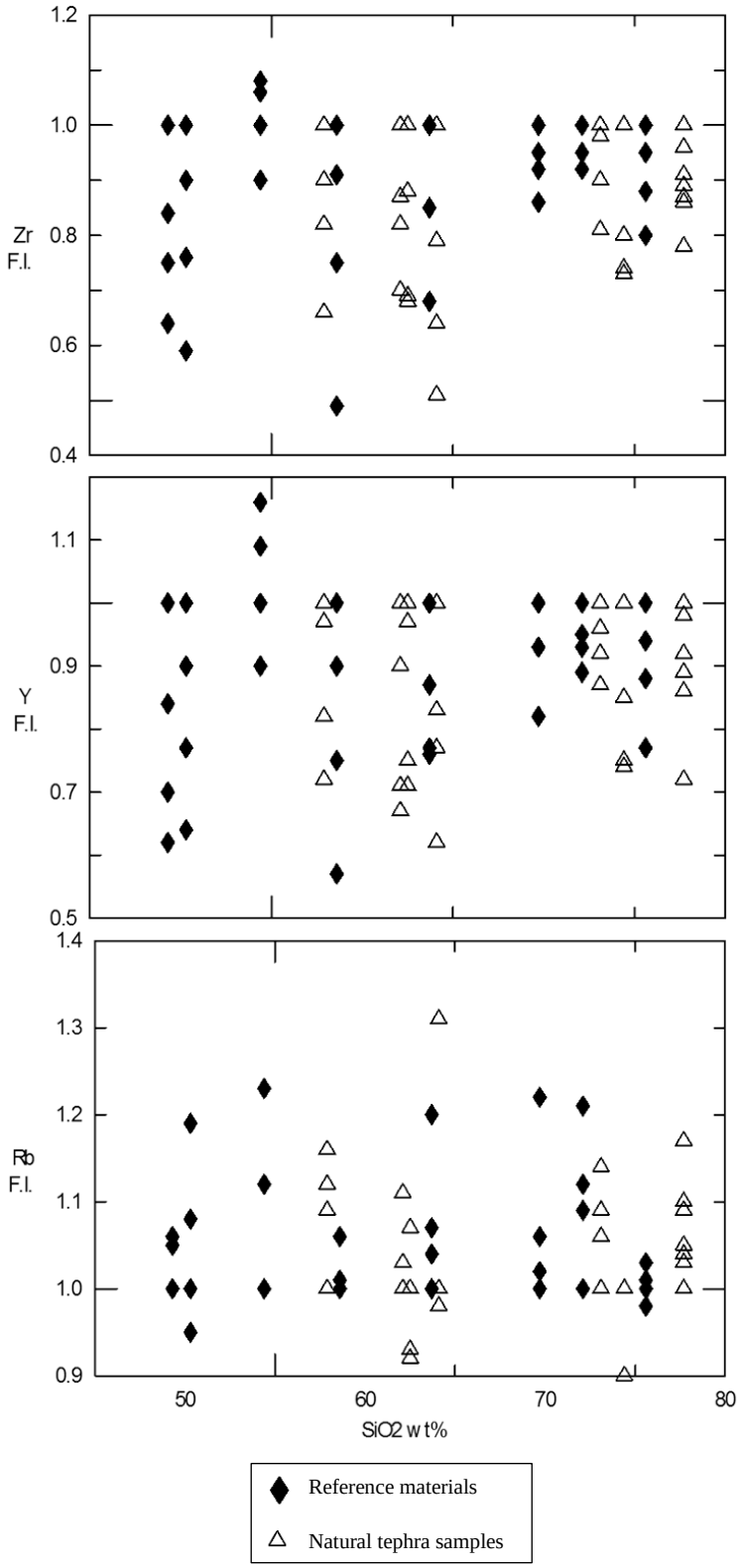

Fig. 3.31 Graphs show F.I. (conc. at *x* µm crater diameter / conc. at 20 µm crater diameter) plotted against SiO_2 wt% of 15 samples analyses using a range of crater diameters for samples of natural compositions and reference materials.

Chapter 4 Element Fractionation

4.1 The Impact of Crater Diameter on Fractionation

Crater size has been widely cited as a cause of fractionation during LA-ICP-MS analysis (Eggins *et al.,* 1998; Tomlinson *et al.,* 2010; Pearce *et al.,* 2011). In this section the impact of crater size on fractionation will be explored. All analyses are fractionation corrected using the Pearce *et al.* (2011) 20 µm crater diameter fractionation factor.

Ratios of measured concentrations in ATHO-G (acidic), StHs/680-G, T1-G (intermediate) BCR-2G, BHVO-2G, KL2-G (basic) to certified GeoReM concentrations are plotted for different crater diameters in Fig. 4.10 and 4.11. Measured concentrations of the HFSE and LREE deviate increasingly from the certified concentrations with decreasing crater diameter. The overall deviation (average of acidic, intermediate and basic deviations) from certified concentrations for Zr is +2% at 20 µm crater diameters, -8% at 10 µm crater diameter, -17% at 6 µm crater diameters and -25% at 4 µm crater diameters. The offset of the MREE and HREE at 4 µm crater diameters is more erratic, possibly due to low counts using 4 µm crater diameters. The focus of this study will therefore be on the fractionation of the HFSE and LREE.

Measured concentrations of Zr, Pr and Rb in ATHO-G are plotted against crater diameter (Fig. 4.12). Concentrations measured from 20 µm crater diameters are closest to certified concentrations. Measured concentrations of Zr and Pr decrease with decreasing crater diameter, whilst Rb concentrations show a marginal increase with decreasing crater diameter. Additionally, the scatter increases with decreasing crater diameter, (see Fig. 3.30), measured concentrations at 20 µm and 10 µm crater diameters have an RSD of ~ 10% and 6 µm and 4 µm crater diameters have errors of 15% and 30%, respectively.

Fractionation associated with crater diameter is investigated further by calculating a fractionation index (F.I) (after Pearce *et al.,* 2011). Concentrations measured using 10 µm, 6 µm and 4 µm crater diameters were each averaged and divided by average 20 µm crater diameter concentrations to give a fractionation index for each sample. F.I. is plotted against crater diameter in Figs. 4.13; an F.I. of 1 indicating no fractionation has occurred.

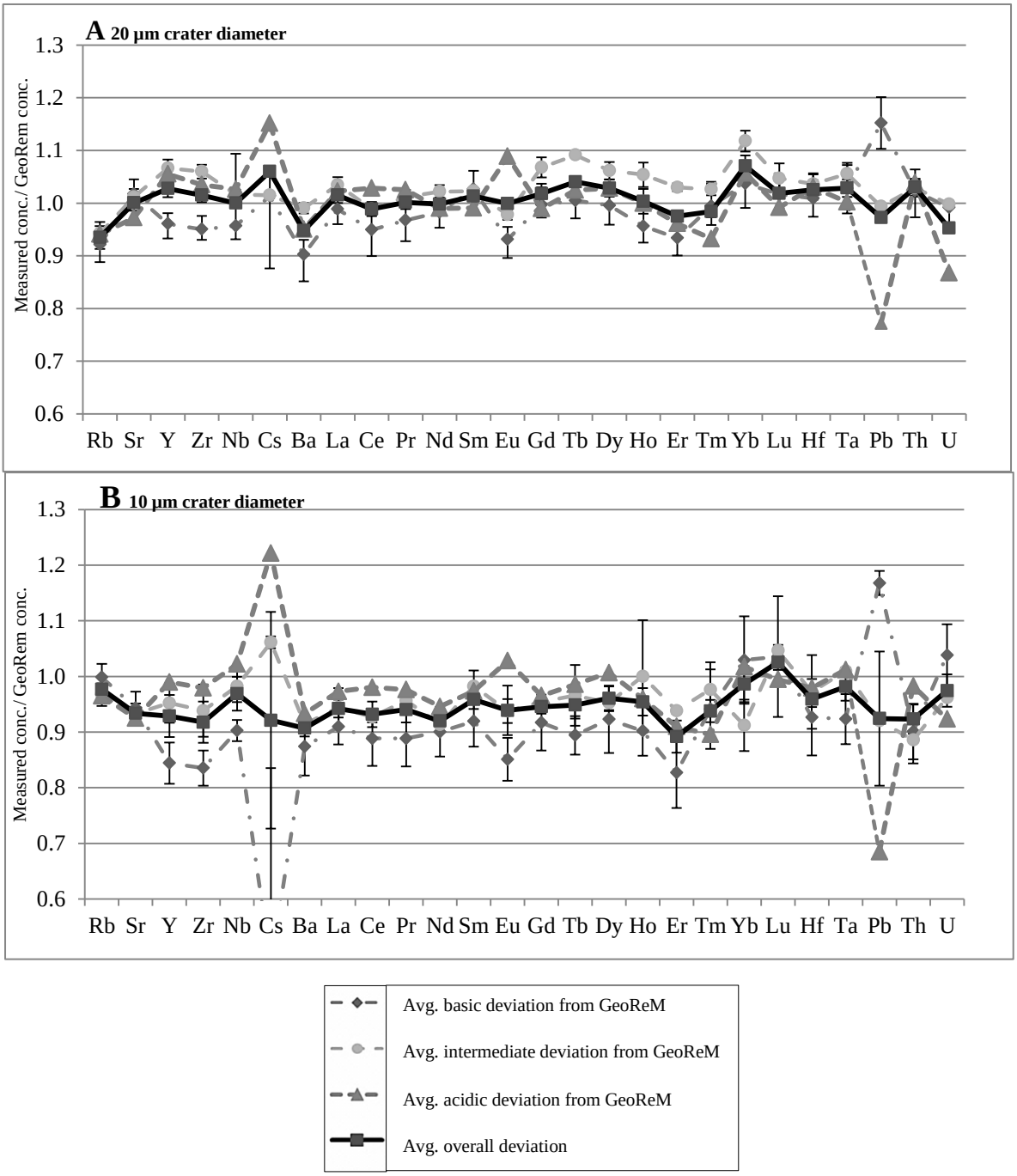

Fig. 4.10 Average of determined/accepted concentrations using A) 20 µm crater diameters and B) 10 µm crater diameter, for basic compositions (BCR-2G, BHVO-2G and KL2-G), intermediate compositions (StHs/680-G and T1-G) and acidic compositions (ATHO-G). Analyses undertaken at 24.2 kV, 5 Hz, 10 Jcm^{-2} and calibrated against NIST 612 20 µm crater diameter spectra with ^{29}Si as the internal standard. Pearce *et al.* (2011) 20 µm crater diameter fractionation factor applied to analyses at all crater diameters.

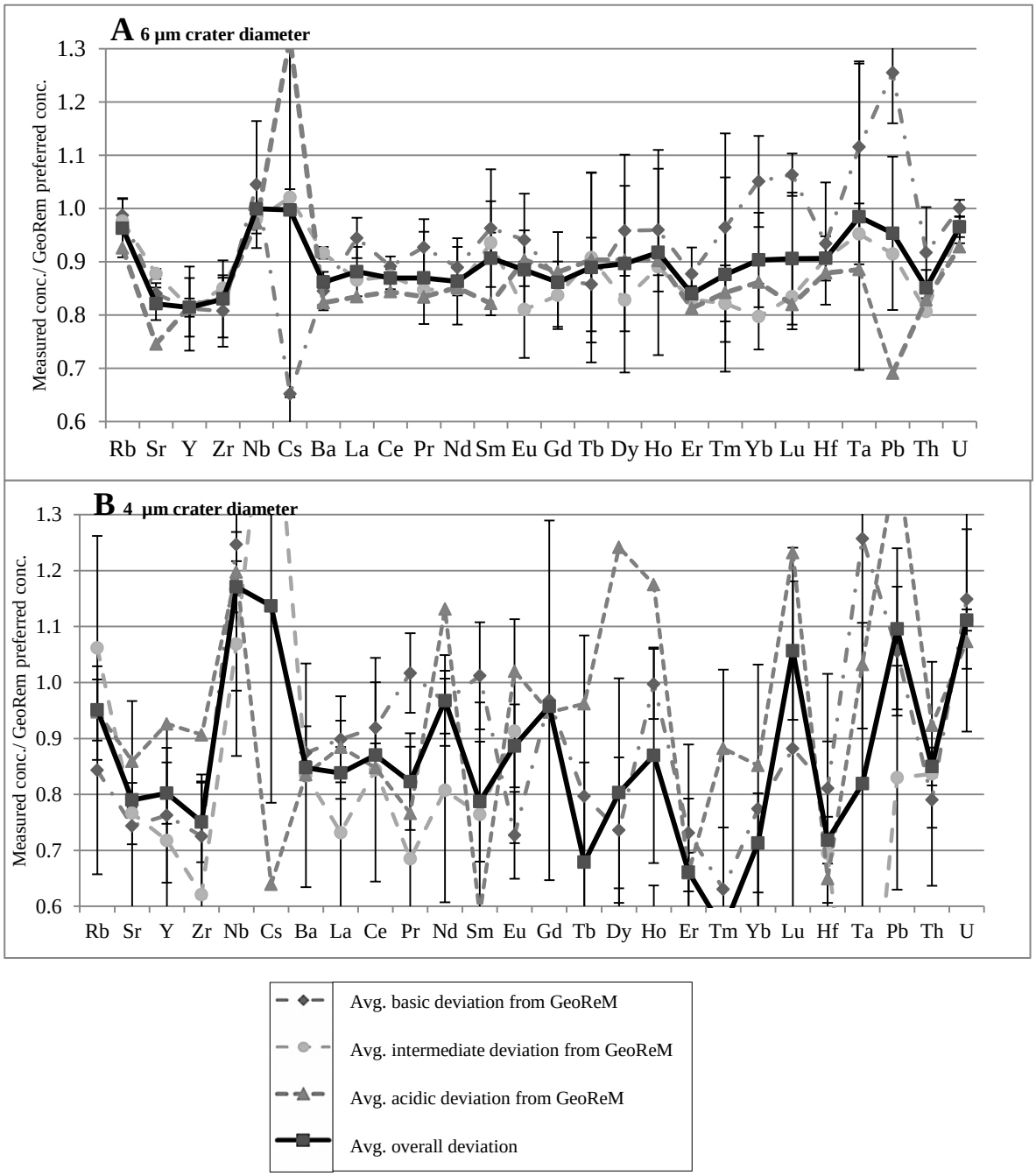

Fig. 4.11 Average of determined/accepted concentrations using A) 6 µm crater diameters and B) 4 µm crater diameter, for basic compositions (BCR-2G, BHVO-2G and KL2-G), intermediate compositions (StHs/680-G and T1-G) and acidic compositions (ATHO-G). Analyses undertaken at 24.2 kV, 5 Hz, 10 Jcm^{-2} and were calibrated against NIST 612 20 µm crater diameter spectra with ^{29}Si as the internal standard. Pearce *et al.* (2011) 20 µm crater diameter fractionation factor applied to analyses at all crater diameters.

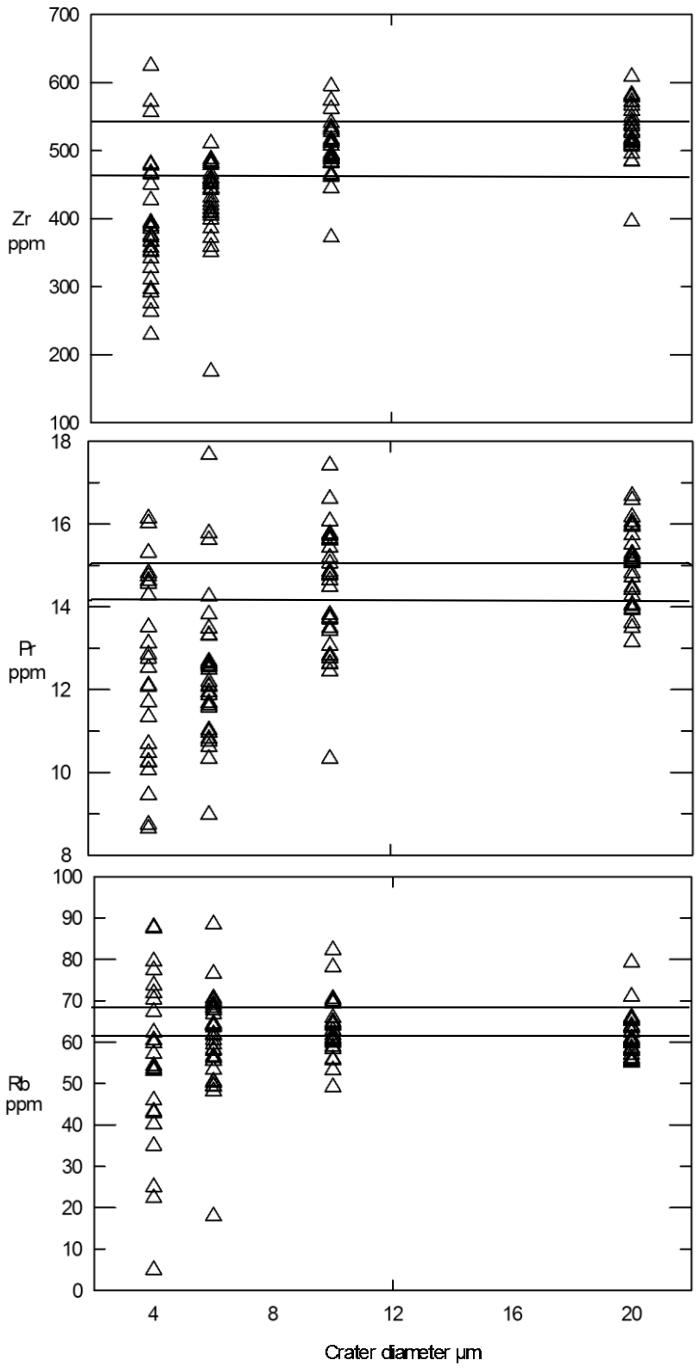

Fig. 4.12 Average concentrations of Zr, Pr and Rb in ATHO-G obtained over six sessions of five repeat analyses at 20 µm, 10 µm, 6 µm and 4 µm crater diameters. Horizontal lines represent ± one standard deviation of GeoReM certified values. Analyses were conducted under identical laser operating conditions (24.2 kV, 5 Hz and 10 Jcm^{-2}) calibrated against 20 µm crater diameter NIST 612 acquisitions with ^{29}Si as the internal standard. Analyses are fractionation corrected against the 20 µm crater diameter fractionation factor from Pearce *et al.* (2011).

Fractionation generally increases as crater diameters decrease, with elements either underestimated or overestimated. Zr is strongly fractionated and on average underestimated by ~10% using 10 µm crater diameters, ~20% using 6 µm crater diameters and by ~25% using 4 µm crater diameters. Strontium, Th and Ce also appear increasingly fractionated with decreasing crater diameter. The fractionation of Ba is less systematic, possibly due to increased analytical noise for this element. In contrast, the volatile elements Rb and Cs become increasingly overrepresented as a function of decreasing crater diameter, at 6 µm crater diameter Rb is overrepresented by ~5% and at 4 µm Rb is overrepresented by ~10% relative to 20 µm concentrations.

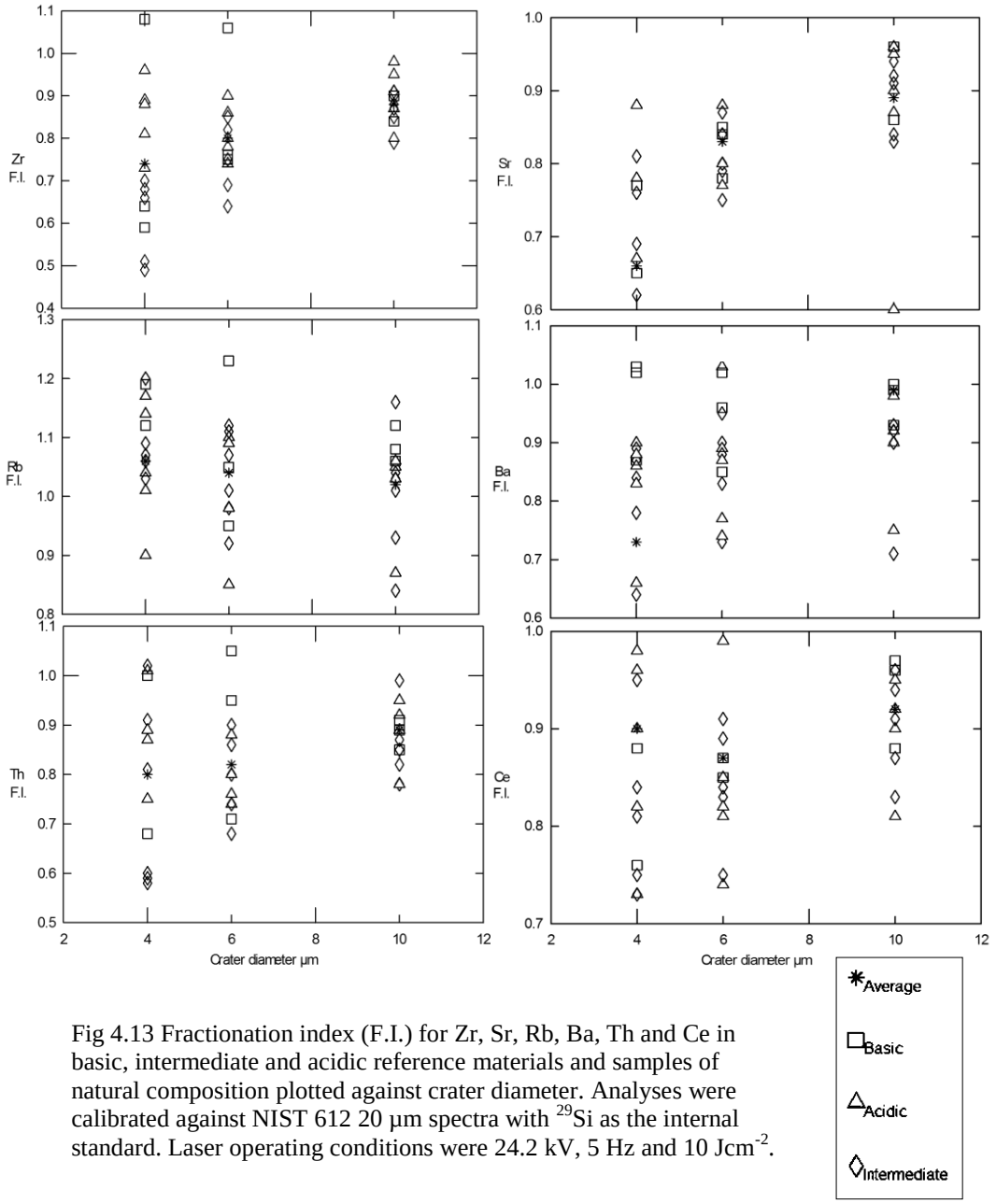

Fig 4.13 Fractionation index (F.I.) for Zr, Sr, Rb, Ba, Th and Ce in basic, intermediate and acidic reference materials and samples of natural composition plotted against crater diameter. Analyses were calibrated against NIST 612 20 µm spectra with ^{29}Si as the internal standard. Laser operating conditions were 24.2 kV, 5 Hz and 10 Jcm^{-2}.

4.1.1. Discussion of Element Fractionation associated with Crater Diameter

Pearce *et al.* (2011) found an increase in fractionation related to decreasing crater diameter, with Zr underestimated in acidic glasses by 20% at 10 µm crater diameters, ~45% at 6 µm crater diameters and ~65% at 4 µm crater diameter relative to concentrations measured from 20 µm crater diameters. Tomlinson *et al.* (2010), conducted analyses at crater diameters of 57 µm, 34 µm and 15 µm on the MPI-DING reference materials ATHO-G, StHs/680-G, ML3-B and GOR 128-G. Tomlinson *et al.*(2010) noted Zr concentrations in StHs/680-G were offset by -10% using 57 µm crater diameter and -15% using 34 µm crater diameter. Pearce *et al.* (2011) found those elements with a high charge, e.g. Zr^{4+}, responded dramatically to fractionation, as seen in this study. Pearce *et al.* (2011) described the presence of a ~0.5 µm thick melt film lining the ablation craters, similar to that noted by Eggins *et al.* (1998). Elements are either volatilised from or retained within this melt, which makes up an increasing proportion of craters with decreasing crater diameter (Pearce *et al.* 2011). Fractionation from this melt film therefore becomes more significant with decreasing crater diameter, explaining the fractionation trends noted in this study. The increase in scatter with decreasing crater diameter seen in this study has also been noted by Tomlinson *et al.* (2010), Pearce *et al.* (2011) and Jenner and O'Neill (2012). Tomlinson *et al.*(2010) associated the increased scatter with loss of counts and reported average precisions of 6% at 57 µm, 9% at 34 µm and 26% at 15 µm; the latter comparable with the ~20% error using 10 µm crater diameters seen in this study.

With decreasing crater diameter the homogeneity of MPI-DING reference glasses becomes increasingly uncertain, with tests only guaranteeing homogeneity when volumes of 30 x 30 x 30 μm^3 to 50 x 50 x 50 μm^3 are sampled (Kempenaers *et al.,* 2003; Jochum *et al.,* 2005; Borisova *et al.,* 2010; Pearce *et al.,* 2011). Thus, some increased scatter with decreasing crater diameter may also be a result of compositional heterogeneity.

4.2 The Response of Trace Elements to Fractionation

Numerous studies have considered element fractionation associated with condensation temperature, ionic radius, ionization energy and other element properties (Jeffries *et al.*, 1997; Chen, 1999; Tomlinson *et al.*, 2010). In Fig. 4.20 the average 10 µm crater diameter F.I. of 26 trace elements in BCR-2G, BHVO-2G, KL2-G, T1-G, StHs/680-G and ATHO-G is plotted against various indicators of element behaviour.

Ionic radius, charge, field strength, electronegativity, condensation temperature and ionization do not appear to control element fractionation. Generally the large ion lithophile elements (LILE) (e.g. Rb and Cs) appear overrepresented whilst the HFSE and REE (e.g. Zr, Ce, Pr) are commonly underrepresented. Higher charge elements appear more fractionated (see Fig. 4.20 A), with 4^+ elements such as Zr and Th being ~10% more fractionated than 2^+ elements. Elements of a higher charge may be bound more tightly within the silicate matrix due to their smaller size, thus may be less easily removed during ablation (Pearce *et al.*, 2011). However, some elements of similar charge are differently fractionated; suggesting charge is neither a significant nor the sole influence on element fractionation.

Element fractionation does not vary systematically with ionic radius, field strength, condensation temperature or first ionization enthalpy (see Fig. 4.20). Additionally, elements with similar properties fractionate differently, suggesting other factors control element fractionation.

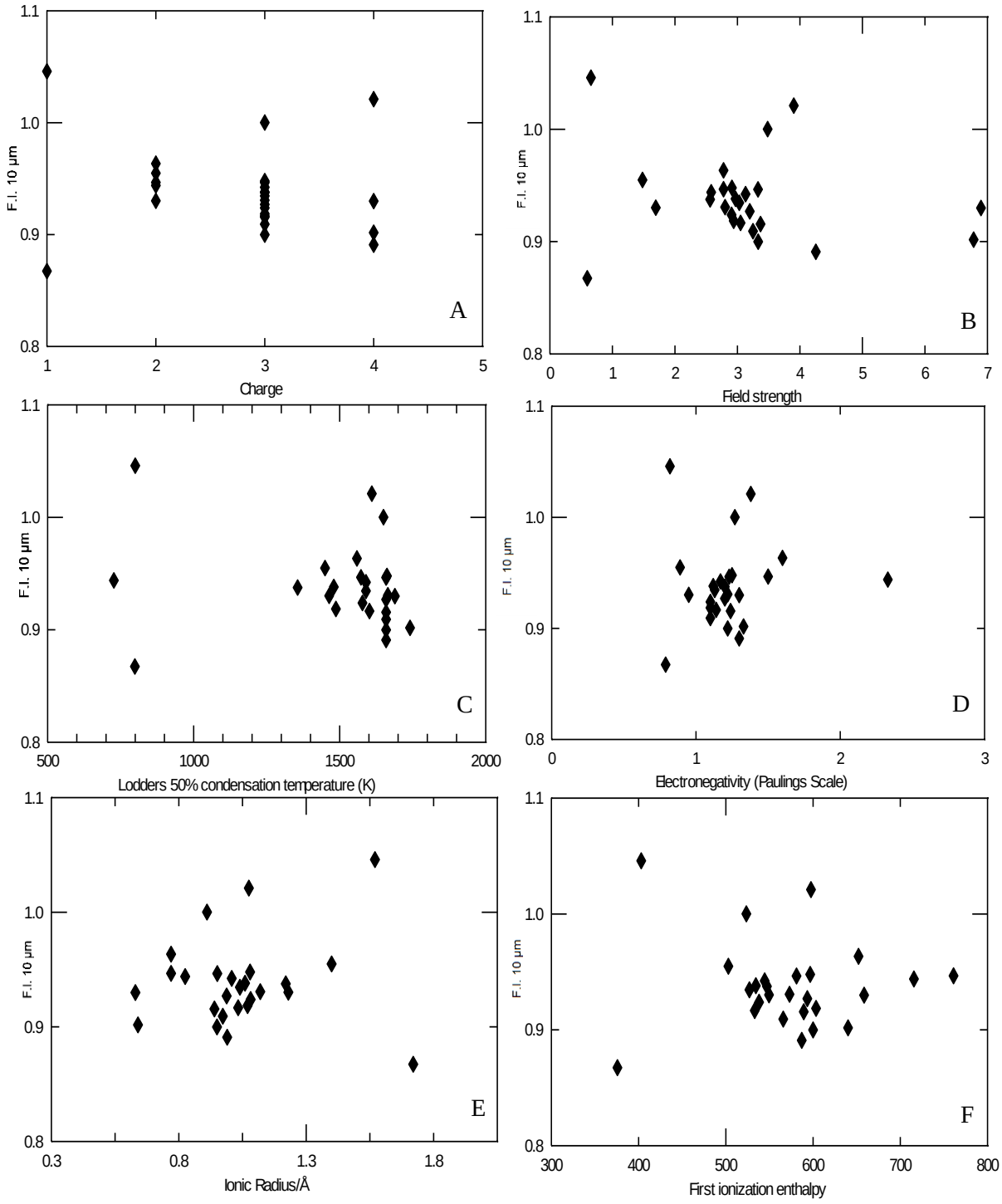

Fig. 4.20 Fractionation index for 26 trace elements in MPI-DING reference materials against A) charge B) field strength (charge/ionic radius) C) Lodders 50% condensation temperature (K) (from Lodders, 2003) D) Paulings electronegativity E) Ionic radius (Å) F) first ionization enthalpy (kJ mol^{-1}) (from James and Lord, 1992). Analyses were undertaken using 10 µm crater diameters, under identical operating conditions (5 Hz, 24.2 kV and 10 Jcm^{-2}) calibrated against 20 µm crater diameter NIST 612 spectra with ^{29}Si as the internal standard.

4.2.1 Discussion of element fractionation associated with element properties

Jeffries *et al.* (1997) stated the heavy rare earth elements (HREE) and high field strength elements (HFSE) are generally underrepresented during continued ablation, whilst LILE elements tend to be overrepresented, as seen in this study. Pearce *et al.* (2011) commented on the stronger fractionation of HFSE, e.g. Zr^{4+} with decreasing crater diameter, however, this study demonstrated that field strength does not clearly correlate with element fractionation.

Jeffries *et al.* (1997) used an IR laser to demonstrate a clear link between the fractionation of REE and their ionic radius. The study found that REE with a smaller ionic radius appeared more strongly underrepresented (see Fig. 4.21 A), suggesting elements with high charge and small ionic radius are bound more securely within the sample matrix and thus removed less easily during ablation. This study is not analogous to that of Jeffries *et al.* (1997), IR lasers ablate the sample through thermal erosion. The UV laser used in this study ablates through photo-ablation, causing differing fractionation effects (Pearce, *pers. comm.*). Chen (1999) studied the fractionation of Ca, V, Zn, Ga, Sr, La and Nd in NIST 613, BCR-2 and SY-4 using a 266 nm laser and found no influence of field strength and melting temperature on fractionation, yet reported a strong correlation between fractionation and the sum of first and second ionization enthalpies. Chen (1999) suggested that those elements of high ionization energy were ablated less easily from the sample and therefore became progressively enriched in the ablation pit, however, this correlation was not seen in this study.

Several studies have investigated element fractionation using a 193 nm laser, finding no correlation with element properties, as seen in this study. Using a 193 nm laser, Tomlinson *et al.* (2010) found Lodders (2003) 50% condensation temperature did not influence the fractionation of ATHO-G, StHs/680-G, ML3B, GOR128-G and NIST 612 (Fig. 4.22). When using a 193 nm laser Kuhn and Gunther (2004) also found no correlation between element melting and boiling points and the degree of laser induced element fractionation. Thus, it is possible that fractionation using the 193 nm Excimer laser utilised in this study is less influenced by element properties.

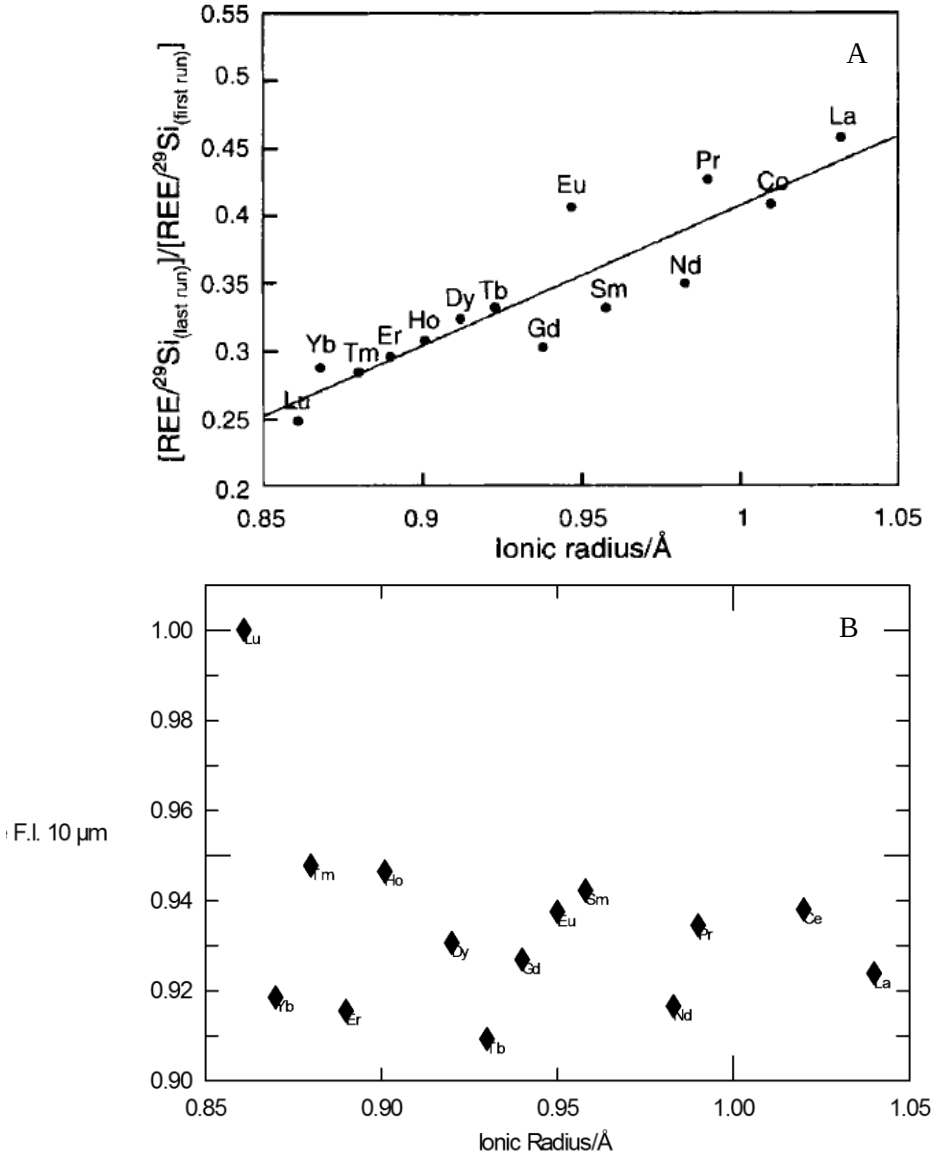

Fig. 4.21 A) Fractionation for the REE calculated as (REE/^{29}Si $_{(last\ run)}$)/ REE/^{29}Si $_{(first\ run)}$) in NIST 610 versus ionic radius (from Jeffries *et al.*, 1997), B) F.I. for the REE in MPI-DING reference materials analysed in this study against ionic radius.

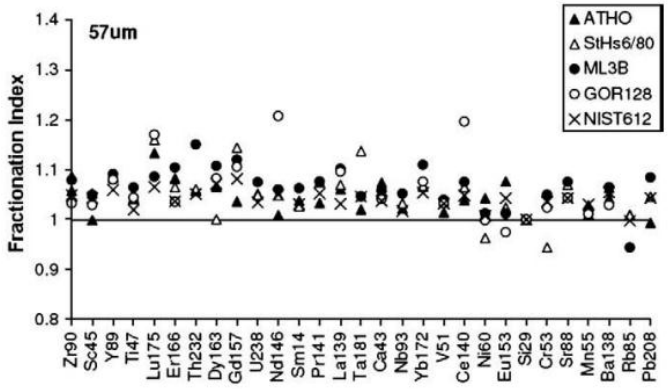

Fig. 4.22 Fractionation index (calculated as the mean intensity of the analyte mass/ mean intensity of the internal standard over the first 15 seconds versus the last 15 seconds of analysis) against elements ordered by Lodders (2003) 50% condensation temperature (left to right = decreasing temperature). From Tomlinson *et al.* (2010)

4.3 The Impact of Excitation Voltage on Element Fractionation

Numerous studies have linked fractionation to various laser operating conditions (eg. Sylvester, 2008); however, few have investigated the influence of excitation voltage on element fractionation. In this study, a constant laser energy output and repetition rate were used (respectively 10 Jcm^{-2} and 5 Hz), whilst the laser excitation voltage was altered from high (28 kV) to low (24.2 kV). Adjusting the laser excitation voltage whilst keeping other laser conditions identical may alter the laser pulse duration (Pearce *pers.comm.*).

Concentrations of trace elements in ATHO-G were measured using a 24.2 kV excitation voltage and a higher 28 kV excitation voltage whilst using a series of crater diameters. All analyses are fractionation corrected using the Pearce *et al.* (2011) 20 µm crater diameter fractionation factor. Using 20 µm and 10 µm crater diameters, measured concentrations of Zr, Y, Sr and REE obtained at a 28 kV excitation voltage are ~5% to 10% lower than concentrations measured using a 24.2 kV excitation voltage (Fig. 4.30 A and B). Additionally, measured concentrations of Rb are ~5% higher using an excitation voltage of 28 kV as opposed to 24.2 kV. However, excitation voltage does not systematically control the fractionation of Zr, Y, Sr and REE using 6 µm and 4 µm crater diameters (Fig. 4.31 A and B). This may be the result of the higher noise at 6 µm and 4 µm crater diameters.

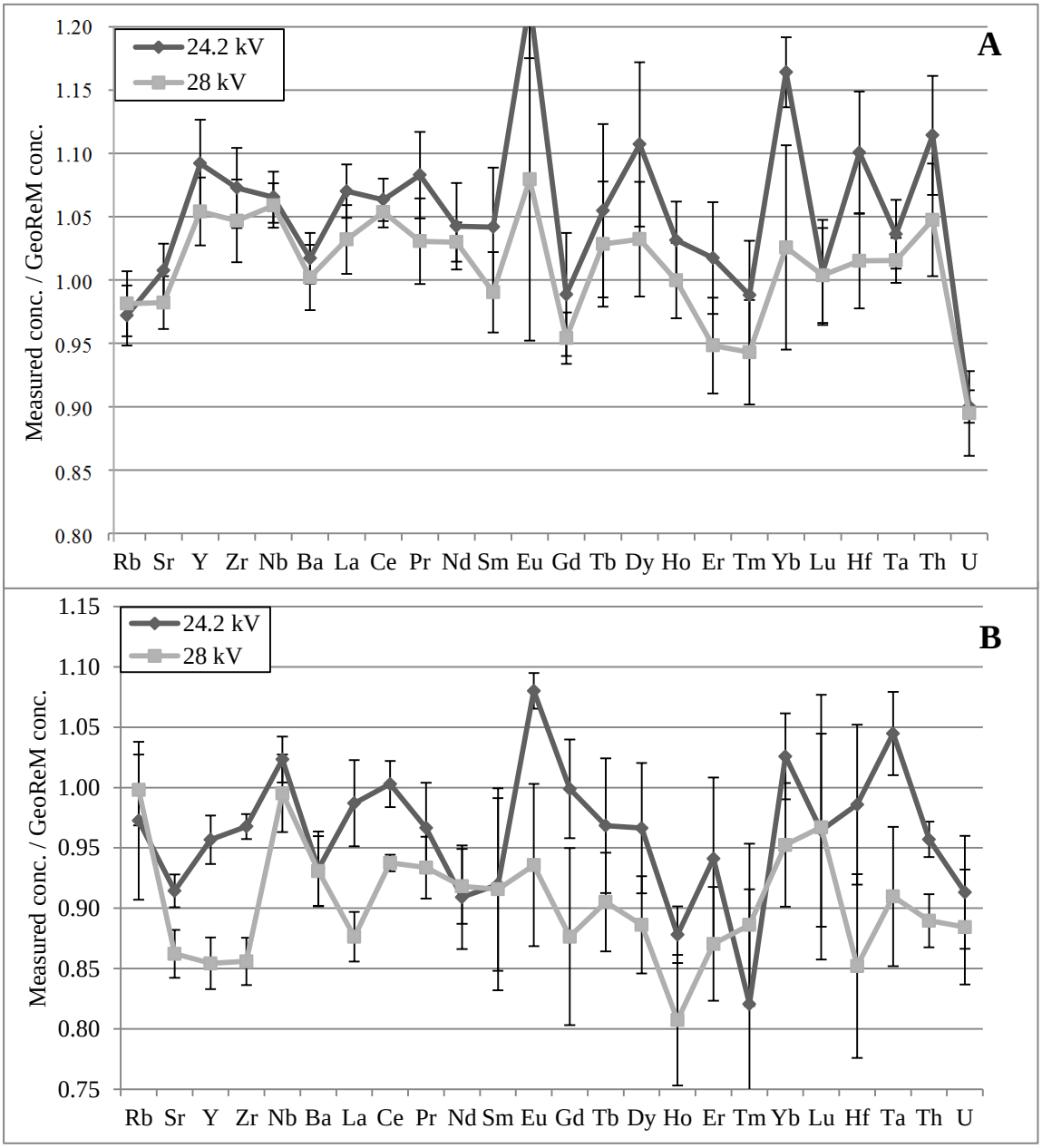

Fig. 4.30 Average measured concentrations/ accepted concentrations for ATHO-G, with analyses conducted at excitation voltages of 24.2 kV and 28 kV, and A) analyses conducted at 20 µm crater diameters and B) analyses conducted at 10 µm crater diameters. Results are from one day of analysis with the repetition rate and laser fluence kept the same (respectively 5 Hz and 10 Jcm^{-2}), analyses are calibrated against NIST 612 20 µm crater diameter acquisitions and using ^{29}Si as the internal standard. All analyses are fractionation corrected against the 20 µm crater diameter fractionation factor of Pearce *et al.* (2011). Error bars represent one standard deviation.

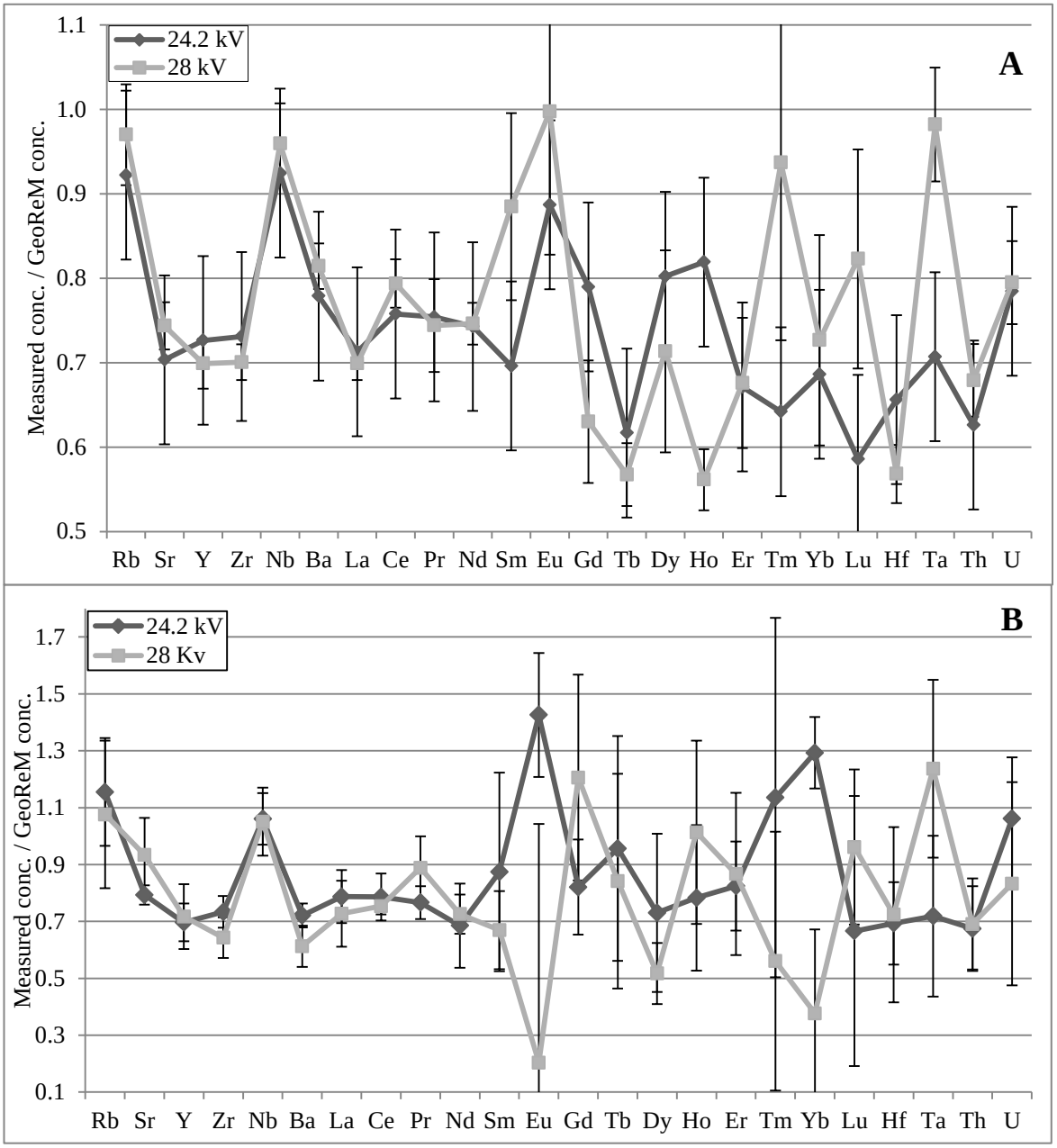

Fig. 4.31 Average measured concentrations/ accepted concentrations for ATHO-G, with analyses conducted at excitation voltages of 24.2 kV and 28 kV, and A) analyses conducted at 6 µm crater diameters and B) analyses conducted at 4 µm crater diameters. Results are from one day of analysis with the repetition rate and laser fluence kept the same (respectively 5 Hz and 10 Jcm^{-2}), analyses are calibrated against NIST 612 20 µm crater diameter acquisitions and using ^{29}Si as the internal standard. All analyses are fractionation corrected against the 20 µm crater diameter fractionation factor of Pearce *et al.* (2011). Error bars represent one standard deviation.

4.3.1. Discusssion of Element Fractionation Associated with Excitation Voltage

Using an ArF 193 nm Excimer laser, Feenstra *et al.* (1999) demonstrated that altering the excitation voltage from 4.1 kV to 7.9 kV increased the laser pulse duration from 55 ns to 80 ns. Few studies have studied the effect of excitation voltage on element fractionation.

Pearce *et al.* (2011) state that longer pulse durations may cause more sample heating, possibly promoting the formation of a melt film. Russo *et al.* (2002), Fernandez *et al.* (2007) and Pisonero and Gunther (2008) state that shorter pulse durations cause less energy to be lost to the sample through thermal dissapation, allowing stoichiometric aerosols to be formed. The majority of lasers used for LA-ICP-MS analysis are currently of a relatively long ~20 nanosecond (ns) pulse length. However, lasers with shorter pulse lengths of ~ 100 femtosecond (fs) have recently been coupled to ICP-MS with promising results (Pisonero and Gunther 2008; Borisova *et al.*, 2010; Pearce *et al.*, 2011). Compared with ns pulse durations, laser ablation using fs lasers causes little redeposition of the molten sample within craters, resulting in the formation of smaller particles which are vaporized more efficiently by the ICP-MS (Fig. 4.32). This means that fs-LA reduces fractionation effects when compared with ns-LA (Fernandez *et al.*, 2007; Borisova *et al.*, 2010).

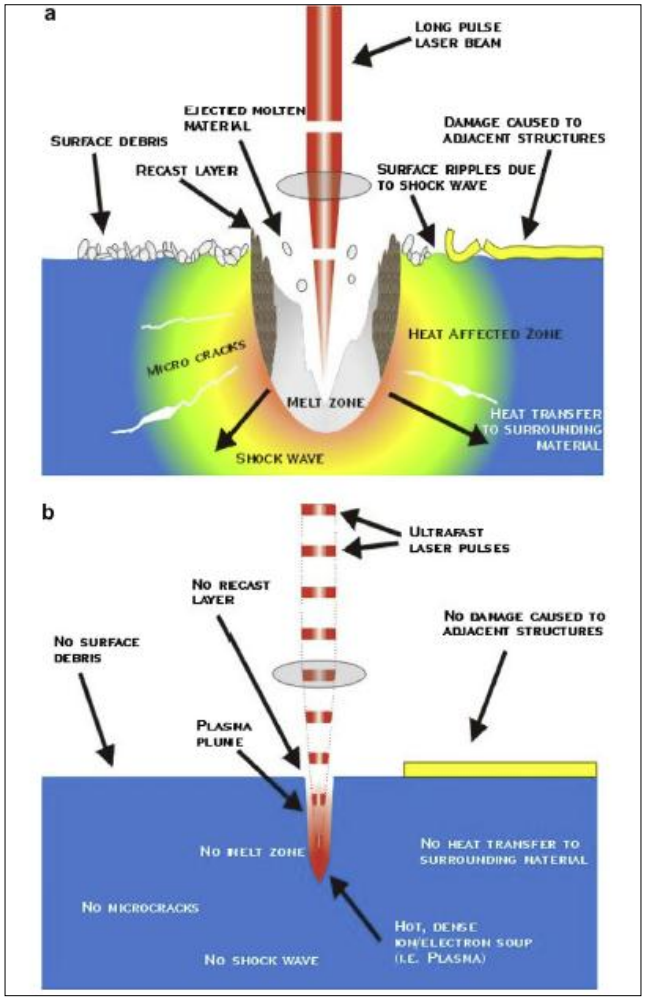

Fig. 4.32 Schematic of ablation using A) a femtosecond laser and B) using a nanosecond laser (from Ferrnandez *et al.*, 2007), with fs ablation causing less peripheral damage and avoiding the formation of a melt film.

Therefore, if excitation voltage is related to laser pulse duration it may influence element fractionation. Further research is required to ascertain the control excitation voltage exerts on laser pulse duration and in turn fractionation.

4.4 Element Fractionation and Composition

4.4.1 Fractionation associated with Concentration and Signal Intensity

Pearce *et al.* (2011) reported a systematic increase in element fractionation with decreasing polymerisation. This section will assess whether the correlation between element fractionation and polymerisation reported by Pearce *et al.* (2011) is simply related to changes in element concentration and signal.

Element concentration may vary systematically with bulk composition, e.g. commonly Zr concentrations are high in rhyolites and low in basalts (Pearce, *pers. comm.*). Variations in ablated volumes where the same crater diameter is used may cause differing fractionation effects in different sample (Pearce, *pers. comm.*)

In Fig. 4.40 F.I. is plotted against respective element concentrations. The fractionation of the HFSE and LILE is unrelated to their respective element concentration, with Ba consistently fractionated in samples containing ~100 – 1000 ppm Ba. Through plotting fractionation against signal intensity ratios (Zr cps/Si cps and Y/Si cps) there is no apparent or systematic relationship between the two factors (Fig. 4.41).

Therefore, fractionation is not associated with variations in element concentration and signal intensity. Variations in element fractionation between samples may be associated with composition and this will be explored in the following section.

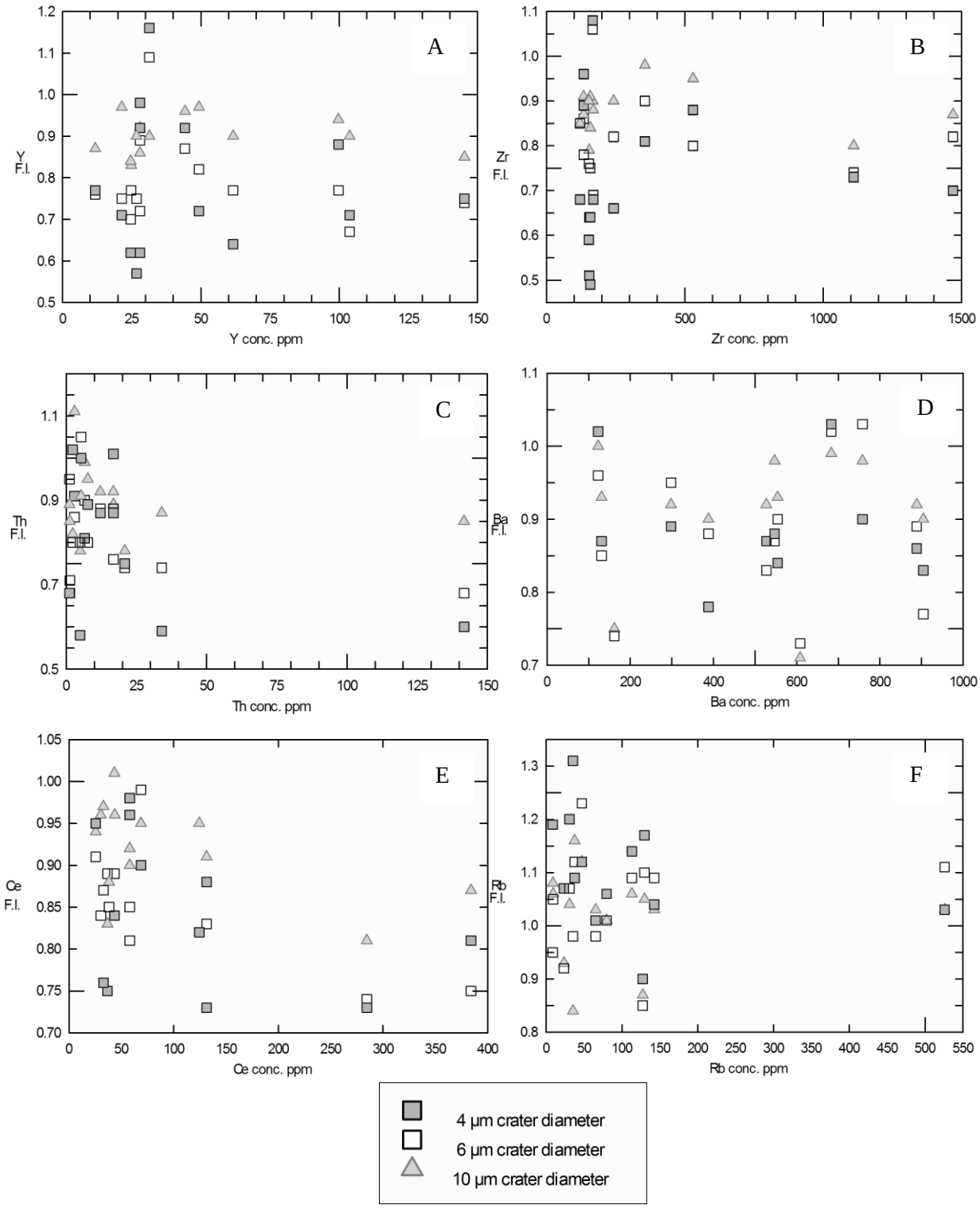

Fig. 4.40 Concentrations of A) Y, B) Zr, C) Th, D) Ba, E) Ce, F) Rb in 15 reference materials and tephra samples vs. the respective 10 µm, 6 µm, 4 µm crater diameter fractionation indices (F.I.). F.I. calculated as (concentration determined at *X* µm crater diameter/ concentration determined at 20 µm crater diameter). Analyses were conducted under identical laser operating conditions, calibrated against NIST 612 20 µm crater diameter acquisitions with ^{29}Si as the internal standard. Analyses were fractionation corrected against the 20 µm fractionation factor from Pearce *et al.* (2011).

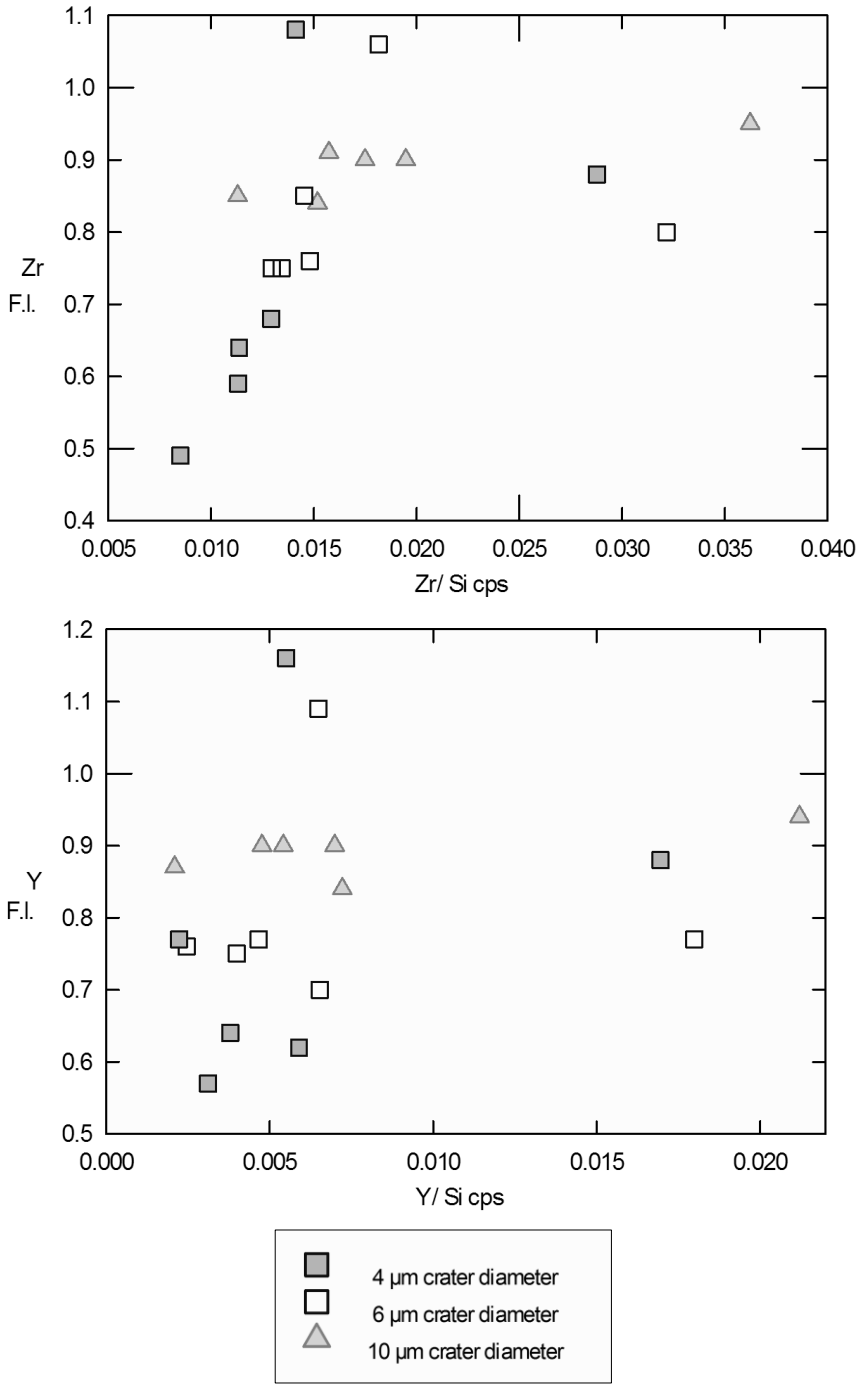

Fig. 4.41 Signal intensity ratio of Zr and Y counts per second (cps) divided by Si cps plotted against respectively Zr and Y fractionation indices. Average Zr and Y cps for 20 µm, 10 µm, 6 µm, 4 µm crater diameter acquisitions of basic (KL2-G, BHVO-2G, BCR-2G), intermediate (T1-G, St-Hs80G) and acidic (ATHO-G) MPI-DING reference materials divided by the average Si cps for each crater diameter. Analyses conducted under identical laser operating conditions.

4.4.2 The Control of Sample Matrix on Element Fractionation

Pearce *et al.* (2011) described a correlation between element fractionation and polymerisation (NBO/T). The influence of NBO/T on element fractionation will be tested here. In Figs. 4.42 to 4.44 F.I. is plotted against NBO/T; rhyolitic glasses are highly polymerised with an NBO/T= 0.

Zirconium, Y, Ce, Th, Ba and Rb are consistently fractionated (by ~10-20 %) in a range of differently polymerised glasses using 10 µm crater diameters. At 6 µm and 4 µm crater diameters, fractionation generally remains unrelated to NBO/T. However, the fractionation of Y and Zr shows some dependence on polymerisation (Fig. 4.42 E and F). Yttrium and Zr are more fractionated with decreasing polymerisation (increasing NBO/T). At NBO/T =0, Y is underrepresented by ~0 -10% using 6 µm and 4 µm crater diameters, whilst at NBO/T = ~0.5, Y is underrepresented by ~25% and ~45% at 6 µm and 4 µm crater diameters, respectively. However, using 4 µm crater diameters, Y is differently fractionated in three similarly polymerised melts of NBO/T = ~0. Additionally, the reliability of Zr and Y fractionation associated with polymerisation at <10 µm crater diameters is uncertain given the significant error at 6 µm and 4 µm crater diameters, respectively ~ 20% and ~30-50%. Concentrations of trace elements in the basaltic reference material, BCR-2G, (NBO/T = ~0.55) are frequently overestimated at 4 µm crater diameters (see Fig. 4.42 E, circled in red). This may indicate BCR-2G responds differently to element fractionation or may relate to compositional heterogeneity at smaller crater diameters.

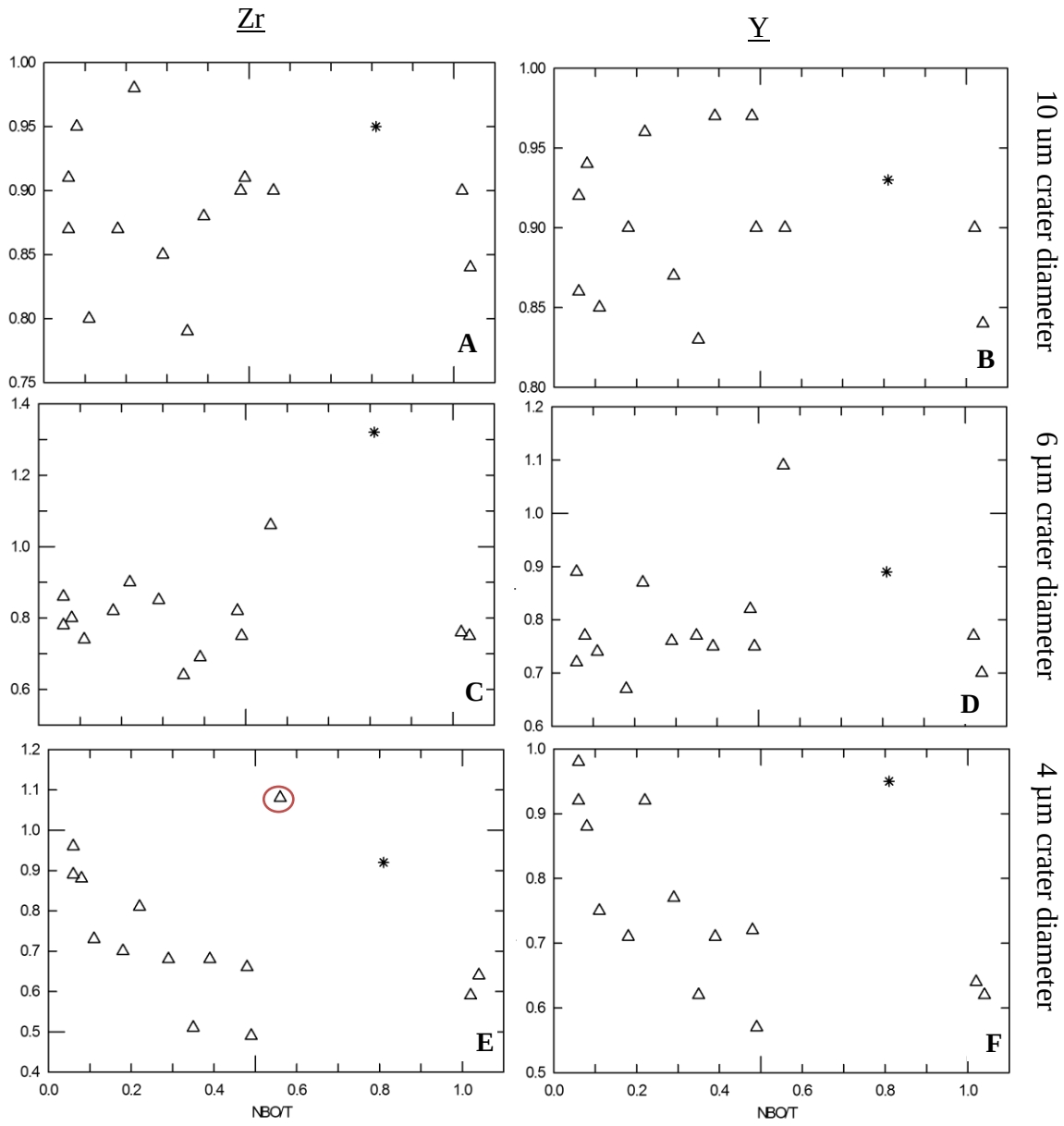

Fig. 4.42 F.I (calculated as concentration determined at *x* µm crater diameter/ concentration determined at 20 µm crater diameter) for Zr and Y measured from 10 µm (A and B), 6 µm (C and D) and 4 µm crater diameters in 15 samples and NIST 612 (*) against calculated NBO/T. All analyses are conducted under identical laser operating conditions, calibrated against 20 µm crater diameter acquisitions of NIST 612 with ^{29}Si as the internal standard. All analyses are fractionation corrected against the 20 µm crater diameter fractionation factor calculated by Pearce *et al.* (2011).

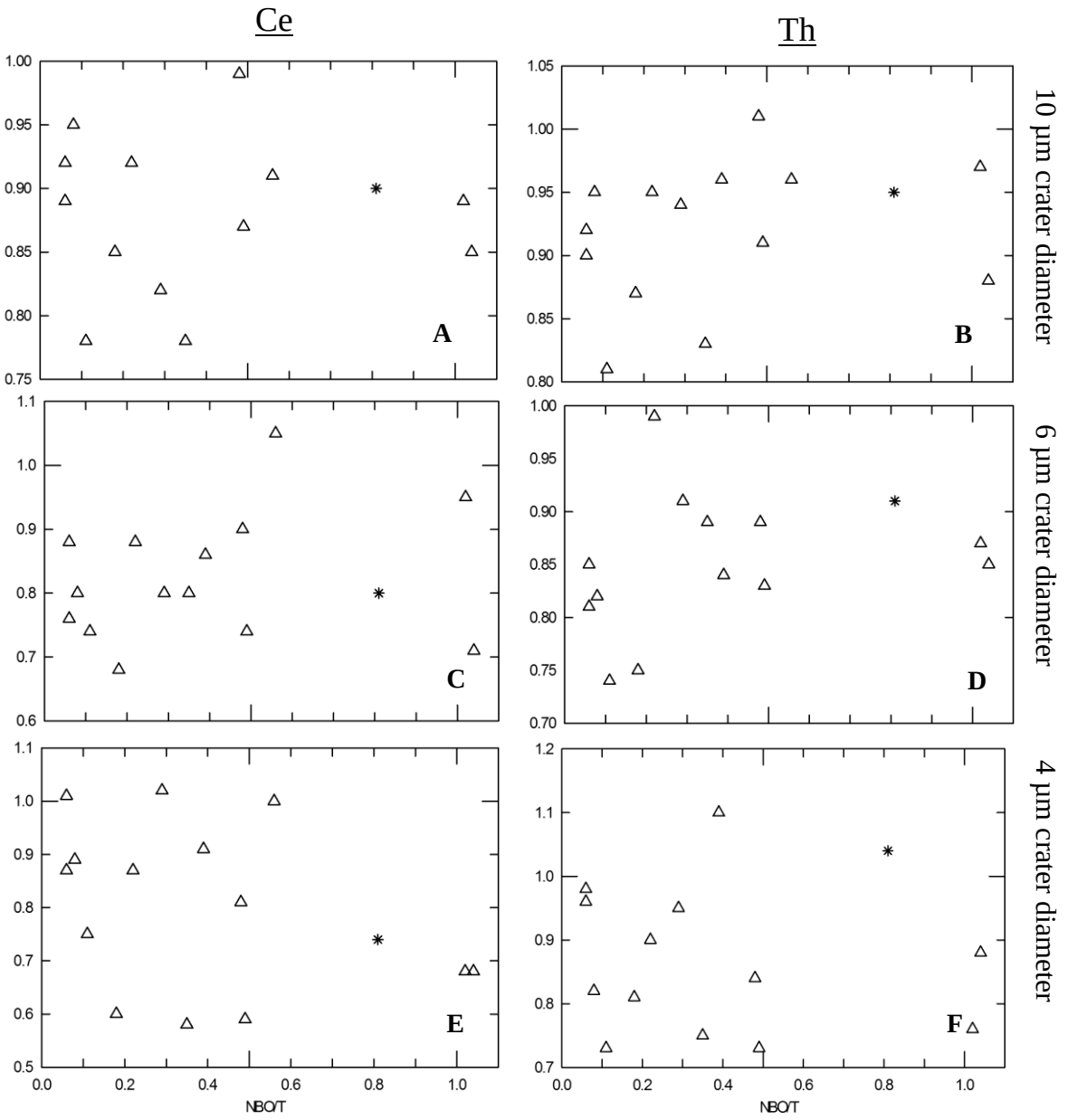

Fig. 4.43 F.I for Ce and Th measured from 10 µm (A and B), 6 µm (C and D) and 4 µm crater diameters in 15 samples and NIST 612 (*) against calculated NBO/T. All analyses conducted under identical laser operating conditions, calibrated against 20 µm crater diameter acquisitions of NIST 612 with ^{29}Si as the internal standard. All analyses fractionation corrected against the 20 µm crater diameter fractionation factor calculated by Pearce *et al.* (2011).

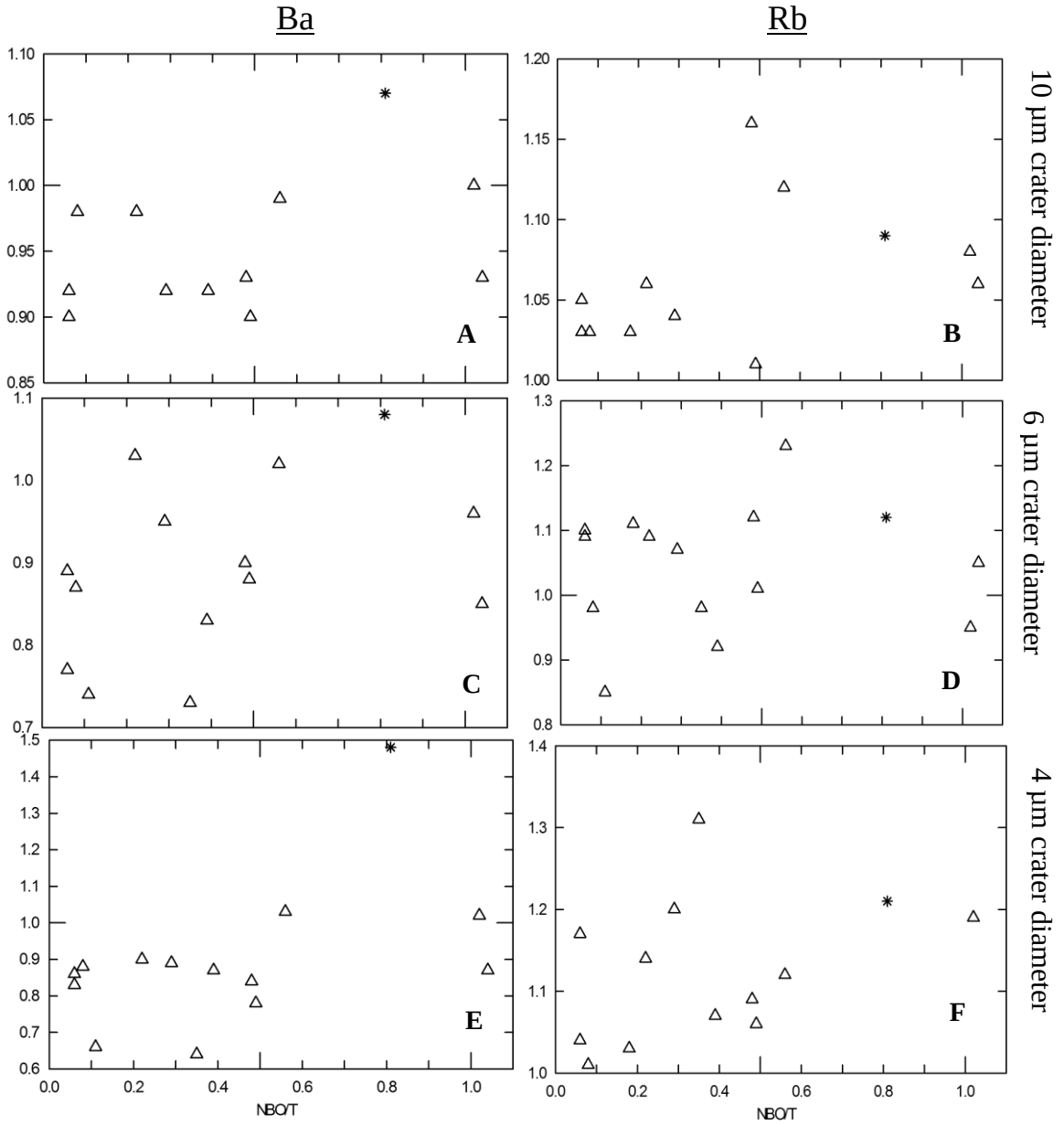

Fig. 4.44 F.I. for Ba and Rb measured from 10 µm (A and B), 6 µm (C and D) and 4 µm crater diameters in 15 samples and NIST 612 (*) against calculated NBO/T. All analyses conducted under identical laser operating conditions, calibrated against 20 µm crater diameter acquisitions of NIST 612 with ^{29}Si as the internal standard. All analyses fractionation corrected against the 20 µm crater diameter fractionation factor calculated by Pearce *et al.* (2011).

Finding no significant correlation between element fractionation and NBO/T, element fractionation of Zr and Rb related to viscosity, liquidus temperature and iron concentration is investigated below (Figs. 4.45 to 4.47). These factors are interrelated and are influenced by bulk composition. Viscosity and NBO/T both relate to silicate structure, in turn controlled by composition. Liquidus temperature is directly related to SiO_2 concentration and iron concentration is inversely proportional to SiO_2 concentration.

Zirconium and Rb fractionation using 10 µm crater diameters shows no correlation with viscosity, liquidus temperature or iron concentration. As seen previously, the fractionation of Zr and Rb at 6 µm and 4 µm crater diameters appears broadly related to viscosity, liquidus temperature and iron concentration, yet these analyses are subject to large ~<50 % errors. Zirconium appears most fractionated (~-50%) in basic samples of a low viscosity, high liquidus temperature and high iron concentration. Rubidium fractionation from 4 µm crater diameters broadly correlates only with viscosity, appearing to increase with decreasing viscosity. Rubidium is ~20% overepresented in samples of low viscosities and ~10% overestimated in samples of a ~10,000 Pascal seconds (Pa s) viscosity. This reflects the broad increase in element fraction with increasing NBO/T. However, a group of samples with similarly high viscosities fractionate Zr differently, ranging from ~30% to ~0% underepresented. This may suggest other factors determine element fractionation.

The fractionation of NIST 612 differs by ~5-10% when compared with samples of samples of a similar viscosity, liquidus temperature and iron concentration (e.g. Fig. 4.45 E), this may relate to the synthetic matrixof this reference material.

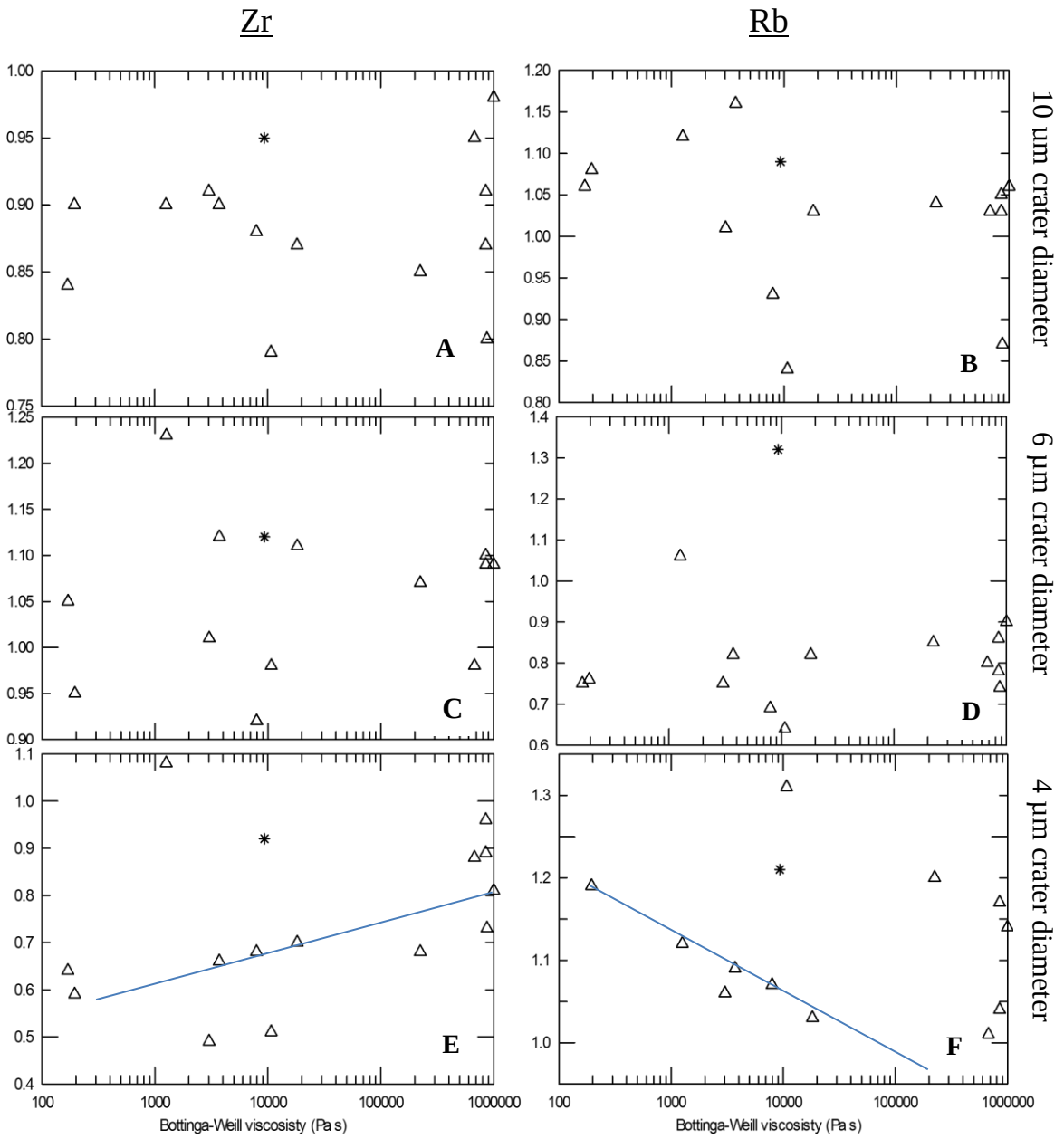

Fig. 4.45 F.I. for Zr and Rb measured from 10 µm (A and B), 6 µm (C and D) and 4 µm crater diameters in 15 samples and NIST 612 (*) against calculated Bottinga-Weill Viscosity (Pa s). All analyses fractionation corrected against the 20 µm crater diameter fractionation factor calculated by Pearce *et al.* (2011).

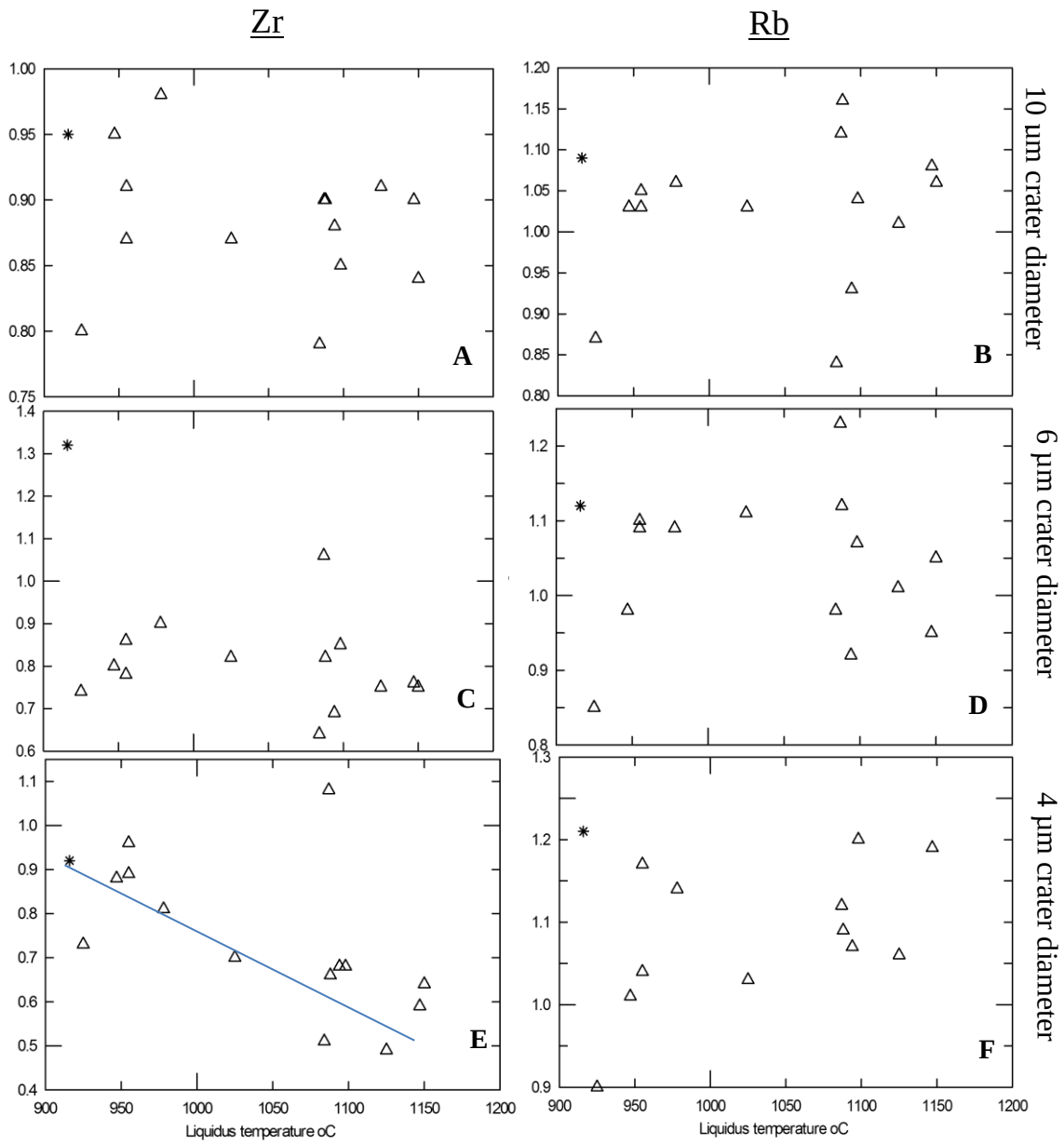

Fig. 4.46 F.I. for Zr and Rb measured from 10 µm (A and B), 6 µm (C and D) and 4 µm crater diameters in 15 samples and NIST 612 (*) against calculated liquidus temperature (^{o}C) All analyses fractionation corrected against the 20 µm crater diameter fractionation factor calculated by Pearce *et al.* (2011).

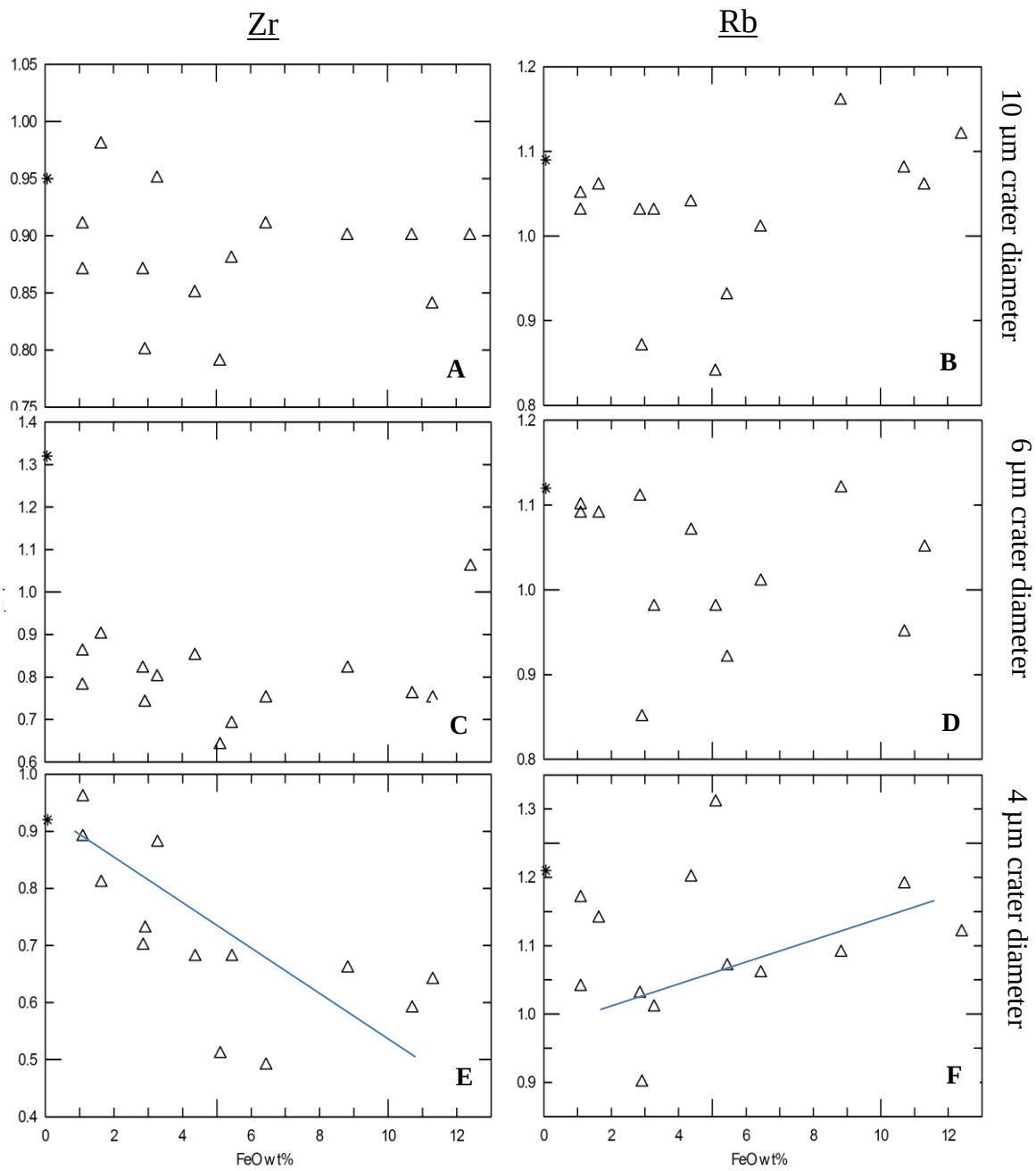

Fig. 4.47 F.I. for Zr and Rb measured from 10 µm (A and B), 6 µm (C and D) and 4 µm crater diameters in 15 samples and NIST 612 (*) against FeO wt%. All analyses fractionation corrected against the 20 µm crater diameter fractionation factor calculated by Pearce *et al.* (2011).

4.4.3 Discussion of Fractionation Associated with Composition

Several studies have investigated element fractionation associated with simple compositional parameters, such as sample transparency and colour associated with varying SiO_2 and FeO concentrations (Mank and Mason, 1999; Sylvester, 2008; Gaboardi and Humayan, 2009; Czas *et al.*, 2012). Mank and Mason (1999) and Gaboardi and Humayan (2009) generally found element fractionation to be more prevalent in transparent samples (containing lower FeOwt%). This study found no relationship between element fractionation and sample transparency and in some instances, basic samples with higher FeO concentrations appear more fractionated. Mank and Mason (1999) and Gaboardi and Humayan (2009) used longer laser wavelengths than this study (266 nm and 213 nm, respectively). The 193 nm laser utilised in this study couples more efficiently to transparent samples. Czas *et al.* (2012) found matrix effects between transparent and opaque silicate glasses to be reduced when using a 193 nm laser. However, Czas *et al.* (2012) used large crater diameters (> 75 µm), affected less by fractionation.

Few studies have investigated element fractionation and other compositional parameters. However, Pearce *et al.* (2011) found a clear relationship between melt polymerisation and element fractionation, with fractionation increasing with decreasing NBO/T (increasing melt polymerisation). This may be related to changing REE co-ordination within samples associated with changing composition, in turn altering a particular elements preference for the melt phase. Using an identical analytical set-up to Pearce *et al.* (2011), no systematic influence of polymerisation, viscosity, liquidus temperature and iron concentration on element fractionation was noted in this study. The HFSE were broadly more fractionated in more basic samples at 6 µm and 4 µm crater diameters, contrasting with the findings of Pearce *et al.* (2011). Prowatke and Klemme (2005) found partition coefficients for Zr, Hf and U and monovalent and divalent cations to be unaffected by composition, possibly explaining why the fractionation of Zr is not controlled systematically by composition in this study. However, Prowatke and Klemme (2005) cited the compositional dependence of REE partition coefficients, yet in this study Ce showed no compositionally related fractionation. Whilst Pearce *et al.* (2011) demonstrated a systematic relationship between element fractionation and polymerisation, this study tested a wider compositional range of samples over a longer time period, introducing factors such as sample heterogeneity and variable instrument operating conditions, which may mask any relationship between sample composition and element fractionation.

Chapter 5 Calculation of New Fractionation Factors

5.1 Calculation of Fractionation Factors

After investigating the influence of several parameters on element fractionation, it is apparent that only crater diameter controls fractionation systematically. Therefore only fractionation factors for crater diameter are calculated below.

Three fractionation factors (F.Fs) were calculated for to correct for the fractionation of each element when measured using 10 µm, 6 µm and 4 µm crater diameters. Fractionation indices (F.I.s concentration determined using 10 µm, 6 µm and 4 µm crater diameters / measured concentrations from 20 µm crater diameters) were calculated from the repeat analyses of 16 reference materials (NIST 610, NIST 612, BCR-2G, BHVO-2G, KL2-G2, StHs/680G, T1-G, ATHO-G) and tephra samples (UT1588, UT1440,UT2015, UT1285, UT1287, Chabbi and Newberry Obsidians and CF86) as presented in Chapter 4. Measured concentrations in each sample were calculated using the Pearce *et al.* (2011) F.F. New fractionation factors for each crater diameter were calculated by averaging the relevant 10 µm, 6 µm and 4 µm crater diameter F.I.s for the 16 samples.

Calculated fractionation factors for 26 trace elements can be seen in Table 5.10. To fractionation correct raw glass analyses they must first be divided by the 20 µm crater diameter F.F. from Pearce *et al.* (2011). Then element concentrations may be divided by the appropriate crater diameter fractionation factors calculated in this study.

5.2 Testing New Fractionation Factors

In Fig. 5.10 the calculated 10 µm, 6 µm and 4 µm crater diameter F.F.s are applied to the same suite of 16 samples from which they were calculated. Prior to fractionation correction using the F.F.s from this study, all analyses were calculated using the Pearce *et al.* (2011) 20 µm crater diameter F.F. Those elements omitted from Fig. 5.10 (e.g. the MREE-HREE at 4 µm crater diameters) fall below the limit of detection for that particular crater diameter, the overall average is plotted as a point of reference. Application of the F.F.s from this study brings concentrations from all crater diameters on average closer to measured concentrations from 20 µm crater diameters (see Fig. 5.10, a ratio of 1 equivalent to 20 µm crater diameter concentrations). From 6 µm crater diameters, nine petrogenically

significant trace elements (Rb, Y, Zr, Nb, Ba, La, Ce, Pr and Nd) may be determined to within ±10% of their measured concentrations from 20 µm crater diameters.

	10 µm crater diameter			6 µm crater diameter			4 µm crater diameter		
	Fractionation factor	SD	RSD%	**Fractionation factor**	SD	RSD%	**Fractionation factor**	SD	RSD%
Rb	**1.03**	0.08	7.98	**1.05**	0.09	8.97	**1.08**	0.19	18.07
Sr	**0.90**	0.09	10.13	**0.84**	0.45	53.36	**0.70**	0.45	64.81
Y	**0.90**	0.05	5.08	**0.81**	0.11	13.10	**0.80**	0.16	20.21
Zr	**0.89**	0.05	6.18	**0.84**	0.16	18.97	**0.76**	0.17	22.12
Nb	**0.95**	0.05	5.70	**1.01**	0.18	18.04	**1.14**	0.28	24.93
Cs	**0.89**	0.33	37.37	**1.13**	1.02	90.41	**0.20**	3.20	1598.52
Ba	**0.99**	0.27	27.30	**1.04**	0.59	56.55	**0.79**	0.47	60.13
La	**0.91**	0.05	5.60	**0.89**	0.14	15.46	**0.83**	0.13	15.83
Ce	**0.92**	0.05	5.79	**0.88**	0.10	10.97	**0.91**	0.16	17.59
Pr	**0.92**	0.07	7.53	**0.91**	0.21	22.78	**0.89**	0.19	21.07
Nd	**0.93**	0.07	7.36	**0.90**	0.11	11.72	**0.92**	0.15	16.31
Sm	**0.95**	0.09	9.77	**0.90**	0.27	30.38	**0.86**	0.28	32.98
Eu	**0.97**	0.14	14.01	**1.17**	1.12	95.78	**0.77**	1.40	180.58
Gd	**0.86**	0.21	23.77	**0.90**	0.41	45.19	**0.77**	0.67	87.56
Tb	**0.94**	0.11	11.97	**0.85**	0.21	24.91	**0.64**	0.56	86.78
Dy	**0.92**	0.09	10.08	**0.89**	0.12	13.72	**0.84**	0.33	39.17
Ho	**0.94**	0.09	9.55	**0.91**	0.24	26.31	**0.96**	0.40	41.75
Er	**0.95**	0.11	11.61	**0.91**	0.12	13.48	**0.76**	0.31	41.19
Tm	**0.91**	0.11	12.46	**0.80**	0.26	32.84	**0.82**	0.63	76.74
Yb	**0.94**	0.09	9.13	**0.84**	0.17	19.97	**0.79**	0.40	50.01
Lu	**1.01**	0.15	14.45	**0.87**	0.19	22.12	**1.75**	4.28	244.36
Hf	**0.94**	0.09	9.49	**0.92**	0.18	19.87	**0.74**	0.25	33.41
Ta	**0.94**	0.09	9.70	**0.91**	0.22	24.71	**0.82**	0.63	76.36
Pb	**0.94**	0.10	11.00	**0.94**	0.13	14.34	**1.05**	0.37	34.82
Th	**0.89**	0.08	8.91	**0.83**	0.10	11.56	**0.80**	0.15	18.72
U	**0.98**	0.08	8.33	**0.97**	0.11	10.88	**1.12**	0.16	14.26

Table 5.10 Fractionation factors calculated by averaging F.I. for a particular crater diameter (average concentration determined at *x* µm crater diameters / average concentration determined at 20 µm crater diameter) and for 15 MPI-DING and USGS reference materials and tephra samples. Analyses were conducted at 20 µm 10 µm, 6 µm and 4 µm crater diameters, with NIST 612 as the calibration standard and ^{29}Si as the internal standard. Analyses were corrected against the 20 µm crater diameter F.F. from Pearce *et al.* (2011), prior to calculation of the new F.F.s

In Figs. 5.12-5.14 new fractionation factors are applied to Minoan (~75 wt% SiO_2) and UT2252 (~45wt% SiO_2) glass analyses from Pearce *et al.* (2011). Figures 5.12-5.14 (A & B) show raw Zr, Y, La and Rb concentrations without fractionation correction. In Figs. 5.12-5.14 (C & D) Zr, Y, La and Rb concentrations in Minoan and UT2252 glass are fractionation corrected only using the 20 µm crater diameter Pearce *et al.* (2011) F.F. Figures 5.12-5.14 (E & F) show the same analyses calculated using the Pearce *et al.* (2011) 20 µm crater diameter F.F., then corrected against the respective crater diameter F.F.s calculated in this study. With new F.F.s applied, measured concentrations of Rb, Zr and La at 10 µm, 6 µm and 4 µm crater diameters are brought closer to concentrations obtained using 20 µm crater diameters. With no fractionation correction, concentrations of Zr and Y measured in Minoan and UT2252 glass shards using 6 µm crater diameters are represented at ~60-70% of measured concentrations using 20 µm crater diameters. With F.Fs. from both Pearce *et al.* (2011) and this study applied, Zr and Y concentrations in Minoan and UT2252 glass from 6 µm crater diameters are measured at 90% of concentrations from 20 µm crater diameters. In contrast, the fractionation of Rb in Minoan glass shards does not appear to be reduced through application of the fractionation factors calculated in this study.

Whilst the application of the F.F.s presented in Table 5.10 appears to improve the accuracy of 10 µm, 6 µm and 4 µm crater diameter analyses, Fig. 5.10 demonstrates that different compositions remain differently fractionated. After application of the F.F.s calculated in this study to concentrations from 10 µm crater diameters, Zr and Y are ~15% more underestimated in basic samples than intermediate and acidic compositions. Whilst this is not as significant as the fractionation associated with crater diameter, this differential fractionation is not systematic and thus cannot be corrected for at this stage.

In the following section, the fractionation factors calculated above will be applied to tephra from Ulleungdo, Korea.

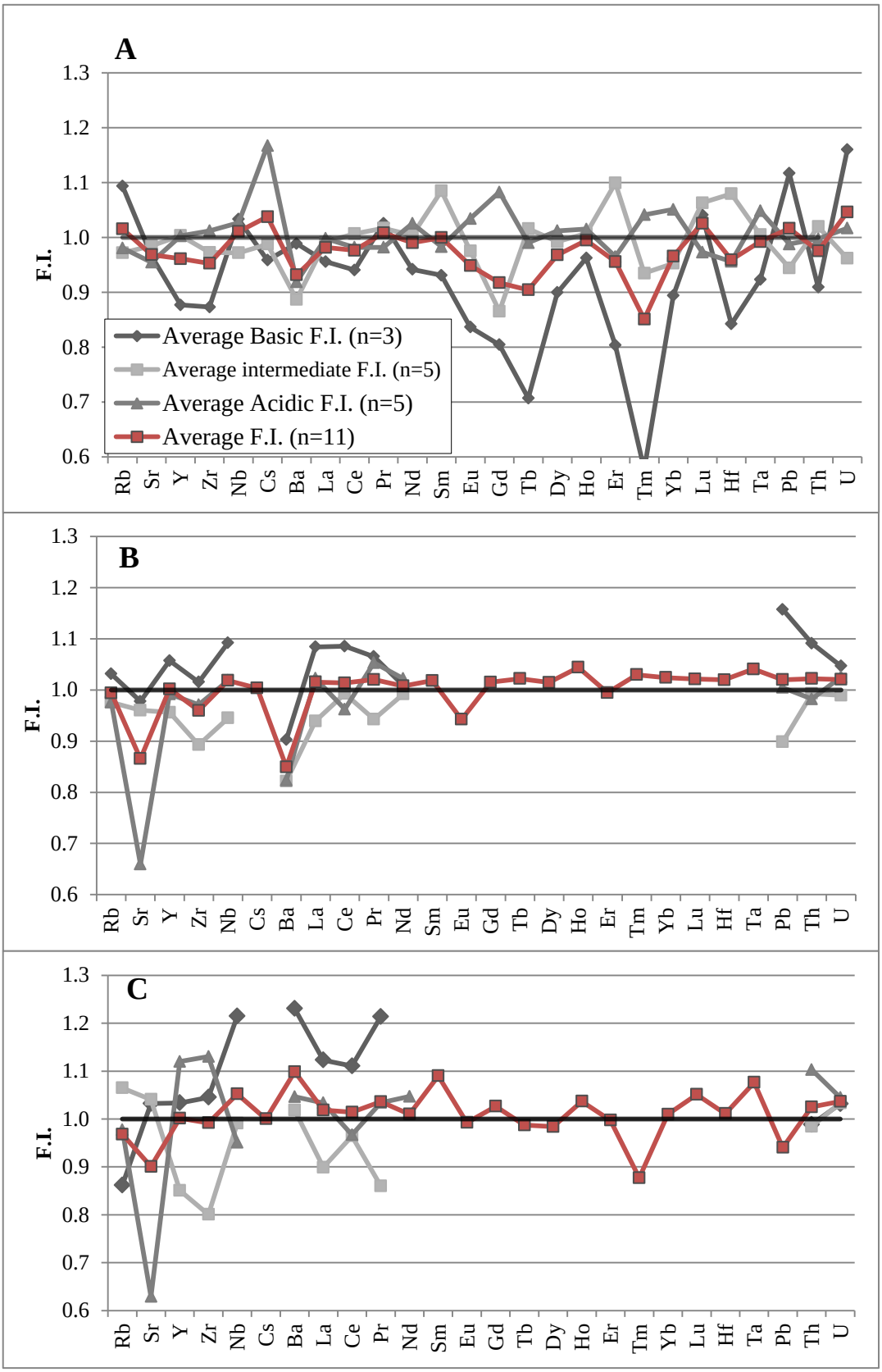

Fig. 5.10 Fractionation index for trace elements in basic (KL2-G, BHVO-2G, BCR-2G), intermediate (UT1588, UT1440, UT2015, T1-G, St-Hs80G) and acidic (ATHO-G, UT1285, UT1287, Chabbi Obsidian, Newberry Obsidian) samples and at A) 10 µm, B) 6 µm and C) 4 µm crater diameters. Analyses are calibrated against NIST 612 20 µm crater diameter spectra, with ^{29}Si as the internal standard. Analyses corrected against fractionation factors for 10 µm, 6 µm 4 µm crater diameters calculated in this study.

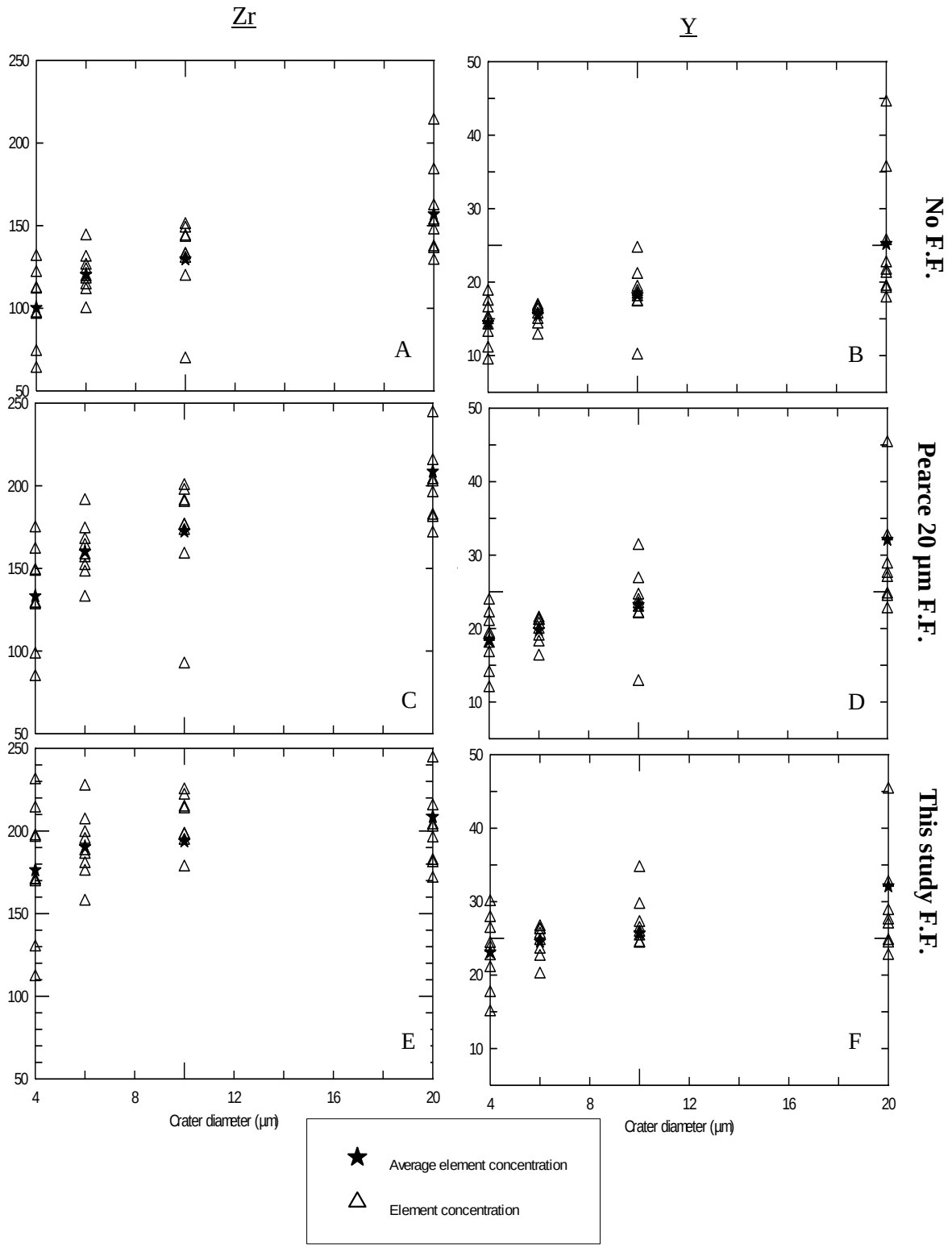

Fig. 5.11. Concentrations of Zr and Y (ppm) in Minoan glass shard analyses from Pearce *et al.* (2011) at 20 µm, 10 µm, 6 µm and 4 µm crater diameters, A) and B) no fractionation correction, C) and D) Zr and Y concentrations with only Pearce *et al.* (2011) 20 µm crater diameter fractionation factor, E) and F) Zr and Y concentrations with Pearce *et al.* (2011) 20 µm fractionation factor and 10 µm, 6 µm, 4 µm crater diameter fractionation factors calculated in this study applied.

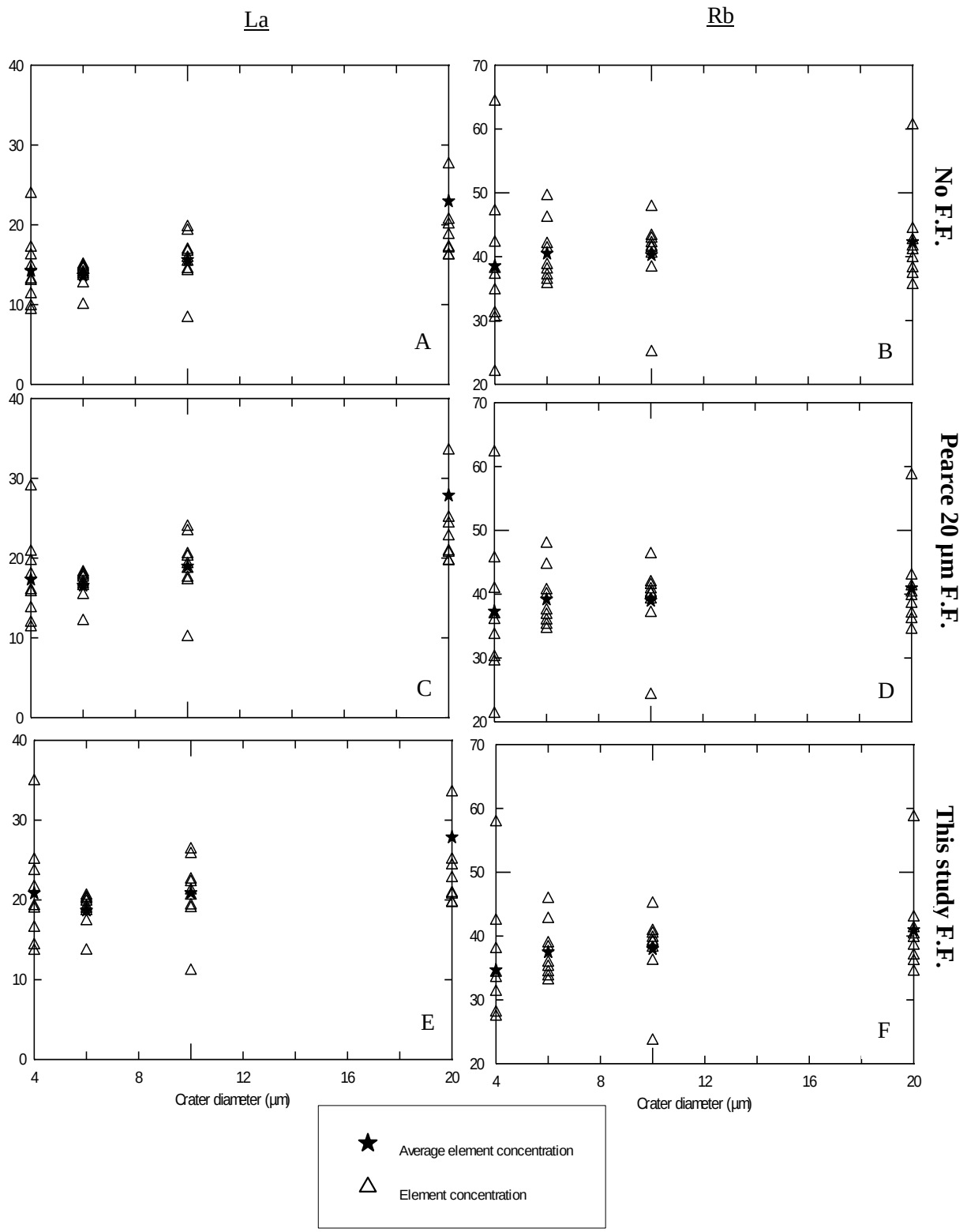

Fig. 5.12. La and Rb concentrations (ppm) in Minoan glass shard analyses from Pearce *et al.* (2011) at 20 µm, 10 µm, 6 µm and 4 µm crater diameters,. A) and B) no fractionation correction, C) and D) only Pearce *et al.* (2011) 20 µm crater diameter fractionation factor, E) and F) Pearce *et al.* (2011) 20 µm fractionation factor and 10 µm, 6 µm, 4 µm crater diameter fractionation factors calculated in this study applied.

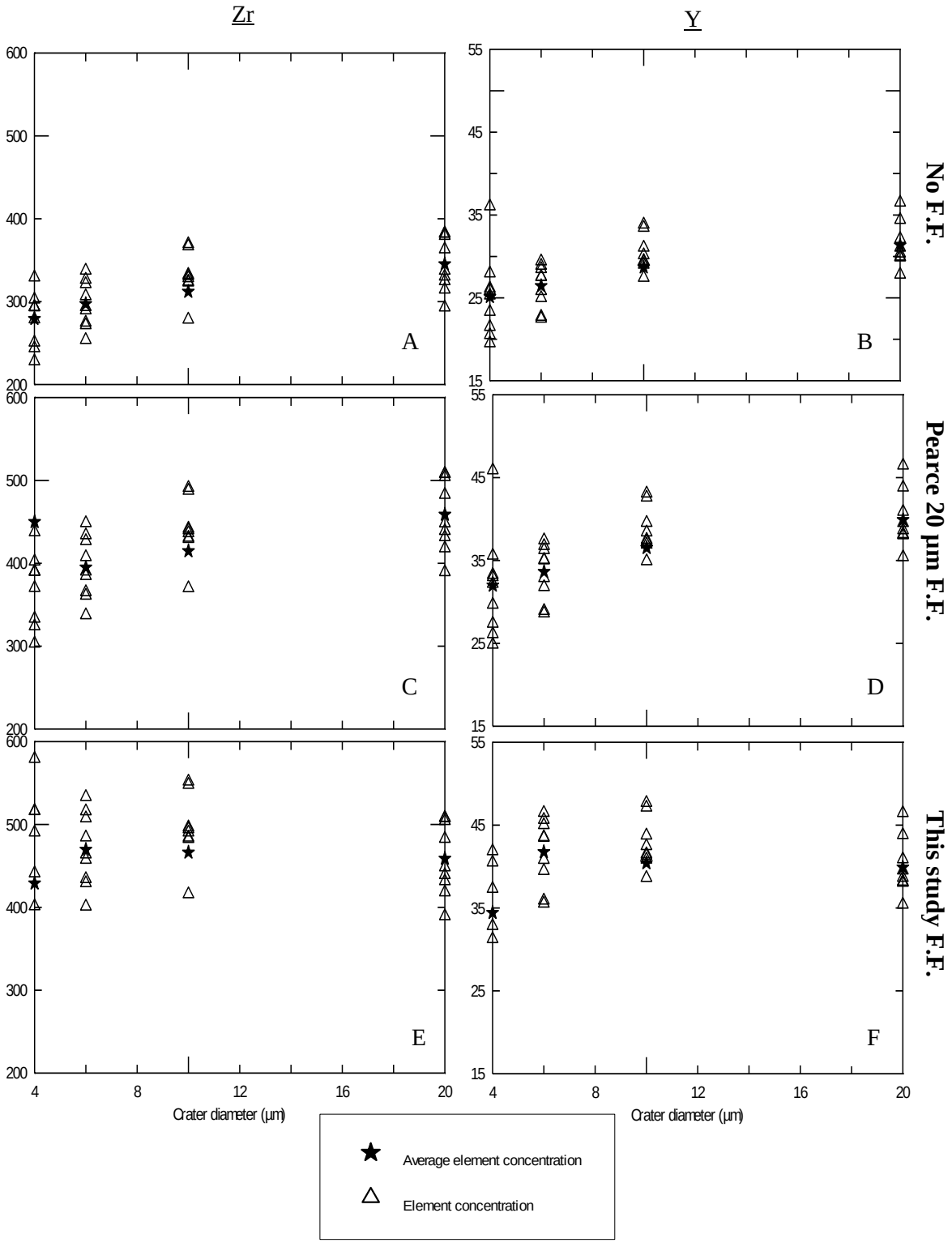

Fig. 5.13Zr and Y concentrations (ppm) in glass shard analyses of UT2552 (~45wt % SiO_2) from Pearce *et al.* (2011) at 20 µm, 10 µm, 6 µm and 4 µm crater diameters, A) and B) no fractionation correction, C) and D) only Pearce *et al.* (2011) 20 µm crater diameter fractionation factor, E) and F) Pearce *et al.* (2011) 20 µm fractionation factor and 10 µm, 6 µm, 4 µm crater diameter fractionation factors calculated in this study applied.

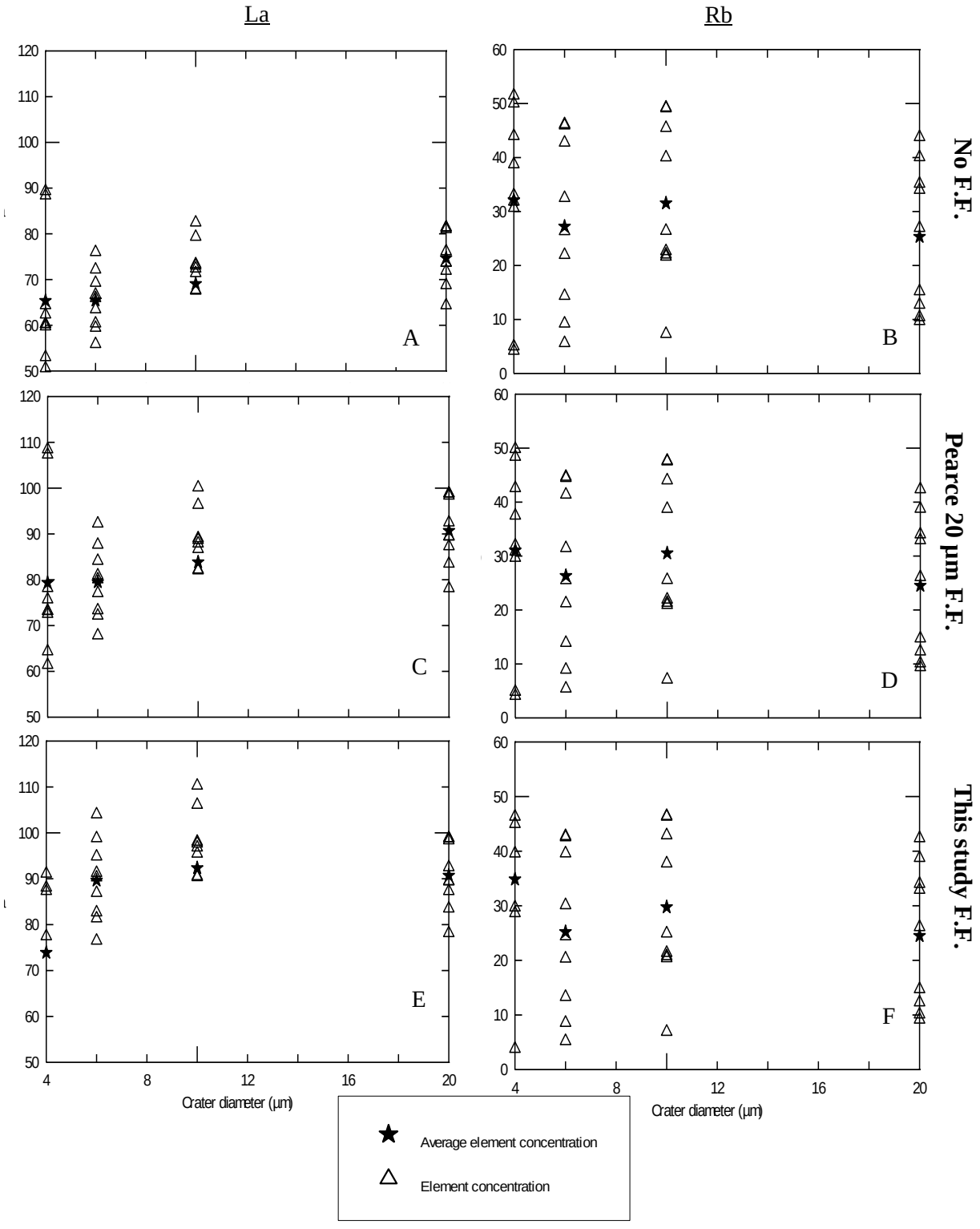

Fig. 5.14 La and Rb concentrations (ppm) in glass shard analyses of UT2552 (~45wt % SiO_2) from Pearce *et al.* (2011) at 20 µm, 10 µm, 6 µm and 4 µm crater diameters A) and B) with no fractionation correction, C) and D) with only Pearce *et al.* (2011) 20 µm crater diameter fractionation factor, E) and F with Pearce *et al.* (2011) 20 µm fractionation factor and 10 µm, 6 µm, 4 µm crater diameter fractionation factors calculated in this study applied.

Chapter 6 Characterisation of Ulleungdo Tephra

In this chapter fractionation factors calculated in this study will be applied to the analysis of proximal tephra deposits from Ulleungdo, Korea.

Machida *et al.* (1984) described seven Ulleungdo pyroclastic units younging from U7 to U1, some of which are dispersed throughout the Sea of Japan (Smith *et al.* 2011a). Details of the samples analysed in this study can be seen in Fig. 6.11.

Field based correlations of tephra deposits to units defined by Machida *et al.* (1984) were established by Dr Victoria Smith (RLAHA, Oxford). A stratigraphic column (Fig. 6.11) gives the relative ages of tephra deposits analysed in this study. Three samples were collected from site K1 on Ulleungdo; sample K1-A1 was collected from a pumice fall deposit, correlated to U4. Sample K1-B1 was collected from an overlying ignimbrite deposit, possibly corresponding to U3. Sample K1-C1 was collected from an overlying ash fall deposit, possibly correlating to U2.

Two samples were collected from Site K7. Sample K7-B2 was taken from a vitric ash deposit, possibly correlating to the Japanese AT tephra. Sample K7-J1 was collected from U3, comprising an ash and pumice deposit. All these Ulleungdo units are separated by palaeosols.

Glass shards from Ulleungdo proximal deposits are typically pumiceous with thin bubble walls. However, K7-B2 contains glass shards of a cuspate nature. Feldspar microcrysts are also common in the Ulleungdo samples.

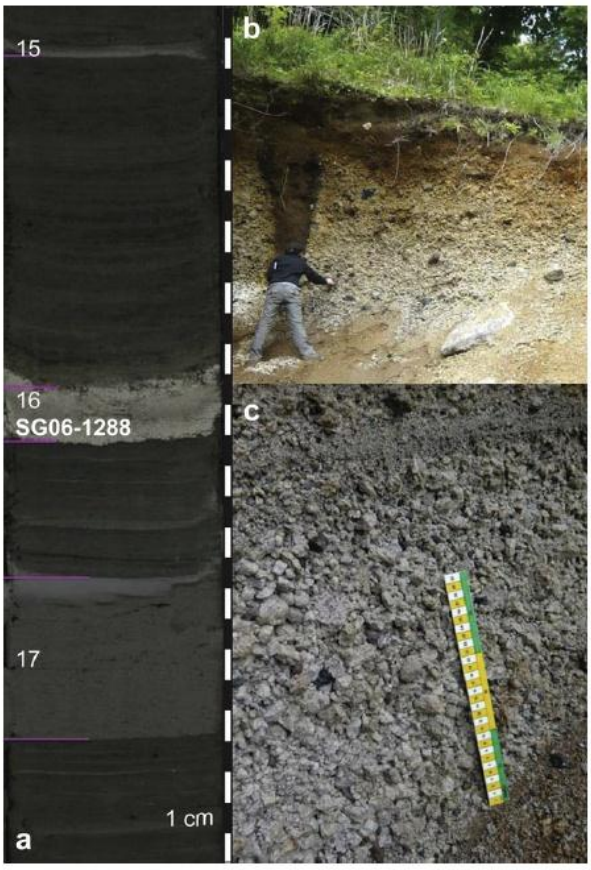

Fig. 6.10 A) SG06-1288 tephra in the Suigetsu core, B) and C) U4 outcropping on Ulleungdo, Korea (from Smith *et al.*, 2011a).

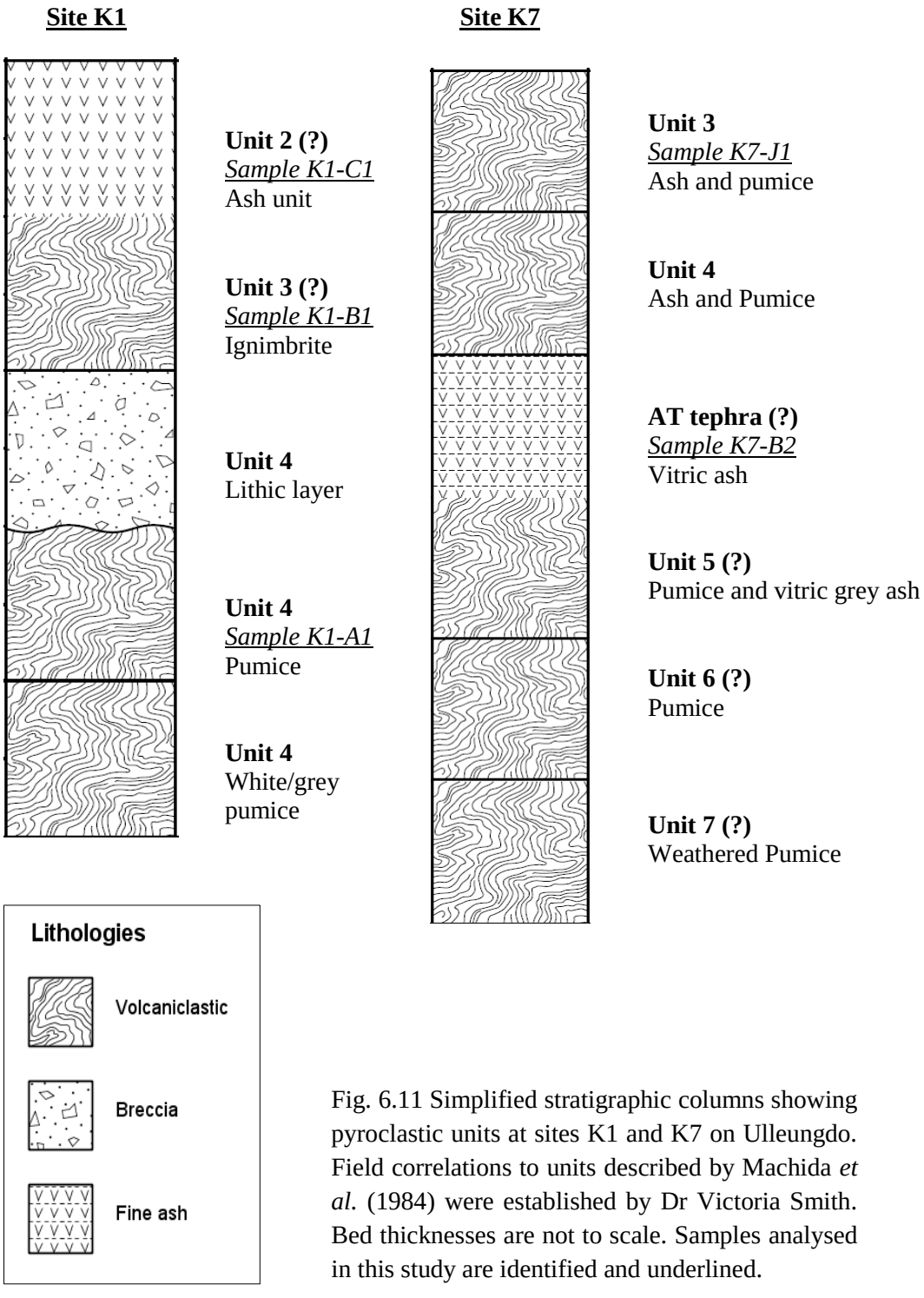

Fig. 6.11 Simplified stratigraphic columns showing pyroclastic units at sites K1 and K7 on Ulleungdo. Field correlations to units described by Machida *et al.* (1984) were established by Dr Victoria Smith. Bed thicknesses are not to scale. Samples analysed in this study are identified and underlined.

6.1 Major Element Glass Chemistry and Comparison with other Studies

Sample	**K1-B1 (n=18)**	*SD*	**K1-C1 (n=13)**	*SD*	**K7-B2 (n= 23)**	*SD*	**K7-J1 (n=7)**	*SD*	**K1-A1 (n=8)**	*SD*
Unit	**U3**		**U2**		**AT**		**U3**		**U4**	
SiO_2	**59.68**	*0.55*	**60.73**	*0.45*	**77.70**	*0.50*	**59.59**	*0.67*	**59.89**	*1.21*
TiO_2	**0.55**	*0.08*	**0.45**	*0.08*	**0.14**	*0.03*	**0.28**	*0.11*	**0.45**	*0.16*
Al_2O_3	**19.40**	*0.21*	**19.57**	*0.15*	**12.47**	*0.14*	**20.76**	*0.96*	**19.69**	*0.72*
FeOT	**3.66**	*0.17*	**3.08**	*0.27*	**1.33**	*0.12*	**2.82**	*0.54*	**3.28**	*0.14*
MnO	**0.15**	*0.04*	**0.18**	*0.04*	**0.05**	*0.03*	**0.20**	*0.03*	**0.20**	*0.06*
MgO	**0.62**	*0.05*	**0.24**	*0.06*	**0.13**	*0.02*	**0.11**	*0.11*	**0.25**	*0.11*
CaO	**2.23**	*0.12*	**1.49**	*0.12*	**1.12**	*0.08*	**1.11**	*0.22*	**1.58**	*0.33*
Na_2O	**6.18**	*0.71*	**6.94**	*0.27*	**3.61**	*0.52*	**8.36**	*1.19*	**7.34**	*0.98*
K_2O	**7.06**	*0.15*	**6.95**	*0.16*	**3.32**	*0.15*	**6.25**	*0.47*	**6.88**	*0.21*
P_2O_5	**0.15**	*0.02*	**0.08**	*0.02*	**0.02**	*0.02*	**0.04**	*0.04*	**0.09**	*0.05*
H_2O*	**4.08**	*2.10*	**3.52**	*2.21*	**5.03**	*0.95*	**3.59**	*2.26*	**6.15**	*2.38*

Table 6.10 Anhydrous average major element (wt%) glass compositions for Ulleungdo units. Standard deviation given in italics, H_2O* = water by difference.

Normalised major element glass chemistry of the Ulleungdo proximal tephra deposits is presented as averages in Table 6.10. Shard specific major element compositions are plotted in Figs. 6.12 to 6.14. The Ulleungdo proximal deposits, K7-J1, K1-A1, K1-C1 and K1-B1, (U3, U4, U2 and U3, respectively) are typically phonolitic, containing ~60wt% SiO_2 and > ~13wt% $Na_2O + K_2O$ (Fig. 6.12 A). Generally, seperate Ulleungdo proximal units share a similar major element composition; containing ~0.1-0.4wt% MgO, ~19-20 wt% Al_2O_3, ~6-8wt% Na_2O and ~2.5-3.5wt% FeO. The major element chemistry of Ulleungdo samples compares well with that described by (Shiihrara *et al.*, 2011; Smith *et al.*, submitted) (Figs. 6.12 B and 6.13 A). The Ulleungdo proximal units may have evolved from trachytic compositions through extraction of alkali feldspar in the region Or_{25-40} (see Fig. 6.12 A; Sorenson, 1974).

However, a duplicate sample from U3, K7-J1, is chemically distinct from other Ulleungdo units. K7-J1 glass contains lower SiO_2 (~59wt%), higher Na_2O (~8-10wt%), lower FeO (~2-3wt%) and lower MgO (~0.0-0.1 MgOwt%) and exhibits a broadly linear compositional range (Fig. 6.13 B) when compared with K1-A1, K1-B1 and K1-C1. The distinct composition of K7-J1 may indicate this sample is more compositionally evolved, with the continued removal of feldspar and movement of the melt further towards the

nepheline cotectic causing the residual melt to become depleted in SiO_2 and enriched in Na_2O relative to glass from other Ulleungdo units. Glass from K7-J1 is also depleted in FeO and MgO relative to glass from other Ulleungdo units, possibly indicating the removal of Fe-Ti oxide and pyroxene phases during the magmatic evolution of this sample (Wilson, 1989). Shiihara *et al.* (2011) demonstrate that glass from U2 and U3 is compositionally bimodal, containing two glass populations of slightly different Al_2O_3 and FeO concentrations (Fig. 6.13 A).

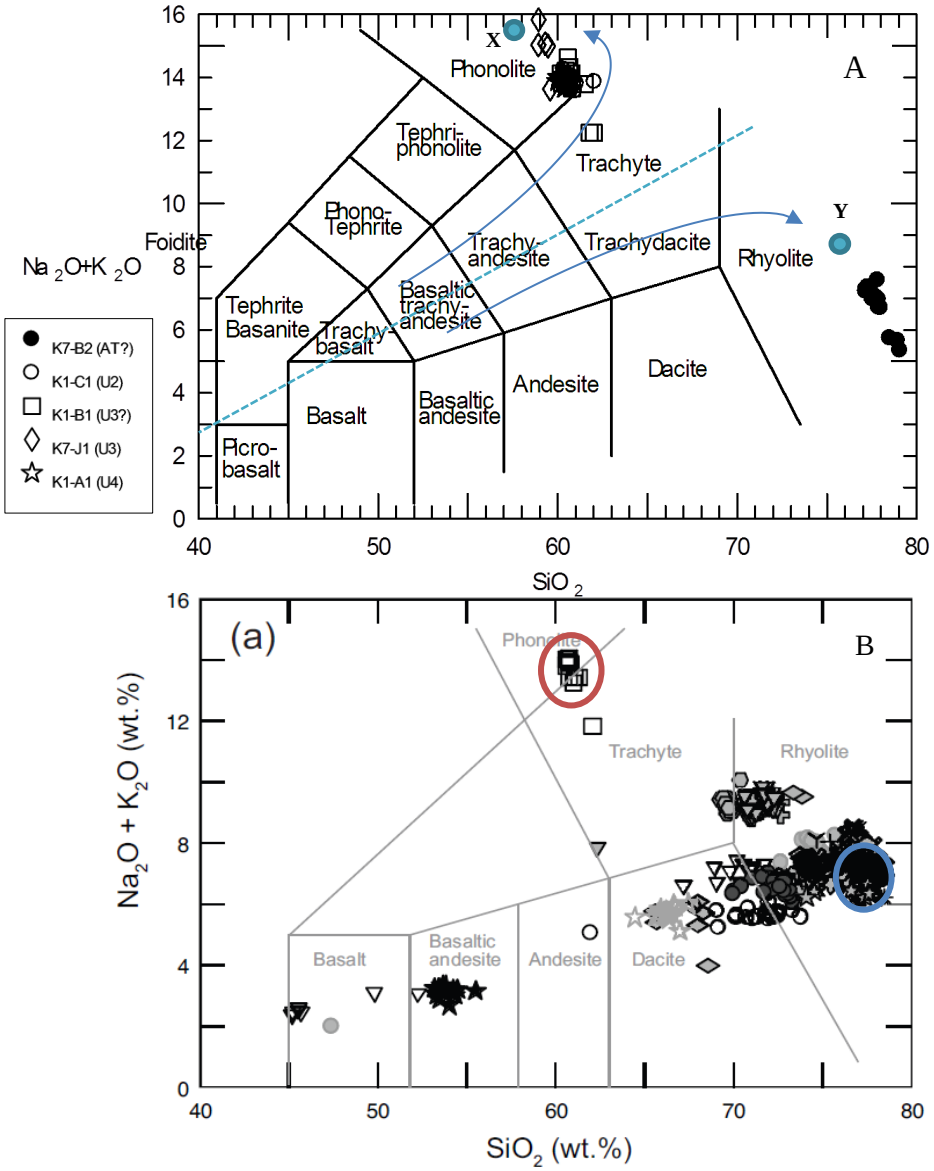

Fig. 6.12 A) TAS plot of anhydrous major element chemistry of Ulleungdo pyroclastic units from this study. Blue dashed line represents the albite-orthoclase thermal barrier, temperature contours decrease away from this plane (from Sorenson, 1974). Arrows diverging away from trachytic compositions indicate paths towards silica under and oversaturated cotectics, shown as X and Y, representing feldspar-nepheline and feldspar-quartz cotectics, respectively (Sorenson, 1974). B) TAS plot of anhydrous major element of tephra retrieved from the Suigetsu SG06 core, (plot and analyses from Smith *et al.*, submitted). Many Japanese tephra layers within SG06 are rhyolitc; Ulleungdo U4 glass chemistry is highlighted in red and the AT glass chemistry is highlighted in blue for comparison with this study.

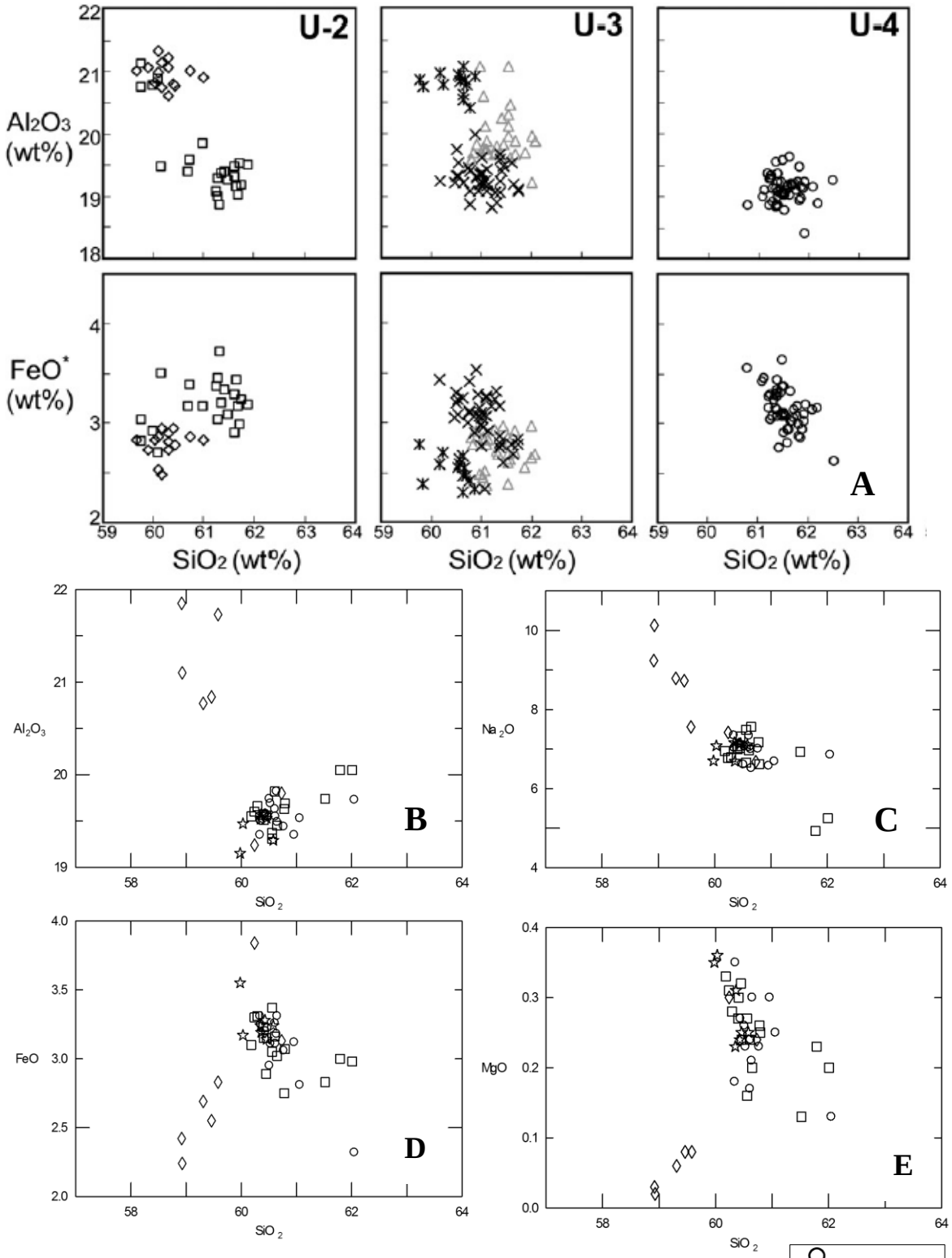

Fig. 6.13 A) Al_2O_3 and FeO vs. SiO_2 for Ulleungdo units 2, 3 and 4 (from Shiihara *et al.* 2011), note the bimodal glass populations for U2 and 3. B) Al_2O_3 C) Na_2O D) FeO E) MgO all vs. SiO_2 for a duplicate sample from U3 and samples from U2 and U4, note the more evolved nature of K7-J1, contrasting with the composition of other Ulleungdo units.

Glass analyses of K7-J1 in this study broadly correspond to compositional populations containing higher Al_2O_3 and lower FeO and SiO_2 in glass U2 and U3 from Shiihara *et al.* (2011).

One Ulleungdo tephra deposit is distinctly rhyolitic (K7-B2), containing ~78 wt% SiO_2, ~7 wt% $Na_2O + K_2O$ and lower concentrations of FeO, MgO and CaO when compared with other Ulleungdo units. K7-B2 glass evolved differently from that of the Ulleungdo samples, as the K7-B2 melt diverged from trachytic compositions towards the silica oversaturated cotectic (see Fig. 6.12 A), agreeing with the correlation of this unit of the AT tephra in the field. In addition, K7-B2 is more homogeneous when compared with the Ulleungdo samples, exhibiting a narrower range of K_2O (3-4wt %), CaO (1.1-1.2wt%) and MgO (0.1-0.2wt%). This may suggest glass from K7-B2 evolved from a magma chamber tapping a differing compositional range.

Japanese volcanic products are typically of a rhyolitic nature, containing <10wt% $K_2O + Na_2O$, contrasting with the alkaline nature of Ulleungdo tephra (Machida, 2002; Park *et al.*, 2007; Smith *et al.*, 2011a; Smith *et al.*, submitted) (Fig. 6.12 B). The Japanese Aira-Tanzawa (AT) and the Akahoya (K-Ah) tephra deposits, originating from the south Kyushu calderas Aira and Kikai, respectively, are found across the Sea of Japan and outcrop on Ulleungdo, (Machida *et al.*, 1984; Smith *et al.*, submitted). A precise date of 30.009 ± 0.189 $SG06_{2012}$ ka BP (2 σ) has been determined for the AT eruption and 7.165-7.303 cal. ka BP (95.4% probability) for the K-Ah (Smith *et al.*, submitted), using the new radiocarbon data and varve chronology from Lake Suigetsu (Staff *et al.*, 2011; Bronk Ramsey *et al.*, 2012). Unit 4, outcropping above the deposit from which K7-B2 was collected, yields an age of 10.0 ± 0.3 ka (1σ) (Smith *et al.*, 2011a). Thus, it is stratigraphically possible that K7-B2 corresponds to the AT tephra. The major element glass chemistry of K7-B2 is compared with the composition of tephra layers within the Suigetsu SG06 from Smith *et al.* (submitted) in Fig. 6.14 A) to D). Glass in K7-B2 matches the composition of many Japanese tephra layers within the Suigetsu core (see Fig 6.12 B & 6.12 E). The major element composition of K7-B2 broadly overlaps that of the AT tephra. However, there are some compositional differences; K7-B2 typically contains ~0.5wt% lower SiO_2 and ~0.5wt% higher Na_2O and CaO concentrations than AT proximal glass. K7-B2 contains two compositional groups, with three glass shards containing ~2wt% higher SiO_2 and ~1wt% higher Na_2O, this compositional heterogeneity is not shown by the AT proximal samples.

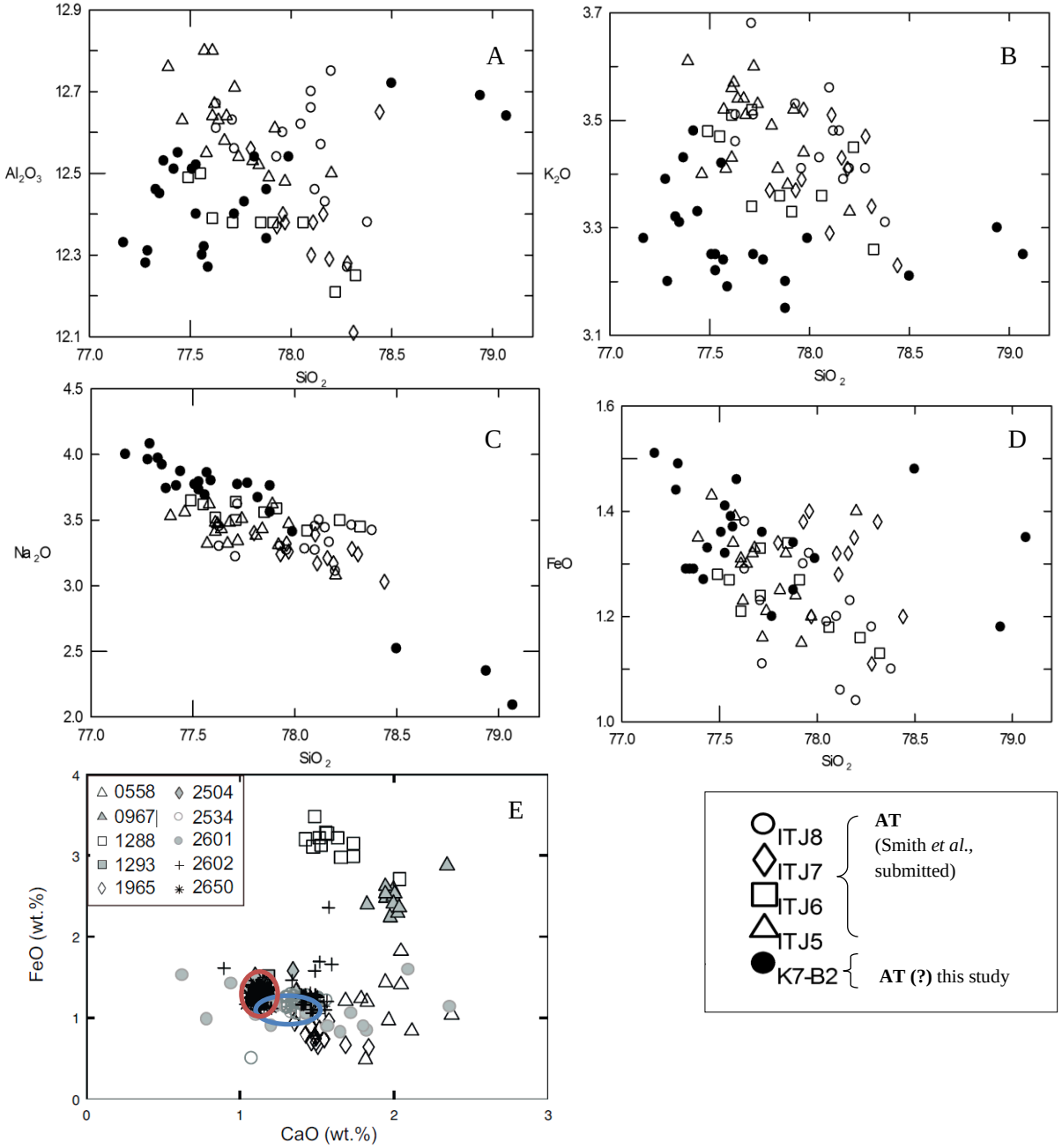

Fig. 6.14 AT proximal glass composition (samples ITJ8, ITJ7, ITJ6 and ITJ5, from Smith *et al.*, submitted) compared with K7-B2 glass composition. SiO_2wt% vs., A) Al_2O_3wt%, B) K_2Owt%, C) Na_2Owt%, D) FeOwt%.

E) CaOwt% vs. FeOwt% plot for tephra in the SG06 core, from Smith *et al.* (submitted). Numbers in legend refer to tephra depth within core (0967 = K-Ah tephra, 1288 = U-Oki, 2650 =AT).The glass composition of K7-B2 is overlain in blue, the AT tephra is ringed in red. Note how K7-B2 broadly corresponds to the AT (*), yet contains higher CaOwt%.

6.2 Trace Element Glass Chemistry and Comparison with other Studies

Machida *et al.* (1984) and Smith *et al.* (2011a) cited the similar major element composition of the Ulleungdo pyroclastic units. The trace element composition of Ulleungdo deposits is poorly studied (Park *et al.* 2007) and trace element data may allow their distinction.

Sample	**K1-B1 (U3)**		**K1-C1 (U2)**		**K7-B2 (AT?)**		**K7-J1 (U3)**		**K1-A1 (U4)**	
	(n=25)	*SD*	(n=21)	*SD*	(n=45)	*SD*	(n=7)	*SD*	(n=14)	*SD*
Rb	**167**	*12.66*	**160**	*15.21*	**131**	*16.24*	**205**	*69.81*	**168**	*10.69*
Sr	**78.1**	*39.98*	**61.1**	*19.72*	**120**	*19.82*	**84.1**	*75.72*	**79.3**	*46.97*
Y	**38.6**	*7.94*	**37.1**	*5.72*	**40.7**	*8.16*	**45.5**	*5.75*	**34.3**	*4.64*
Zr	**991**	*193.99*	**934**	*115.89*	**191**	*31.69*	**2090**	*271.97*	**937**	*76.41*
Nb	**209**	*30.79*	**199**	*23.49*	**12.3**	*2.74*	**376**	*54.64*	**228**	*14.49*
Cs	**2.19**	*0.94*	**1.82**	*0.50*	**9.71**	*1.38*	**3.58**	*2.33*	**2.03**	*0.77*
Ba	**111**	*66.09*	**73.0**	*32.21*	**753**	*75.80*	**82.2**	*95.16*	**78.0**	*33.09*
La	**154**	*26.51*	**150**	*17.49*	**47.1**	*18.54*	**196**	*26.11*	**142**	*10.81*
Ce	**228**	*28.98*	**210**	*23.63*	**77.2**	*10.89*	**318**	*188.86*	**223**	*16.14*
Pr	**21.4**	*4.02*	**20.8**	*3.05*	**8.47**	*1.83*	**21.5**	*3.71*	**20.4**	*2.24*
Nd	**72.4**	*15.17*	**65.8**	*12.50*	**34.8**	*8.50*	**69.7**	*20.21*	**65.6**	*6.97*
Sm	**11.8**	*5.41*	**10.8**	*3.59*	**7.25**	*1.90*	**11.1**	*3.39*	**9.50**	*3.22*
Eu	**1.84**	*1.16*	**1.43**	*0.63*	**1.04**	*0.69*	**1.23**	*1.17*	**1.60**	*0.69*
Gd	**8.52**	*5.63*	**9.81**	*3.02*	**7.46**	*2.55*	**6.10**	*4.61*	**8.13**	*3.44*
Tb	**1.39**	*0.69*	**1.20**	*0.50*	**1.07**	*0.36*	**1.12**	*0.71*	**1.15**	*0.45*
Dy	**8.06**	*2.72*	**7.23**	*2.60*	**7.26**	*1.91*	**7.99**	*1.92*	**7.10**	*3.03*
Ho	**1.62**	*0.60*	**1.49**	*0.70*	**1.46**	*0.44*	**1.56**	*0.45*	**1.60**	*0.40*
Er	**4.13**	*1.22*	**4.58**	*1.74*	**4.37**	*1.13*	**5.48**	*1.80*	**4.26**	*1.69*
Tm	**0.670**	*0.50*	**0.700**	*0.37*	**0.710**	*0.29*	**0.940**	*0.30*	**0.690**	*0.43*
Yb	**5.52**	*2.92*	**5.07**	*1.98*	**5.15**	*1.41*	**7.09**	*0.76*	**4.63**	*1.64*
Lu	**0.760**	*0.44*	**0.740**	*0.35*	**0.760**	*0.24*	**0.740**	*0.48*	**0.650**	*0.24*
Hf	**21.3**	*5.79*	**17.50**	*3.33*	**6.94**	*2.02*	**41.3**	*9.69*	**20.0**	*2.73*
Ta	**13.3**	*2.65*	**11.80**	*1.49*	**1.48**	*0.38*	**20.6**	*4.19*	**13.0**	*1.27*
Pb	**27.9**	*21.02*	**23.90**	*21.75*	**28.6**	*3.86*	**41.4**	*16.29*	**54.8**	*81.03*
Th	**39.2**	*8.52*	**37.40**	*5.86*	**23.8**	*4.80*	**91.9**	*15.46*	**36.6**	*4.68*
U	**6.49**	*1.38*	**5.92**	*0.83*	**4.05**	*0.67*	**12.6**	*2.68*	**6.45**	*0.96*

Table 6.20 Average trace element concentrations (ppm) to 3 sig. figs. for five Ulleungdo proximal samples, with standard deviation given in italics. Analyses were conducted at 10 Jcm^{-2}, 5 Hz and 24.2 kV. Analyses were calibrated against NIST 612 20 μm crater diameter spectra with ^{29}Si as the internal standard. Analyses are fractionation corrected against the Pearce *et al.* (2011) F.F. and F.F.s calculated in this study.

The trace element glass chemistry of the Ulleungdo samples is given in Table 6.20; analyses are fractionation corrected using the 20 µm crater diameter fractionation factor from Pearce *et al.* (2011) and 10 µm, 6 µm and 4 µm crater diameter fractionation factors calculated in this study are applied where appropriate. The thin bubble walls of Ulleungdo glass shards necessitated the use of 10 µm and 6 µm crater diameters, the less pumiceous nature of K7-B2 allowed larger 20 µm and 10 µm crater diameters to be used for analysis. Selected trace elements in glass from the Ulleungdo samples are plotted Fig. 6.20. For comparison, trace analyses of Ulleungdo-Oki (U-Oki), Ulleungdo-Ym (U-Ym; 30.9 cal. Ka; Park *et al.* 2007) and AT tephra from Park *et al.* (2007) are plotted alongside those from this study. Park *et al.* (2007) analysed the U-Oki and the older U-Ym (30.9 cal ka) tephra horizons within a marine core retrieved from the Ulleungdo Basin using solution ICP-MS.

Ulleungdo proximal units are of three different trace element glass chemistries. K1-A1, K1-B1, K1-C1 and K7-J1 are of similar trace element compositions, containing glass shards of ~10-50 ppm Hf, ~30-100 ppm Th, ~200-500 ppm Nb and ~500-2000 ppm Zr.

Glass from K7-J1 (U3) is enriched in incompatible elements relative to K1-A1 (U4), K1-B1 (U3) and K1-C1 (U2). K7-J1 glass contains ~1000 ppm higher Zr, ~30 ppm higher Th, and ~ 30 ppm higher Nb concentrations relative to other Ulleungdo units. The enrichment of incompatible elements in K7-J1 glass is consistent with its more evolved major element composition. Incompatible elements in all samples correlate positively, indicative of their progressive enrichment in the residual melt. Incompatible elements in glass from K1-A1, K1-B1, K1-C1 and occasionally K7-J1 share positive correlations of a similar gradient, indicating they are of a co-magmatic origin (Westgate *et al.,* 2011). However, gradients for K7-B2 differ from those for other glass analyses (see Fig.6.15 B and D)

Compared with glass from all other units, sample K7-B2 is depleted in incompatible elements, containing ~5-10 ppm Hf, ~0-30 ppm Th, ~0-10 ppm Nb and ~0-200 ppm Zr.

The trace element chemistry U-Oki and U-Ym from Park *et al.* (2007) is similar to that of K1-A1, K1-B1 and K1-C1. AT tephra glass shard analyses of Park *et al.* (2007) are also broadly similar to analyses of K7-B2 undertaken in this study.

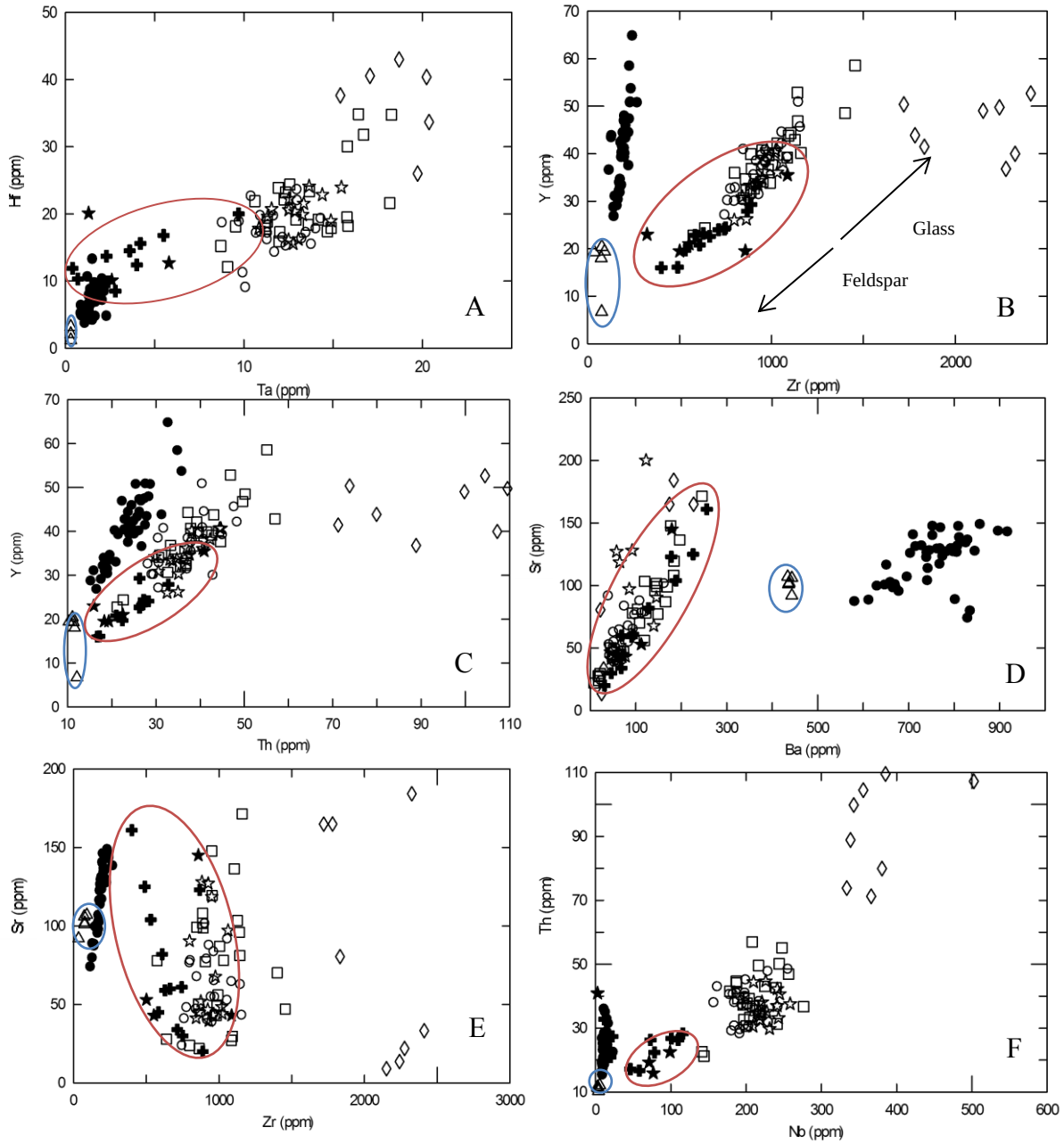

Fig. 6.20 Selected trace element variation plots for glass from Ulleungdo units, compared with U-Oki and U-Ym (ringed in red) and AT glass (ringed in blue) compositions from Park *et al.* (2007). A) Hf vs. Ta, B) Y vs. Zr, C) Y vs. Th, D) Sr vs. Ba, E) Sr vs. Zr, F) Th vs. Nb. Arrows in B) show analytical variation resulting from bulk sample analysis and inclusion of feldspars phenocrysts. All analyses from this study are fractionated corrected against firstly the Pearce *et al.* (2011) 20 µm crater diameter fractionation factor and 10 µm, 6 µm and 4 µm crater diameter fractionation factors where approproiate.

However, there are noticeable differences, with tephra compositions from Park *et al.* (2007) typically containing lower concentrations of incompatible elements than all samples analysed in this study. Park *et al.* (2007) found U-Oki and U-Ym glass to contain ~ 10-30 ppm Nb and Th, whilst K1-A1, K1-B1 and K1-C1 contain ~200-300 ppm Nb and ~40-60 ppm Th. However, glass analyses from Park *et al.* (2007) typically follow similar compositional arrays to those of this study. Dissolved bulk tephra samples were analysed by Park *et al.* (2007), thus some feldspar phenocrysts, containing lower concentrations of incompatible elements, may have been incorporated in the analysis (Pearce, *pers. comm*). Fig. 6.21 shows Th/Nb vs. Hf/Ta and Hf/Ta vs. Zr/Y plots; incompatible element ratio plots may allow comparison of bulk compositions and glass compositions (Pearce *et al.*, 2002). The trace element chemistry of K1-A1, K1-B1 and K1-C1 broadly corresponds with the trace element chemistry of U-Oki and U-Ym from Park *et al.* (2007). However, some differences remain, with U-Oki bulk from Park *et al.* (2007) containing higher Hf/Ta ratios than Ulleungdo samples studied here. Whilst there is some overlap between K7-B2 and the AT glass chemistry from Park *et al.* (2007) further proximal AT trace element glass analyses are required for comparison.

The Ulleungdo pyroclastic deposits are further defined into three compositional groups by chondrite normalised spider diagrams and Pearce tectono-magmatic Nb vs. Y and Rb vs. Y+Nb plots (Pearce *et al.*, 1983) (See Figs. 6.22).

All Ulleungdo pyroclastic deposits are typically depleted in Ba, Eu and Sr, compatible in feldspars, and Ti, compatible in Fe-Ti oxides, suggesting these phases were crystallising during the magmatic evolution of Ulleungdo.

Glass from samples K1-A1, K1-B1 and K1-C1 is typically enriched in REE. Glass from K7-J1 shows a similar trace element signature, suggesting these samples are of a co-magmatic origin. However, K7-J1 glass contains higher concentrations of the HREE, Th, Nb and Ta than glass from K1-A1, K1-B1 and K1-C1. In Fig. 6.23, mineral vector diagrams show that the more evolved composition of K7-J1 may be associated with continued removal of K-feldspar and possibly clinopyroxene during the evolution of the Ulleungdo volcanic deposits.

Fig. 6.22 C&D show that glass from K7-B2 is of a markedly different trace element composition to other Ulleungdo volcanic deposits. Glass from K7-B2 is depleted in REE, Rb, Eu and Th relative to all other Ulleungdo units, suggesting it was erupted from a

magma chamber tapping different compositions. Additionally, K7-B2 possesses a shallower REE gradient than glass from other Ulleungdo units, suggesting it may be of a differing magmatic origin. The glass in K7-B2 is characteristically depleted in Nb when compared with other Ulleungdo units, indicating K7-B2 glass was erupted from a subduction zone setting (Wilson, 1989).

Pearce diagrams (Fig. 6.22 A & B) emphasise that K7-B2 may have been erupted from a different tectonic setting to that of other Ulleungdo units. The trace element composition of K7-B2 is consistent with its eruption from a volcanic arc setting, whilst other Ulleungdo units are of a within-plate composition. This corresponds with the similarity between K7-B2 glass and Japanese volcanic products and the possibility that K7-B2 correlates to the AT tephra.

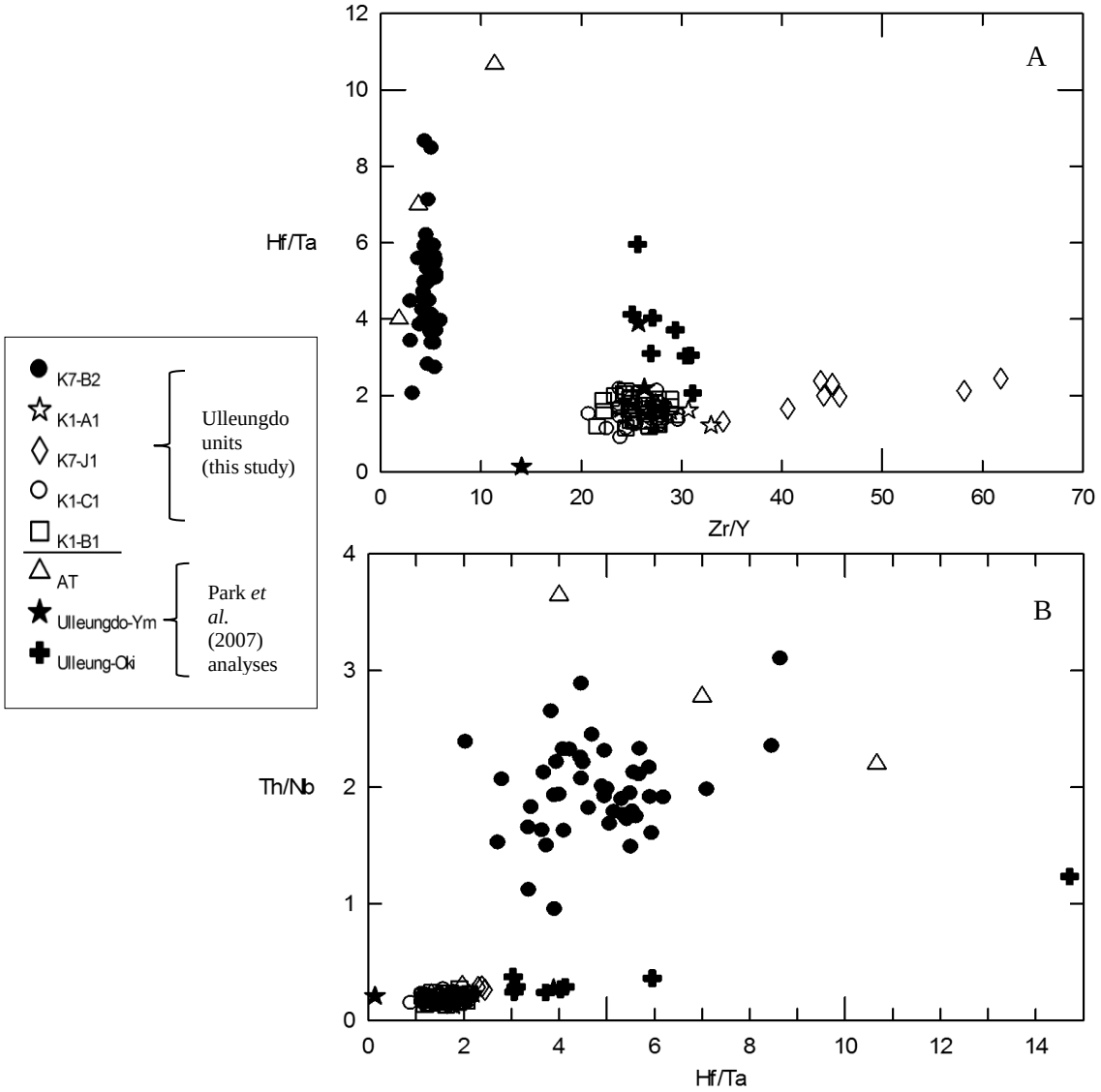

Fig. 6.21 Trace element ratios for Ulleungdo proximal glass compared with AT, U-Oki and U-Ym glass compositions from Park *et al.* (2007). A) Hf/Ta vs. Zr/Y, B) Th/Nb vs. Hf/Ta.

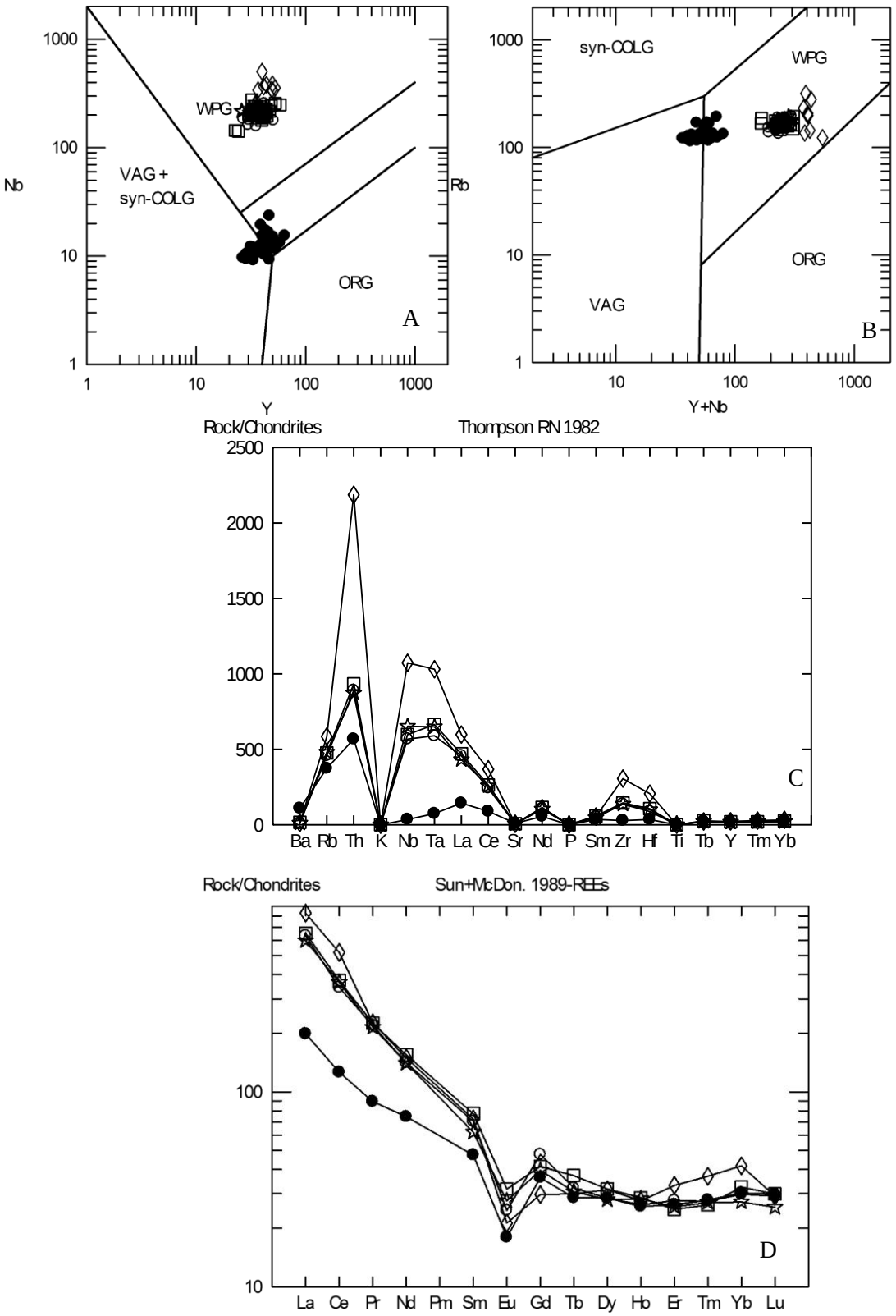

Fig. 6.22 A) and B) Pearce tectono-magmatic plots of Nb vs. Y and Rb vs. Y+Nb, respectively. VAG = volcanic arc granite, ORG = orogenic granite, WPG = within plate granite. Note that K7-B2 occupies a different tectonic field to other Ulleungdo volcanic units. C) and D) chondrite normalised trace and major element spider diagrams for Ulleungdo proximal units. Note log scale for D.

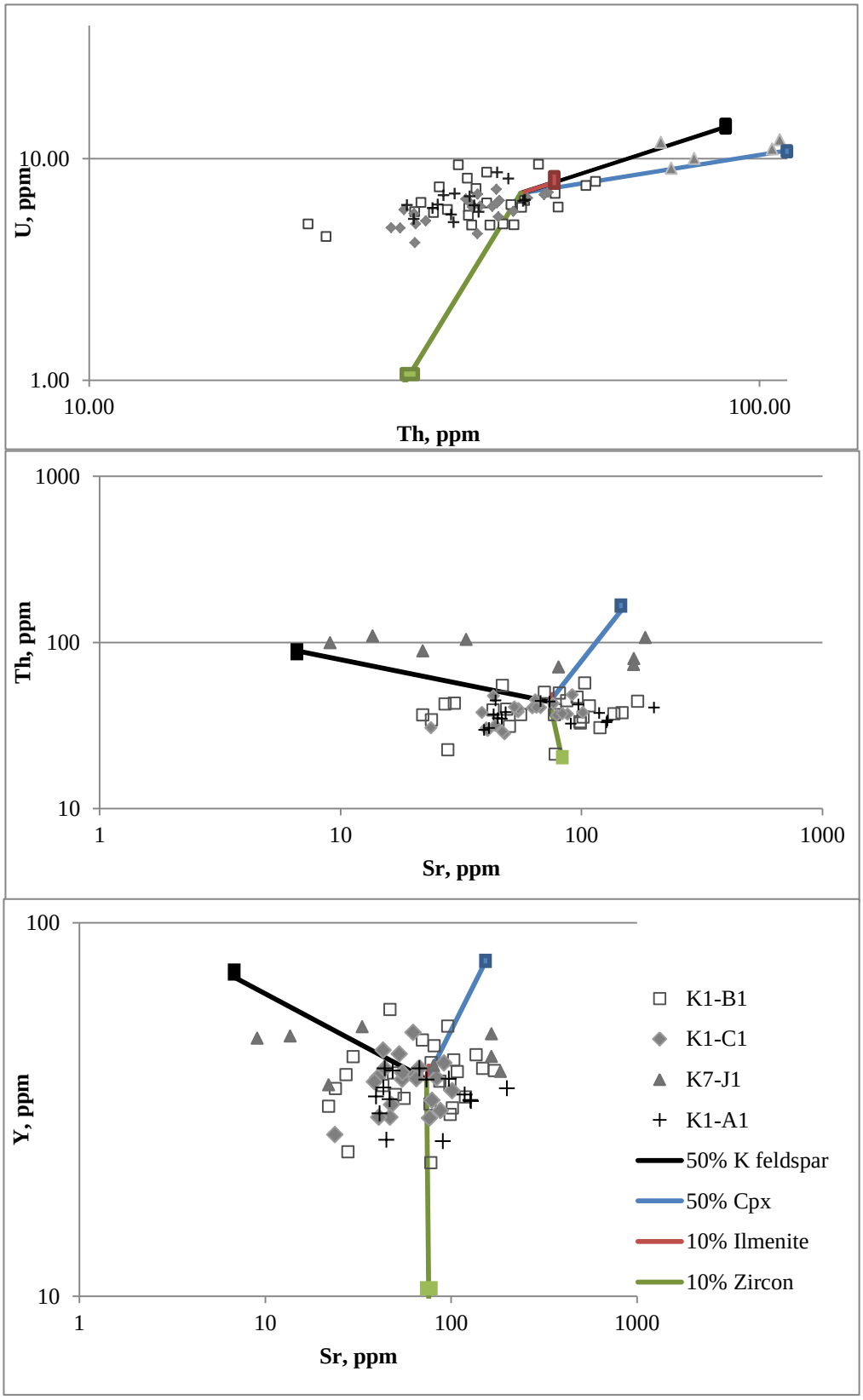

Fig. 6.23 Mineral vector diagrams indicating Rayleigh fractional crystallisation of 50% K-feldspar, 50% clinopyroxene, 10% ilmenite and 10% zircon on the melt composition of K1-B1, K1-C1, K7-J1 and K1-A1. Average trace element concentrations for all samples were used as the initial concentrations. Partition coefficients for rhyolites are taken from Rollinson (1993). Zircon Ds are from Thomas *et al.* (2002). Note log scales.

6.3 Statistical Distance Tests and Possible Correlations

Statistical distance tests were used to compare the composition of five samples, K1-A1, K1-B1, K1-C1, K7-J1 and K7-B2 collected from Ulleungdo, Korea. In addition, sample K7-B2 will be compared with Aira-Tanzawa proximal deposits, ITJ5, ITJ7 and ITJ8.

The statistical distance between tephra deposits is summarized in the equation (3) from Perkins *et al.* (1998).

$$D^2 = \sum_{k=1}^{n} (x_{k1} - x_{k2})^2 / (\sigma_{k1}^2 + \sigma_{k2}^2) \qquad \textbf{(3)}$$

n= number of elements in the comparison
x_{k1} and x_{k2} = the concentrations of the element being compared in each sample
$\sigma_{k1}$and σ_{k2} = the standard deviations on the element concentrations

Pearce *et al.* (2008) state that the calculated D^2 has a Chi-squared distribution where data is normally distributed. Fig. 6.30 shows the major and trace element concentrations for Ulleungdo samples K1-A1, K1-B1, K1-C1 and K7-J1. They are broadly of a normal distribution therefore the statistical distance test may be used to give an approximate comparison of tephra compositions.

The calculated statistical distance between major element concentrations of K1-A1, K1-B1, K1-C1, K1-J1, K7-B2 are compared with major element concentrations from Smith *et al.* (2011a). Additionally, K7-B2 is compared with AT major element concentrations from Smith *et al.* (submitted) and trace element concentrations from Park *et al.* (2007). The results of the statistical distance tests are given in Table 6.30.

Ten major and 9 petrogenically significant trace elements concentrations are compared in all samples, giving respective D^2 critical values of 23.21 and 21.67 at the 99.9% confidence level (Runyon and Haber, 1988). The null hypothesis is that at a given confidence level, two tephra deposits are compositionally the same. Where $D^2_{calculated} < D^2_{critical}$, the null hypothesis is accepted, greater calculated D^2 indicates more compositional difference.

Through comparing the major element composition of glass shards in five samples from Ulleungdo, the statistical distance between K1-A1 (U4), K1-B1 (U3) and K1-C1 (U2) is typically <3 and therefore these units are compositionally very similar in terms of their major and trace elements. Of all Ulleungdo units analysed in this study, K1-B1 (U3) is

statistically closest to the U-Oki tephra from the Suigetsu core, contrasting with correlations between U-Oki and U4 made by Okuno *et al.* (2010) and Smith *et al.* (submitted).

Sample K7-J1 (U3) has a greater calculated statistical distance from K1-A1, K1-B1 and K1-C1, calculated at ~20 for major elements and ~50 for trace elements. In terms of its trace element composition, K7-J1 is therefore statistically different from other Ulleungdo samples, due to its comparatively evolved composition. Sample K7-B2 (AT?) is statistically distinct from other Ulleungdo units in terms of its major and trace elements, with statistical distances of <~900 and ~600 respectively. The $D^2_{calculated}$ for major element concentrations in K7-B2 compared with the AT proximal deposits (ITJ5, ITJ7 and IT78) is ~2, thus K7-B2 shares a similar major element composition to that of the AT tephra. However, when trace element concentrations in K7-B2 are compared with those from the AT tephra, published by Park *et al.* (2007) they are statistically different ($D^2_{calculated}$ = ~50).

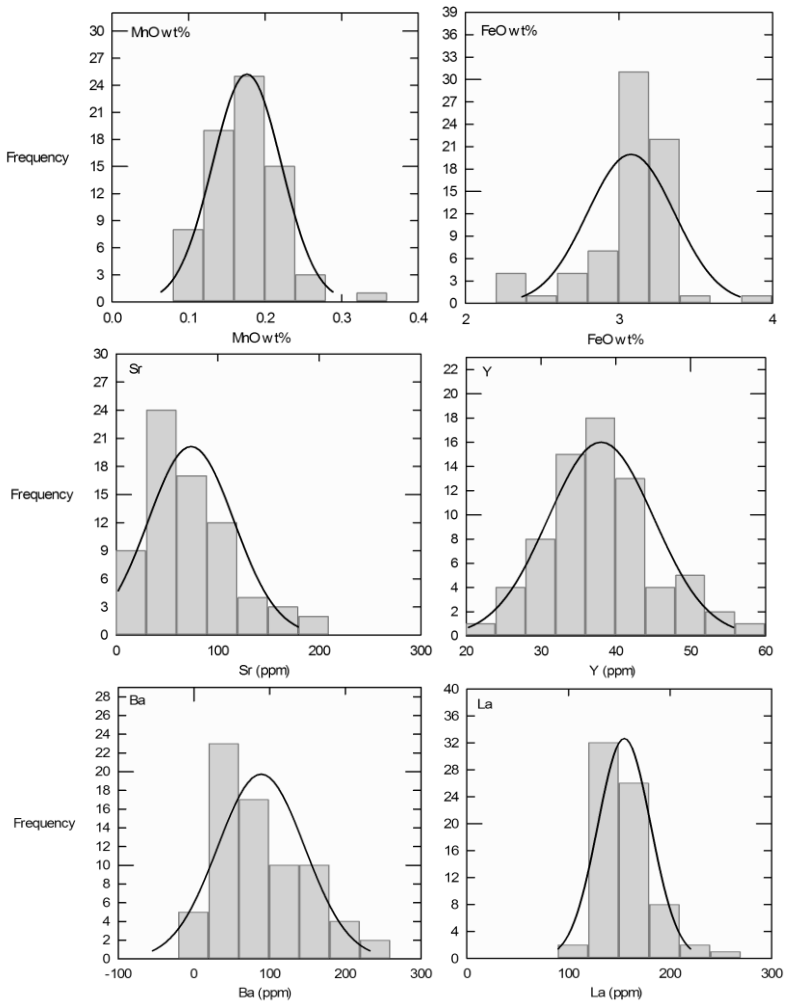

Fig. 6.30 Histograms for selected trace and major elements in Ulleungdo proximal units.

Major element $D^2_{critical}$ = 23.21	**K1-A1** *(U4)*	**K1-B1** *(U3?)*	**K1-C1** *(U2)*	**K7-J1** *(U3)*	**K7-B2** *(AT?)*	**SGO6_1288** *(U-Oki)*
K1-A1 *(U4)*	0.00					
K1-B1 *(U3?)*	2.04	0.00				
K1-C1 *(U2)*	1.23	1.88	0.00			
K7-J1 *(U3)*	7.12	18.78	11.91	0.00		
K7-B2 *(AT?)*	602.85	425.01	885.43	611.63	0.00	
SGO6_1288 *(U-Oki)*	2.34	0.82	1.98	18.48	2299.37	0.00
	ITJ8 *(AT)*	**ITJ7** *(AT)*	**IT75** *(AT)*			
K7-B2 *(AT?)*	2.54	1.18	2.22			
Trace element $D^2_{critical}$ = 21.67	**K1-A1** *(U4)*	**K1-B1** *(U3?)*	**K1-C1** *(U2)*	**K7-J1** *(U3)*	**K7-B2** *(AT?)*	**AT Park *et al.*, (2007)**
K1-A1 *(U4)*	0.00					
K1-B1 *(U3?)*	1.54	0.00				
K1-C1 *(U2)*	2.60	1.62	0.00			
K7-J1 *(U3)*	52.85	50.59	50.59	0.00		
K7-B2 *(AT?)*	474.74	152.75	229.22	191.66	0.00	
AT Park *et al.*, (2007)	506.53	112.22	260.72	167.58	47.61	0.00

Table 6.30 Calculated D^2 for Ulleungdo proximal units and possible correlatives. Major element concentrations in Ulleungdo proximal units are compared with U-Oki (from Smith *et al.* 2011a) and K7-B2 glass is compared with AT proximal glass compositions (from Smith *et al.* submitted). Trace element concentrations in Ulleungdo proximal units are compared with AT glass compositions from Park *et al.* (2007).

This statistical difference may be because bulk tephra samples, containing contaminant phases, were analysed by Park *et al.* (2007).

Therefore, the Ulleungdo proximal Units 2, 3 and 4 share a similar major and trace element composition. A duplicate sample of U3 (K7-J1) possesses a different major and trace element glass composition to both that of another sample from U3 and U2 and U4, possibly due to continued fractional crystallisation of feldspar in the Ulleungdo magma chamber. Further trace element and mineral analysis is therefore required to distinguish between Ulleungdo units and correlate further with the Suigetsu core. Rhyolitic glass from sample K7-B2 contrasts with all other Ulleungdo units and has a similar major element composition to the AT tephra. Further trace element analysis of glass separates from AT proximal units is required before K7-B2 can be correlated.

Chapter 7 Conclusions

Laser ablation inductively coupled plasma-mass spectrometry (LA-ICP-MS) is ideally suited to the trace element analysis of individual volcanic glass shards. Recent developments in the LA-ICP-MS analysis of volcanic glass shards have been driven by the ambition to characterize increasingly distal tephra shards and correlate tephra isochrons over greater distances (Pearce *et al.* 2011).

This study demonstrates that 26 trace elements may be quantified in a range of volcanic glass compositions using 20 µm and 10 µm crater diameters (see Table 3.10). Nine petrogenically significant trace elements (Rb, Y, Zr, Th, U and the LREE) remain above 10 times the standard deviation on the gas blank (above LLQ) using 6 µm crater diameters and above 3 times the standard deviation on the gas blank (above LLD) using 4 µm crater diameters (see Table 3.11). Through scanning only for these detectable elements using 4 µm crater diameters, more time will be spent on each element peak and the signal for each may be improved, thus they may become quantifiable. Low concentration of CaO in rhyolites (< 2wt%) means that neither ^{44}Ca or ^{43}Ca are quantifiable in rhyolitic glass using <10 µm crater diameters. ^{29}Si is present above LLQ in rhyolitic glass analyses performed at <10 µm crater diameter and is therefore a suitable internal standard for rhyolitic glass analyses at small spot sizes. ^{44}Ca and ^{43}Ca are only suitable internal standards for the analysis of basic glasses using >10 µm crater diameters. This is the result the improved signal/noise ratio at mass 29 compared with for ^{44}Ca and ^{43}Ca (Pearce *et al.,* 2011). However, analysis using 6 µm and 4 µm crater diameters is subject to large analytical errors, ±20% and ±30-50%, respectively.

Element Fractionation

Glass analyses performed using <20 µm crater diameters suffer from increased element fractionation; the non-stoichiometric removal of material from the sample. Pearce *et al.* (2011) found element fractionation increased with both decreasing crater diameter and increasing polymerisation and calculated fractionation factors to compensate for element fractionation at 20 µm and 10 µm crater diameters.

This study has further investigated element fractionation with the aim of correcting for its effects at 6 µm and 4 µm crater diameters. Sixteen USGS and MPI-DING reference materials and tephra samples of basic, intermediate and acidic compositions were

repeatedly analysed using 20 µm, 10 µm, 6 µm and 4 µm crater diameters. With decreasing crater diameter, measured concentrations become increasingly biased away from preferred concentrations and those measured from 20 µm crater diameters. Fractionation indices for 20 µm, 10 µm, 6 µm and 4 µm crater diameters (concentration measured at *x* µm crater diameter/ concentration measured at 20 µm crater diameters, Pearce *et al.,* 2011) were calculated for each sample. Analyses demonstrate that fractionation increases with decreasing crater diameter. Relative to preferred concentrations; Zr is underrepresented by on average ~10% using 10 µm crater diameters, ~20% using 6 µm crater diameters and ~25% using 4 µm crater diameters. This increase in fractionation reflects the changing aspect ratio of craters with decreasing crater diameter described by Pearce *et al.,* (2011). Fractionation is thought to originate from a melt film lining the interior of ablation craters (Pearce *et al.,* 2011). At smaller crater sizes the melt film occupies a larger volume of the crater and thus fractionation becomes significant (Pearce *et al.,* 2011).

The high field strength elements (Zr, Th, U) are typically increasingly underrepresented, and the LILE (Rb, Cs) are increasingly overrepresented, with decreasing crater diameter. However, this study found no correlation between trace element ionic radius, ionization energy, charge, field strength and condensation temperature and whether elements are under or overrepresented and how dramatically they fractionate. This contrasts with the findings of Jeffries *et al.* (1997), who used an IR laser to demonstrate that those elements of a smaller ionic radius are more tightly bound within the sample matrix and less easily removed during ablation, thus typically underrepresented. Infra-red lasers ablate the sample differently to the 193 nm laser used in this study, resulting in differing fractionation effects. Recent studies using a 193 nm laser suggest that the response of elements to fractionation does not vary significantly with condensation temperature (Tomlinson *et al.*, 2010).

Analyses of ATHO-G at a range of crater diameters were repeated at 24.2 kV and then 28 kV, whilst the laser fluence and repetition rate were kept constant. Where 20 µm and 10 µm crater diameters and a 28 kV excitation voltage are used, element fractionation appears to increase by ~5-10% when compared with analyses conducted at the same crater diameter and a 24.2 kV excitation voltage. However, the fractionation of analyses conducted at crater diameters of <10 µm is unaffected by changing the excitation voltage.

Using an ArF Excimer laser, Feenstra *et al.* (1999) found the pulse length increased from 55 ns to 80 ns when the excitation voltage was increased from 4.1 kV to 7.9 kV. Longer pulse durations may cause increased heating at the sample surface and possibly promote the formation of the melt film from which element fractionation may originate (Pearce *et al.*, 2011). If pulse duration increases at higher excitation voltages this may explain why the fractionation of crater of >10 µm diameter is marginally increased at higher excitation voltages.

This study demonstrates that different samples fractionate differently. Gaboardi and Humayan (2009) suggest that more transparent samples, containing lower FeOwt%, are ablated less efficiently, releasing larger particles which fractionate more strongly.

Pearce *et al.* (2011) described a linear increase in element fractionation with increasing sample polymerisation. Polymerisation gives an indication of melt structure, which may affect how strongly elements are bonded within a sample, thus how dramatically elements are fractionated. Through repeatedly analysing a wider compositional suite of samples than Pearce *et al.* (2011), this study finds that element fractionation is neither related to signal intensity nor element concentration, suggesting other factors cause variations in element fractionation between samples. Additionally, fractionation does not correlate with sample viscosity, liquidus temperature and iron concentration; all interlinked parameters. The fractionation of <10 µm crater diameters increases with decreasing sample viscosity, increasing liquidus temperature and iron concentration – so that basic samples are ~50% more fractionated than acidic samples. However, samples of similar composition fractionate differently, suggesting other factors may be associated with element fractionation. Additionally, analysis at <10 µm crater diameters is typically subject to low analytical precision.

The correlation between element fractionation and crater diameter allows the calculation of fractionation factors (F.F.s) to correct for fractionation. Three F.F.s were calculated, for the correction of concentrations measured from 10 µm, 6 µm and 4 µm crater diameters. Fractionation indices (F.I., concentrations determined from 10 µm, 6 µm and 4 µm/ 20 µm crater diameter concentrations) were calculated for sixteen reference materials (NIST 610, NIST 612, BCR-2G, BHVO-2G, KL2-G, StHs/680G, T1-G, ATHO-G) and tephra samples (UT1588, UT1440,UT2015, UT1285, UT1287, Chabbi and Newberry Obsidians and CF86). All measured concentrations were initially corrected using the 20 µm crater

diameter F.F. from Pearce *et al.* (2011). F.I.s for 10 µm, 6 µm and 4 µm crater diameter and for all samples were then averaged to give respective 10 µm, 6 µm and 4 µm crater diameter fractionation factors.

Fractionation factors can be applied to glass shard analyses where ^{29}Si is the internal standard. All glass analyses should first be fractionation corrected using the 20 µm crater diameter from Pearce *et al.* (2011). Glass analyses can then be divided by the relevant crater diameter F.F. from this study. Fractionation factors calculated in this study were tested on Minoan (~75wt% SiO_2) and UT2252 (~45wt% SiO_2) glass analyses from Pearce *et al.* (2011). Whilst noisy, measured trace element concentrations from < 10 µm crater diameters are brought to within ±20% of measured concentrations from 20 µm crater diameters. Fractionation correction at <10 µm crater diameters will allow analysis of finer glass shards with increased accuracy.

Characterisation of Ulleungdo Tephra

Ulleungdo (Korea) proximal units are of similar major element compositions and of a highly pumiceous nature (Smith *et al.* 2011). The alkaline SG06-1288 tephra horizon within the Lake Suigetsu (Japan) SG06 core has recently been correlated to Unit 4 of Ulleungdo and dating of the proximal U4 tephra has independently verified the chronology of SG06 (Smith *et al.,* 2011a). The similar major element composition of the Ulleungdo units requires trace element analysis at <10 µm crater diameters in order to correlate them further with the SG06 archive. Glass within Ulleungdo proximal Units 2, 3 and 4 and a deposit possibly corresponding to the Japanese AT tephra was analysed for major and trace elements. Fractionation factors calculated in this study were applied where appropriate.

Ulleungdo proximal units are phonolitic, having evolved through fractional crystallisation of alkali feldspar and Fe-Ti oxides. Glass shards within Ulleungdo Units 2,3 and 4 are of a similar major and trace element composition. One duplicate sample of U3 is more compositionally evolved, containing higher concentrations of incompatible elements and lower SiO_2wt%, than other samples from U2, U3 and U4. Major and trace element analyses of U2, U3 and U4 compare well with the compositions of Ulleungdo volcanic products from Shiihara *et al.* (2011) and Park *et al.* (2007).

A tephra deposit from Ulleungdo (sample K7-B2), possibly corresponding to the AT tephra (erupted from Aira Caldera, south Kyushu, Japan), is distinctly rhyolitic; contrasting

with the alkaline composition of Ulleungdo volcanism. This rhyolitic Ulleungdo deposit shares a similar major and trace element composition to the composition of proximal and distal AT tephra from Park *et al.* (2007) and Smith *et al.* (submitted). However, the rhyolitic Ulleungdo tephra contains ~0.5wt% lower SiO_2, Na_2O and FeO and there is insufficient trace element AT proximal glass analyses available for comparison. Relative to other Ulleungdo units, the rhyolitic Ulleungdo deposit contains glass shards of lower LREE concentrations and is markedly depleted in Nb. This may suggest it originated from a subduction zone setting, as verified by Pearce-type tectono-magmatic diagrams, agreeing with the possibility it may be a Japanese tephra (Pearce *et al.,* 1983).

Future Research

In order to widen the scope of this study, several additional factors could be investigated. Whilst this study has corrected for fractionation associated with crater diameter, some differential fractionation still exists between samples. The analysis of more glass compositions may allow further investigation of the response of different samples to element fractionation. Additionally, samples of similar compositions could be differently annealed, giving differing glass structures that may fractionate differently. Annealed samples of natural compositions and synthetic compositions could also be analysed, as they may fractionate differently.

Further research is also required in order to establish the relationship between excitation voltage and laser pulse duration. The influence of excitation voltage on element fractionation was only tested during one analytical session and using one sample; thus repeat analyses of different samples whilst altering the excitation voltage are required in order to test reproducibility. Pulse duration variations concomitant with altering the excitation voltage could be monitored using an oscillograph. Additionally, the impact of repetition rate and laser fluence on the laser pulse duration also requires investigation. Ultimately the replacement of nanosecond lasers with femtosecond lasers should reduce melting at the sample surface and subsequent element fractionation (Pearce *et al.,* 2011).

Whilst fractionation effects studied here are related to laser-sample interaction, the precision at <10 µm crater diameters may be improved through coupling the 193 nm Excimer laser to the Agillent quadrupole based ICP-MS at Aberystwyth. Quadrupole-based ICP-MS are capable of peak hopping, faster scanning and have a collision cell, which may reduce polyatomic interferences and therefore may provide greater precision.

Fractionation experiments could also be run with the guard electrode on; this may increase sensitivity at lower masses yet may increase oxides if not monitored carefully (Pearce *et al.*, 2011). Furthermore, fractionation effects may also be investigated whilst using helium as a carrier gas; this may increase the sensitivity at < 10 µm crater diameters.

Finally, further trace element analysis of glass and minerals from both Ulleungdo and AT proximal deposits is necessary before the Ulleungdo tephra deposits can be further correlated with the Suigetsu SG06, Japan, core.

Reference List

Abbott, P.M., Davies, S.M., Austin, W.E.N., Pearce, N.J.G., Hibbert, F.D., 2011. Identification of cryptotephra horizons in a North East Atlantic marine record spanning marine isotope stages 4 and 5a (~60,000–82,000 a b2k). Quaternary International 246, 177-189.

Arrowsmith, P., 1987. Laser Ablation of Solids for Elemental Analysis by Inductively Coupled Plasma Mass Spectrometry. Analytical Chemistry 59, 1437-1444.

Blockley, S.P.E., Pyne-O'Donnell S.D.F., Lowe J.J., Matthews I.P., Stone A., Pollard, A.M., 2005. A new and less destructive laboratory procedure for the physical separation of distal glass tephra shards from sediments. Quaternary Science Reviews 24, 1952-1960.

Borisova, A., Freydier, R., Polve, M., Jochum, K.P., Candaudap, F., 2010. Multi element analysis of ATHO-G rhyolitic glass (MPI-DING reference material) by femtosecond and nanosecond LA-ICP-MS: evidence for significant heterogenity of B,V, Zn, Mo, Sn, Sb, Cs, W, Pt and Pb at the millimetre scale. Geostandards and Geoanalytical Research 34, 245-255.

Bowen, N.L., 1956. The Evolution of Igneous Rocks Dover Publications, New York.

Bronk Ramsey, C., Staff, R.A., Bryant, C., Brock, F., Kitagawa, H., van der Plicht, J., Schlolaut, G., Marshall, M., Brauer, B., Lamb, H.F., Payne, R.L., Tarasov, P.E., Haraguchi, T., Gotanda, K., Yonenobu, H., Yokoyama, Y., Tada, R., Nakagawa, T., 2012. A Complete Terrestrial Radiocarbon Record for 11.2 to 52.8 kyr B.P. Science 338, 370-374.

Bryant, C.J., Arculus, R.J., Eggins, S.M., 1999. Laser ablation - inductively coupled plasma-mass spectrometry and tephra: A new approach to understanding arc-magma genesis, Geology 27, 1119-1122.

Cas, R.A.F., Wright, J.V., 1987. Volcanic Successions, Modern and Ancient. Allen and Unwin, London.

Chen, Z., 1999. Interelement fractionation and correction in laser ablation inductively coupled plasma mass spectrometry. Journal of Analytical Atomic Spectrometry 14, 1823-1828.

Clugston, M., Flemming, R., 2000. Advanced Chemistry. Oxford University Press.

Coulter, S.E., Pilcher, J.R., Hall, V.A., Plunkett, G., Davies, S.M., 2010. Testing the reliability of JEOL FEGSEM 6500F electron microprobe for quantitive major element analysis of glass shards from rhyolitic tephra, Boreas 39, 163-169.

Czas, J., Jochum, K.P., Stoll, B., Weis, D., Yango, Q.C., Jocob, D.E., Andreae, M.O., 2012. Investigation of matrix effects in 193 nm laser ablation – inductively coupled plasma - mass spectrometry analysis using reference glasses of different transparencies. Spectrochimica Acta Part B 78, 20-28.

Deubener, J., Müller, R., Behrens, H., Heide, G., 2003. Water and the glass transition temperature of silicate melts. Journal of Non-Crystalline Solids 330, 268-273.

Eastwood, W.J., Pearce, N.J.G., Westgate, J.A., Perkins, W., 1998. Recognition of Santorini (Minoan) tephra in lake sediments from Golhisar Golu, southwest Turkey by laser ablation ICP-MS. Journal of Archaeological Science 25, 677-687.

Eastwood, W.J., Pearce, N.J.G., Westgate, J.A., Perkins, W., Lamb, H.F., Roberts, N., 1999. Geochemistry of Santorini tephra in lake sediments from Southwest Turkey. Global and Planetry Change 21, 17-29.

Eggins, S.M., Kingsley, L.P.J., Shelley, J.M.G., 1998. Deposition and element fractionation processes during atmospheric pressure laser sampling for analysis by ICP-MS. Appl. Surf. Sci. 129, 278-286.

Feenstra, L., Bastiaens, H.M.J., Peters, P.J.M., Witteman, W.J., 1999. On the Extension of the Pulse Length of a Discharge Excited ArF Excimer Laser. Laser Physics 10, 382-386.

Fernández, B., Claverie, F., Pécheyran, C., Donard, O.F.X., 2007. Direct analysis of solid samples by fs-LA-ICP-MS. TrAC Trends in Analytical Chemistry 26, 951-966.

Francis, P., Oppenheimer, C., 2004. Volcanoes. Oxford University Press.

Gaboardi, M., Humayan, M., 2009. Elemental fractionation during LA-ICP-MS analysis of silicate glasses: implications for matrix-independent standardization. Journal of Analytical Atomic Spectrometry 24, 1188-1197.

Gray, A.L., 1985. Solid Sample Introduction by Laser Ablation for Inductively Coupled Plasma Source Mass Spectrometry. The Analyst 110, 551-556.

Gunther, D., Hattendorf, B., 2005. Solid sample analysis using laser ablation inductively coupled plasma mass spectrometry. TrAC Trends in Analytical Chemistry 24, 255-265.

Gunther, D., Kroslakova, I. 2006. Elemental fractionation in laser ablation-inductively coupled plasma-mass spectrometry: evidence for mass load induced matrix effects in the ICP during ablation of a silicate glass. Journal of Analytical Atomic Spectrometry 22, 51-62.

Hayward, C., 2011. High spatial resolution electron probe microanalysis of tephras and melt inclusions without beam-induced chemical modification. The Holocene 22, 119-125.

Heinrich, C.A., Pettke, T. Halter, W.E., Aigner-Torres, M. Audetat, A., Gunther, D., Hattendorf. B, Bleiner, D. Guillong, M., Horn. I., 2003. Quantitative multi-element analysis of minerals, fluid and melt inclusions by laser-ablation inductively-coupled-plasma mass-spectrometry, Geochimica et Cosmochimica Acta 67, 3473-3497.

Hergenroger, R., 2006. A model of non-congruent laser ablation as a source of fractionation effects in LA-ICP-MS. Journal of Analytical Atomic Spectrometry 21, 501-516.

Higgins, M.W., 1973. Petrology of Newberry Volcano, Central Oregon. Geological Society of America Bulletin 84, 455-488.

Hirata, T., 1997. Ablation Technique for Laser Ablation–Inductively Coupled Plasma Mass Spectrometry, Journal of Analytical Atomic Spectrometry 12, 1337-1342.

Horn, I., Gunther, D. 2003, The influence of ablation carrier gasses Ar, He and Ne on the particle size distribution and transport efficiencies of laser ablation-induced aerosols: implications for LA–ICP–MS, Applied Surface Science 207, 144-157.

Humphreys, M.C.S., Kearns, S.L., Blundy, J.D., 2006. SIMS investigation of electron-beam damage to hydrous, rhyolitic glasses: Implications for melt inclusion analysis. American Mineralogist 91, 667-679.

Jackson, S.E., Longerich, H.P., Dunning, G.R., Fryer, B.R., 1992. The application of laser ablation microprobe-inductively coupled plasma mass spectrometry (LAM-ICP-MS) to in-situ trace element dterminations in minerals. Canadian Mineralogist 30, 1049-1064.

James, A.M., Lord, M.P., 1992. Macmillan's Chemical and Physical Data. Macmillan, London.

Jeffries, T.E., Pearce, N.J.G., Perkins, W.T., Raith, A., 1996. Chemical fractionation during infrared and ultraviolet laser ablation inductively coupled plasma mass spectrometry, implications for mineral microanalysis. Analytical Communications 33, 35.

Jenner, F., O'Neill, H., Major and trace analysis of basaltic glasses by laser-ablation ICP-MS, Geochemistry, Geophysics, Geosytems 13 (3).

Jochum, K.P., 2005. Geological and Environmental Reference Materials (GeoReM).

Jochum, K.P., Pfander, J., Woodhead, J.D., Willbold, M., Stoll, B., Herwig, K., Amini, M., Abouchami, W., Hofmann, A.W., 2005. MPI-DING glasses: New geological reference materials for in situ Pb isotope analysis. Geochemistry, Geophysics, Geosytems 6, 1-15.

Jochum, K.P., Stoll, B., Herwig, K., Willbold, M., Hofmann, A.W., Amini, M., Aarburg, S., Abouchami, W., Hellebrand, E., Mocek, B., Raczek, I., Stracke, A., Alard, O., Bouman, C., Becker, S., Dücking, M., Brätz, H., Klemd, R., de Bruin, D., Canil, D., Cornell, D., de Hoog, C.-J., Dalpé, C., Danyushevsky, L., Eisenhauer, A., Gao, Y., Snow, J.E., Groschopf, N., Günther, D., Latkoczy, C., Guillong, M., Hauri, E.H., Höfer, H.E., Lahaye, Y., Horz, K., Jacob, D.E., Kasemann, S.A., Kent, A.J.R., Ludwig, T., Zack, T., Mason, P.R.D., Meixner, A., Rosner, M., Misawa, K., Nash, B.P., Pfänder, J., Premo, W.R., Sun, W.D., Tiepolo, M., Vannucci, R., Vennemann, T., Wayne, D., Woodhead, J.D., 2006. MPI-DING reference glasses for in situ microanalysis: New reference values for element concentrations and isotope ratios. Geochemistry Geophysics Geosystems 7, 2.

Kane, S., 1998. A History of the Development and Certification of NIS T Glass SRMs 610-617. Journal of Geostandards and Geoanalysis 22, 7-13.

Kempenaers, L., Janssens, K., Jochum, K.P., Vincze., L., Vekemands, A., Somogyi, A., Drakopoulos, M., Adams, F., 2003. Micro-heterogeneity study of trace elements in USGS, MPI-DING and NIST glass reference materials by means of synchrotron micro-XRF. Journal of Analytical Atomic Spectrometry 18, 350-357.

Kim, K.H., Nagao, K., Sumino, H., Tanaka, T., Hayashi, T., Nakamura, T., Lee, J.I., 2008. He–Ar and Nd–Sr isotopic compositions of late Pleistocene felsic plutonic back arc basin rocks from Ulleungdo volcanic island, South Korea: Implications for the genesis of young plutonic rocks in a back arc basin. Chemical Geology 253, 180-195.

Kuehn, S.C., Froese, D.G., 2010. Tephra from ice - a simple method to routinely mount, polish and quantitively analyse sparse fine particles. Microscopy and Microanalysis 16, 218-225.

Kuehn, S.C., Froese, D.G., Shane, P.A.R., Participants, N.I., 2011. The INTAV intercomparison of electron-beam microanalysis of glass by teprhochronolgy laboratories, results and recommendations. Quaternary International 246, 19-47.

Kuhn, H.R., Gunther, D., 2004. Laser ablation-ICP-MS: particle size dependent elemental composition studies on filter-collected and online measured aerosols from glass. Journal of Analytical Atomic Spectrometry 19, 1158-1164.

Lodders, K., 2003. Abundances and Condensation Temperatures of the Elements. The Astrophysical Journal 591, 1220-1247.

Lowe, D.J., 2011. Tephrochronology and its application: A review. Quaternary Geochronology 6, 107-153.

MacDonald, R., Gibson, I.L., 1969. Pantelleritic Obsidians from the Volcano Chabbi (Ethiopia). Contr. Mineral. and Petrol. 24, 239-244.
Machida, H., 2002. Volcanoes and Tephras in the Japan Area. Global Environmental Research, 6, 19-28.
Machida, H., Arai, F., Lee, B.S., Moriwaki, H., Furuta, T., 1984. Late Quaternary tephras in Ulleung-do island, Korea. Journal of Geography 93, 1-14.
Mank, A.J.G., Mason, P.R.D., 1999. A critical assessment of laser ablation ICP-MS as an analytical tool for depth analysis in silica-based glass samples. Journal of Analytical Atomic Spectrometry 14,1143-1153.
Mysen, B.O., 1983. The structure of silicate melts. Annual Reviews Earth and Planetary Science 11, 75-97.
Nakagawa, T., Gotanda, K., Haraguchi, T., Danhara, T., Yonenobu, H., Brauer, A., Yokoyama, Y., Tada, R., Takemura, K., Staff, R.A., Payne, R., Bronk Ramsey, R., Bryant, C.J., Brock, I., Scholaut, G., Marshall, M., Tarasov, R., Lamb, H.F., Suigetsu Project Members., 2011. SG06, a fully continuous and varved sediment core from Lake Suigetsu, Japan: stratigraphy and potential for improving the radiocarbon calibration model and understanding of late Quaternary climate changes. Quaternary Science Reviews 36, 164-176.
Okuno, M., Shiihara, M., Torri, M., Nakamura, T., Kim, K.H., Domitsu, H., Moriwaki, H., Oda, M., 2010. AMS radiocarbon dating of Holocene tephra layers on Ulleung island, South Korea. Radiocarbon 54, 1465-1470.
Park, M.H., Kim, J., Kil, Y., 2007. Identification of the late Quaternary tephra layers in the Ulleung Basin of the East Sea using geochemical and statistical methods. Marine Geology 244, 196-208.
Pearce, N.J.G., Alloway, B.V., Westgate, J.A., 2008. Mid-Pleistocene silicic tephra beds in the Auckland region, New Zealand: Their correlation and origins based on the race element analyses of single glass shards. Quaternary International 178, 16-43.
Pearce, N.J.G., Denton, J.S., Perkins, W., Westgate, J.A., Alloway, B.V., 2007. Correlation and characterisation of individual glass shards from tephra deposits using element laser ablation ICP-MS analyses: current status and future potential Journal of Quaternary Science 22, 721-736.
Pearce, N.J.G., Eastwood, W.J., Westgate, J.A., Perkins, W., 2002. Trace element composition of single glass shards in distal Minoan tephra from SW Turkey. Journal of the Geological Society 159, 545-556.
Pearce, N.J.G., Perkins, W., Eastwood, W.J., Shane, P.A., 1999. Application of laser ablation ICP-MS to tephrochronology: bulk and single shard analysis Applied Geochemistry 19, 289-322.
Pearce, N.J.G., Perkins, W., Westgate, J.A., Wade, S.C., 2011. Trace-element microanalysis by LA-ICP-MS: The quest for comprehensive chemical characterisation of single, sub-10 μm volcanic glass shards. Quaternary International, 246, 1-25.
Pearce, N.J.G., Westgate, J.A., Perkins, W., 1995. Developments in the analysis of volcanic glass shards by laser-ablation ICP-MS: Quantitive and single internal standard-multi-element methods. Quaternary International 34-36, 213-227.
Pearce, N.J.G., Westgate, J.A., Perkins, W.T., Preece, S.J., 2004. The application of ICP-MS methods to tephrochronological problems. Applied Geochemistry 19, 289-322.
Pearce, J.A., Harris, N.B.W., Tindle, A.G., 1983. Trace Element Discrimmination Diagrams for the Tectonic Interpretation of Granitic Rock. Journal of Petrology 25, 956-983.
Perkins, M.E., Brown, F.H., Nash, W.P., McIntosh, W., Williams, S.K., 1998. Sequence, age, and source of silicic fallout tuffs in middle to late Miocene basins of the northern Basin and Range province. Bulletin of the Geological Society of America 110, 344–360.
Perkins, W., Pearce, N.J.G., Westgate, J.A., 1997. The Development of Laser Ablation ICP-MS and Calibration Strategies: Examples from the Analysis of Trace Elements in Volcanic Glass Shards and Sulfide Minerals. Journal of Geostandards and Geoanalysis 21, 175-190.
Pisonero, J., Günther, D., 2008. Femtosecond laser ablation inductively coupled plasma mass spectrometry: Fundamentals and capabilities for depth profiling analysis. Mass Spectrometry Reviews 27, 609-623.
Pollard, A.M., Blockley, S.P.E., Lane, C.S., 2006. Some numerical considerations in the geochemical analysis of distal microtephra. Applied Geochemistry 21, 1692-1714.
Ponader, C.W., Brown, G.E., 1989. Rare-earth elements in silicate glass melt systems, effects of composition on the coordination environments of La, Gd and Yb. Geochimica et Cosmochimica Acta 53, 2893-2903.
Prowatke, S., Klemme, S., 2005. Effect of melt composition on the partitioning of trace elements between titanite and silicate melt. Geochimica et Cosmochimica Acta 69, 695-709.
Prowatke, S., Klemme, S., 2006. Trace element partitioning between apatite and silicate melts. Geochimica et Cosmochimica Acta 70, 4513-4527.
Rollinson, H., 1993. Using geochemical data: evaulation, presentation, interpretation. Longman Scientific and Technical.
Runyon, R.P. and Haber, A., 1988, Fundamentals of Behavioural Statistics, Random House.

Russo, R.E., Mao, X., Gonzalez, J., Mao, S., 2002. Femtosecond laser ablation ICP-MS. Journal of Analytical Atomic Spectrometry 17, 1072-1075.
Shane, P.A., Smith, I.E.M., 2000. Geochemical fingerprinting of basaltic tephra deposits in the Auckland Volcanic Field. New Zealand Journal of Geology and Geophysics 43, 569-577.
Shiihara, M., Torii, M., Okuno, M., Domitsu, H., Nakamura, T., Kim, K.-H., Moriwaki, H., Oda, M., 2011. Revised stratigraphy of Holocene tephras on Ulleung Island, South Korea, and possible correlatives for the U-Oki tephra. Quaternary International 246, 222-232.
Smith, D.J.W., Westgate, J.A., 1969. Electron probe technique for characterising pyroclastic deposits. Earth and Planetary Science Letters 5, 313-319.
Smith, V.C., Mark, D.F., Staff, R.A., Blockley, S.P.E., Ramsey, C.B., Bryant, C.L., Nakagawa, T., Han, K.K., Weh, A., Takemura, K., Danhara, T., 2011a. Toward establishing precise 40Ar/39Ar chronologies for Late Pleistocene palaeoclimate archives: an example from the Lake Suigetsu (Japan) sedimentary record. Quaternary Science Reviews 30, 2845-2850.
Smith, V.C., Pearce, N.J.G., Matthews, N.E., Westgate, J.A., Petraglia, M.D., Haslam, M., Lane, C.S., Korisettar, R., Pal, J.N., 2011b. Geochemical fingerprinting of the widespread Toba tephra using biotite compositions. Quaternary International 246, 97-104.
Smith, V.C., Staff, R.A., Blockley, S.P.E., Bronk Ramsey, C., Nakagawa, T., Danhara, T., 2006, Suigetsu Project Members, submitted. Tephrostratigraphy of the Lake Suigetsu SG06 sedimentary archive, Japan: markers for synchronisation of East Asian palaeoclimatic records.
Sorenson, H., 1974, The Alkaline Rocks, John Wiley and Sons.
Staff, R.A., Bronk Ramsey, R., Bryant, C.L., Brock, F., Payne, R.L., Schlolaut, G., Marshall, M.H., Brauer, A., Lamb, H.F., Tarasov, P., Yokoyama, Y., Haraguchi, T., Gotanda, K., Yonenobu, H., Nakagawa, T., 2011, Suigetsu Project Members., 2003. New ^{14}C determinations from Lake Suigetsu, Japan: 12,000 to 0 cal BP. Radiocarbon.
Sylvester, P.J., 2008. Matrix effects in laser ablation-ICP-MS, Mineralogical Association of Canada Short Course 40, Vancouver, B.C., 67-78.
Takemura, K., 1994. Sedimentary facies and chronology of core samples from Lake Mikata, Lake Suigetsu and Kurota Lowland, central Japan -sedimentary environment in Mikata Lowland since the Last Interglacial time. Journal of Geography (Japan) 103, 233-242.
Thomas, J.B., Bodnar, R.J., Shimizu, N., Sinha, A.K., 2002, Determination of zircon/melt trace element partition coefficients from SIMS analysis of melt inclusions in zircon, Geochimica et Cosmochimica Acta, 66, 2887-2901.
Thorarinsson, S., 1944. Tefrokronologiska studier på Island : Þjórsárdalur och dess förödelse. Doctoral Thesis, Stockholms Högskola.
Tomlinson, E.L., Thordarson, T.A., Muller, W., Thirlwall, M., Menzies, M.A., 2010. Microanalysis of tephra by LA-ICP-MS — Strategies, advantages and limitations assessed using the Thorsmörk ignimbrite (Southern Iceland). Chemical Geology 279, 73-89.
Westgate, J.A., Pearce, N.J.G., Perkins, W., Fuge, R., Wintle., A.G., 1994. Trace-element analysis of volcanic glass shards by laser ablation inductively coupled plasma mass spectrometry: application to tephrochronological studies. Applied Geochemistry 9, 323-335.
Westgate, J.A., Pearce, N.J.G., Perkins, W.T., Shane, P.A., Preece, S.J., 2011. Lead isotope ratios of volcanic glass by laser ablation inductively-coupled plasma mass spectrometry: Application to Miocene tephra beds in Montana, USA and adjacent areas. Quaternary International 246, 82-96.
Wilson, M., 1989. Igneous Petrogenesis. Springer.
Wohletz, K.H., 1999. MAGMA: Calculates IUGS Volcanic Rock Classification, Densities, and Viscosities, Los Alamos New Mexico.

Appendices

Page

EPMA operating conditions *109*
LA-ICP-MS operating conditions *110*

Appendix 1 MPI-DING and USGS reference materials with no F.F…….....111

Appendix 2 The Pearce *et al.* (2011) 20 µm crater diameter F.F……..117

Appendix 3 Trace element analyses of 16 samples corrected only using the Pearce *et al.* (2011) F.F……...118

Appendix 4 Calculation of LLD and LLQ…….....136

Appendix 5 Calculation of sample polymerisation (NBO/T)……...156

Appendix 6 Fractionation and element properties……....158

Appendix 7 Excitation voltage and fractionation…….159

Appendix 8 Calculation of new fractionation factors……..160

Appendix 9 Application of new F.F.s to trace element analyses UT2252 and Minoan glass shards…….162

Appendix 10 Major element compositions of Ulleungdo proximal units……...170

Appendix 11 Trace element compositions of Ulleungdo proximal units, with only the Pearce *et al.* (2011) F.F. applied……...172

Appendix 12 Trace element compositions of Ulleungdo proximal units with new F.F…….175

Appendix 13 Statistical distance tests……..178